広島大学学位請求論文

Multi-band Observational Study on Two Nearby Type Ia Supernovae

多バンド観測による2つの近傍のIa型超新星に関する研究

2019年

広島大学大学院理学研究科
物理科学専攻

Miho Kawabata

Contents

Abstract

For Type Ia supernovae (SNe Ia), there is a well-established correlation between the peak luminosity and the following decline rate of the light curve, which has been used to measure distances to remote galaxies. Thus, SNe Ia have been used to discover the acceleration of the cosmic expansion and are important for giving constraints on the cosmological parameters. It is widely believed that SNe Ia are explosion of white dwarfs, i.e., compact degenerate stars which are produced in the core of evolved low-mass stars. The progenitor system and explosion mechanism of SNe Ia are still under debate. A possible scenario is single degenerate model. The companion star is a non-degenerate companion star, e.g., the red giant star. The other possible scenario is the merger of two white dwarfs. Some methods to distinguish the progenitor scenarios have been suggested. We have tried to obtain the further information on the explosion properties of SNe Ia and to give constraints on the companion star or the circumstellar environments through multi-band observations.

In this thesis, we focus on two SNe Ia discovered in nearby galaxies. As the first study, we give constrains of the explosion mechanism of the peculiar Type Iax supernova (SN Iax) from our extended observations. We carried out optical and near-infrared observations of SN Iax 2014dt from 14 to 410 days after the maximum light. The light curves and the spectra show considerably slow evolution until the late phase. After $\sim$100 days, the spectral energy distribution was nearly constant and its shape does not change very much, and the bolometric light curve flattened during the same period. These observations suggest the existence of an optically thick, low velocity component that almost fully trapped the γ-ray energy from ^{56}Co decay. These findings are consistent with the predictions from the weak deflagration model, leaving a bound white dwarf remnant after the explosion. This model is constructed assuming a single degenerate progenitor system. Thus, our findings support that the SNe Iax is originated from the single degenerate system. This is consistent with the indication by the previous studies.

As the second study, we searched the signature of the interaction between the SN ejecta and the companion star from the extremely early phase observation of SN Ia, within a few days after the explosion. We present ultraviolet and optical observations of a canonical Type Ia SN 2017erp just after the discovery. We estimate the rising time and we find it is relatively longer than those of typical SNe Ia. The earliest color is much bluer than those of a canonical SNe Ia, e.g., SN 2011fe, showing no significant signature of the ejecta-CSM interaction. From comparison of the color evolution and the theoretical models, we specify the signature of the interaction between the ejecta of SN and the companion or CSM for our data. In both cases, our observations support that the explosion of SN 2017erp occurs in the single degenerate scenario. In addition, we find a possible signature of the companion star for SNe 2017erp. For single degenerate scenario, the intensity of the prompt emission should be dependent on the viewing angle against the progenitor system. Further observations at the extremely early phase may unveil the real origin of the prompt emission, and it may provide strong evidences of the single degenerate scenario in the future.

Chapter 1

Introduction

1.1 Supernovae

1.1.1 Classification of Supernovae

Supernovae (SNe) are one of the most energetic phenomena in the universe. The typical explosion energy is 10^{51} erg. From the optical spectra around the maximum light, SNe are generally classified into several types (Filippenko 1997). Classification of SNe was performed using spectral features. The spectra of Type Ia SNe (SNe Ia) do not show the hydrogen absorption lines. On the other hand, Type II SNe show hydrogen features in their spectra. When the spectra show the characteristic silicon, sulfur, and iron absorption lines, SN is classified into SNe Ia.

By significant features other than hydrogen, Type I SNe are divided into subtypes as Type Ia, Ib and Ic. A strong absorption line of Si II λ6355 is seen for SNe Ia. Generally, this line is shifted to around 6100 Å due to the ejecta expansion of SNe. The spectra of SNe Ib have the helium absorption lines. In the spectra of SNe Ic, there are no significant absorption lines of hydrogen and helium. In Figure 1, we show the spectra of different type SNe. SNe Ib/c and II come from the core collapse (CC) from massive stars (more than about 8 – 10$M_\odot$). On the other hand, SNe Ia arise from the explosion of a white dwarf (WD) in a binary system. In this thesis, we focus on SNe Ia, and describe about the progenitor system and the explosion mechanism in §1.2.

1.1.2 Source of Luminosity in Supernovae

The absolute magnitude of SNe distribute in the range of -15 – -20 mag. SNe are the most luminous events among astronomical objects. The thermal energy source is the radioactive ^{56}Ni (Truran et al. 1967; Colgate & McKee 1969). The large amount of ^{56}Ni are synthesized in the large explosion energy (Arnett 1969b). Radioactive ^{56}Ni decays into ^{56}Co due to electron capture decay. For SNe Ia, the large amount of the ^{56}Ni are synthesized in the thermal nuclear runaway.

$$^{56}Ni \rightarrow ^{56} Co + \gamma + \nu_e. \tag{1.1}$$

The lifetime (e-folding time) of ^{56}Ni is 8.80 days. The total decay energy is 2.14 MeV, and the emitted energy is 1.75 MeV. The remaining energy is brought by neutrinos (Junde et al. 1987). The γ-rays are partly absorbed and scattered by the ejecta and converted to thermal energy or lower energy photons. The optical emission is dominant in the spectra. The decay energy rate is converted into the total radiation energy.

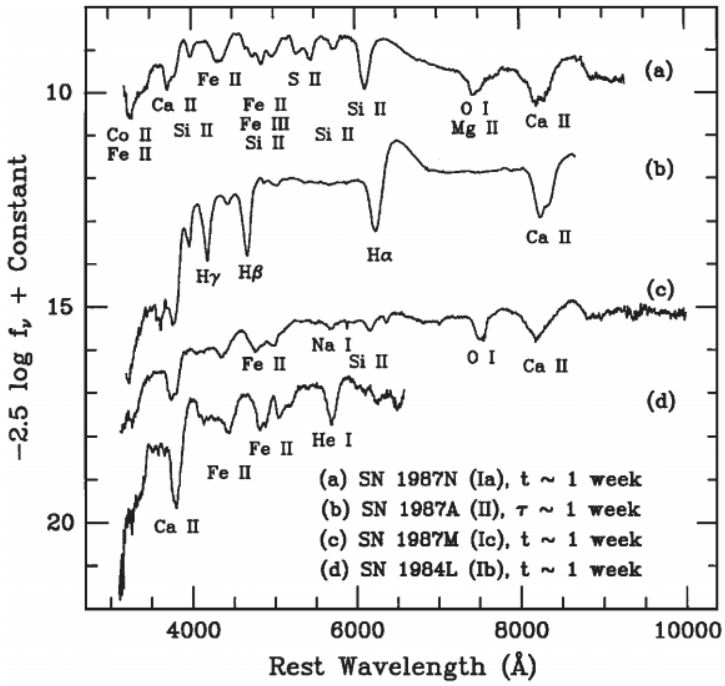

Figure 1: Comparison of the early phase spectra for four types SNe (Type Ia SN 1987N, Type II SN 197A, Type Ic SN 1987M, Type Ib SN 1984L). This figure is cited from Filippenko (1997).

^{56}Co is also a radioactive element and decays into stable isotope ^{56}Fe by electron capture and positron decays.

$$^{56}Co \rightarrow \begin{cases} ^{56}Fe + \gamma + \nu_e & (81\%) \\ ^{56}Fe + e^+ + \gamma + \nu_e & (19\%) \end{cases} \tag{1.2}$$

The lifetime of ^{56}Co is 111.3 days. The positrons interact with the ejecta, and lose their kinetic energy. The total energy emitted by the γ-ray photons is 3.61 MeV and the total kinetic energy of positron is estimated 0.12MeV (Junde et al. 1987). In the late phase, the opacity of the ejecta quite declines and transparent for the γ-ray photons. In this phase, the kinetic energy of positrons dominates the energy deposited to the ejecta. The remaining energy (0.84 MeV) is carried away by neutrinos (Junde et al. 1987). A typical SN Ia synthesize about $\sim 0.6 M_\odot$ ^{56}Ni elements at the explosion. For observations, the tail luminosity is proportional to the ^{56}Ni mass. We can derive the ^{56}Ni mass from the tail luminosity.

1.2 Type Ia Supernovae

By accreting the material on the surface of the WD from the non-degenerate companion star through the Roche-lobe overflow in a binary system, the WD mass gains. When the WD mass reaches the Chandrasekhar-limiting one ($M_{ch} \simeq 1.38$ M$_\odot$), the thermonuclear runaway occurs in the central region (e.g., Hillebrandt & Niemeyer 2000). In Figure 2, we show the light curves (LCs) of several SNe Ia. More luminous SNe Ia slowly fade and less luminous SNe Ia quickly fade. For SNe Ia, there is a well-established correlation between the peak luminosity and the following decline rate of the LC, which is well-known as width-luminosity relation (WLR; Phillips 1993, see Figure 3). This relation

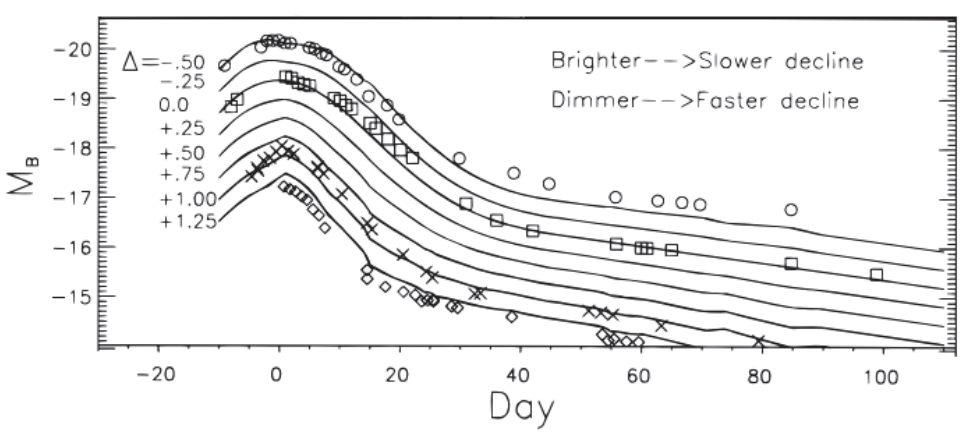

Figure 2: The light curves of several SNe Ia in the B-band. 0 day corresponds to the maximum light. The circles, squares, crosses, diamonds, plus signs and triangles symbols denote the light curves of SN 1991T, SN 1994ae, SN 1986G, SN 1991bg, SN 1992A, and SN 1980N, respectively. This figure is cited from Riess et al. (1996).

has been used to measure the distance to galaxies. The cosmological parameters have been limited using these properties (Perlmutter et al. 1999; Riess et al. 1998).

1.2.1 Explosion Mechanism

SNe Ia synthesize the large amount of ^{56}Ni by the thermonuclear explosion. There are suggested some explosion models to reproduce the observational properties of SNe Ia. In this section, we describe the some theoretical explosion models of SNe Ia. Arnett (1969a) assumed the thermonuclear burning front propagates at supersonic speed (a detonation wave). Before the WD expands, it burns out. The whole WD material (mainly C+O) is almost transformed into iron group elements. For this scenario, the explosion does not occur. Nomoto et al. (1984) suggested the deflagration model. In this model, the WD burning front propagates into outer layer in subsonic speed. Fireball ejecta temporally expands and the explosion is successful. The WD materials are mostly burned by the deflagration frame. Due to the less energetic explosion, the unburned material of WD is expected to be seen. However, it cannot reproduce larger ^{56}Ni and the faster expansion velocity. The deflagration model cannot reproduce the luminous SNe Ia. The delayed detonation model has been proposed as the established model of SNe Ia (e.g., Khokhlov 1991; Hillebrandt & Niemeyer 2000). The burning frame is ignited near the center of the WD, and it burns in deflagration initially. After that, the burning front propagates into outer layer. When it reaches critical density, the frame transformed into the detonation wave near the surface of the WD through the supersonic propagation of the burning front occurs. This model synthesizes more ^{56}Ni and the intermediate mass elements (IME; e.g., Si, S, and Ca). These elements are wholly consistent with the spectral features of SNe Ia.

On the other hand, for peculiar SNe Ia, it is considered to explode with extreme explosion parameters compared to normal SNe Ia. Furthermore, we describe the some explosion models proposed in peculiar SNe Ia; such as Type Iax SNe (see §1.3.3 for details) focusing this thesis. One possible model is the weak deflagration (e.g., Jordan

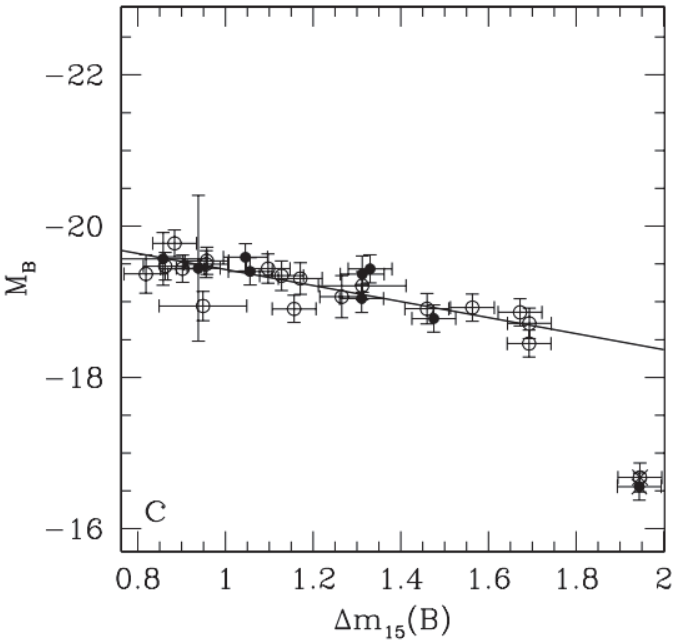

Figure 3: Correlation of the peak absolute magnitudes in the B-band with the decline rate $\Delta m_{15}(B)$. This figure is cited from Altavilla et al. (2004).

et al. 2012; Kromer et al. 2013; Fink et al. 2014), in which a considerable part of the WD could not gain sufficient kinetic energy to exceed the binding energy, and a bound WD remnant of $\sim$1 $M_\odot$ may be left after the explosion. The weak deflagration model, leaving a bound remnant predicts smaller explosion energy, and it is considered to be one plausible model in fainter SNe Ia such as SNe Iax. Other model is the pulsating delayed detonation (PDD) model. After a long-range pulsation of the WD, the delayed detonation is caused (e.g., Hoeflich et al. 1995; Hoeflich & Khokhlov 1996). The PDD model can be also explained for normal SNe Ia. In the case of SNe Iax, the observational properties are explained (e.g., SN 2012Z; Stritzinger et al. 2015).

1.2.2 Progenitor System

Possible Progenitor Scenario

The progenitor system is still under debate. Here, we describe two widely-accepted scenarios. One possible scenario is a single degenerate (SD) one, which consists of a WD and a companion star. The companion star is a non-degenerate companion star, e.g., main sequence or red giant star. The companion star transforms mass by Roche-lobe overflow to the WD, and the mass of the WD approaches the Chandrasekhar limit mass (Whelan & Iben 1973; Nomoto 1982; Hachisu et al. 1999). In this scenario, whether a WD results in SN explosion depends on the mass accretion rate. The mass accretion rate is predicted to be from $10^{-7} - 10^{-8}$ $M_\odot$ yr^{-1} through the numerical calculation (Nomoto 1982). If the binary system has the slower mass accretion rate, nova-like eruption occurs. For the evolved binary systems, it is possible that the direct mass transfer to the WD instead of hydrogen occur. For peculiar SNe Ia, the helium emission lines are detected (see §1.3.3), and it may be related to such progenitor scenario.

The second possible scenario for triggering a SNe Ia is the merger of two WDs (DD scenario; Iben & Tutukov 1984, Webbink 1984). In the classical model, the carbon

on the surface may be only ignited without explosive burning. As a result, the WDs convert to the an oxygen and neon (O-Ne) WD. It is considered that the WD collapses to a neutron star rather than the SN explosion (Saio & Nomoto 1985). Recently, the hydrodynamic calculation of the detonation model triggered by the two WD merger have been suggested (Pakmor et al. 2010). In this model, after two WDs having close masses merge, the detonation explosion is triggered in the off-center region when the density reaches critical one. This explosion can successfully reproduces the observational properties of faint SNe Ia (Pakmor et al. 2010), and the normal SNe Ia (Pakmor et al. 2012), because the small ^{56}Ni mass is synthesized.

Generally, it takes very long time that two WDs merge, because the orbital period shrinks, depending on the gravitational wave. The timescale even extends to the cosmic times. During the orbit shrinkage, the circumstellar material sufficiently diffuses and the surrounding environment is clean comparing to single degenerate system. Some DD models occasionally predict to eject the dense CSM to very close environment to the progenitor just after two WDs merge (Raskin & Kasen 2013; Shen et al. 2012; Tanikawa et al. 2015). On the other hand, the environment with the dense CSM is robustly expected for the SD scenario. In some SNe Ia, they are in the environment with dense CSM using time variable Na I D absorption lines arising in the CSM (e.g., Patat et al. 2007; Blondin et al. 2009; Simon et al. 2009).

Probe to the Progenitor

Some methods to distinguish the progenitor scenario have been suggested. The first one is direct imaging of the progenitor system. In previous studies, a bright red giant companion scenario is excluded through the pre-explosion image analysis for very nearby SNe (Nelemans et al. 2008; Maoz & Mannucci 2008; Kelly et al. 2014; Li et al. 2011). However, this method is applicable only to the progenitor systems in galaxies within 10 Mpc. For most SNe Ia, even if the progenitor is a red supergiant, it cannot be detected.

Second method is to search a signature of the progenitor indirectly. In the SD scenario, the interaction between the SN ejecta and companion can be seen within a few days from the explosion (Kasen 2010; Kutsuna & Shigeyama 2015; Maeda et al. 2018). When the ejecta collides with the companion, it creates a shock cooling signature over the first few days. The signature depends on the size and distance to the companion and its viewing angle. From the data at few days after the explosion, in the case of some SNe Ia, those parameters of the companion star have been constrained (e.g., SN 2012cg; Silverman et al. 2012a, Marion et al. 2016).

Some previous studies suggest that the interaction between the ejecta and the circumstellar material (CSM) can be seen (e.g., Piro & Morozova 2016; Maeda et al. 2018). The signature in the early phase similar to the ejecta-companion interaction has been detected, however the LC timescale and color evolution were somewhat different (Maeda et al. 2018). These features should be a probe of the unknown progenitor.

Previous Observations From First Few Days

Recently, many researchers focus on the observations of SNe Ia within a few days from the explosion. SN 2011fe is the most-well studied SN Ia among this 40 days, because it was discovered in the very close galaxy M101 at 6.4 Mpc by the Palomar Transient Factory (Nugent et al. 2011a). The first detection is about 11 hour after the explosion, and the 5 σ non-detection is 4 hour. From the observation soon after the explosion, it can provide strong constrain to the progenitor scenario (Nugent et al. 2011a). Additional observations exclude the stellar explosion with larger radius than a few $R_\odot$ (Bloom et al.

2012). Additionally, the ceaseless photometric observations soon after the explosion using *Kepler* space telescope unveil the unexpected rising of the luminosity, although they are limited to a few examples (e.g., SN 2018oh; Li et al. 2018b). Although there is a few observations in a single band, the observational samples in multi-band are limited from a few days. These further observations should be the key to understand the progenitor scenario of SNe Ia.

1.2.3 Diversity in the Early Phase of SNe Ia

Although SNe Ia exhibit their homogeneity in LCs, the diversity for SNe Ia is also known, even in "normal" SNe Ia. SNe Ia have some outlier events, and we describe about in §1.3. Benetti et al. (2005) classified SNe Ia into three subgroups. They use the time evolution of the expansion velocity and the strength of Si II λ6355 absorption line. "FAINT" subgroup has low expansion velocities and fast deceleration of Si II λ6355 velocity. In this subgroup, the peak magnitude is fainter then those in typical SNe Ia, and they are similar to so-called SN 1991bg-like ones (see Filippenko et al. 1992a, Leibundgut et al. 1993, Turatto et al. 1996). The second subgroup shows the fast velocity deceleration and normal luminosity. It is called "high velocity gradient (HVG)". The third one is the slow velocity evolution and normal luminosity, called "low velocity gradient (LVG)". This group includes normal SNe Ia and bright SNe Ia such as SN 1991T-like events (see §1.3.1).

The other scheme of classification for SNe Ia has been suggested by Branch et al. (2006). They used the ratio of the equivalent widths of the Si II λ5972 and Si II λ6355 absorption lines around maximum light. In this scheme, SNe Ia are divided into four subgroup. The two subclass, "Core Normal (CN)" and "Broad Line (BL)" that have broader Si II λ6355 line, are roughly "normal" SNe Ia. The "Cool (CL)" shows the deeper Si II λ5792 line. SNe Ia classified as this subclass are fainter and have a fast decline rate. Finally, there is the "Shallow Silicon (SS)". This subclass has weak absorption lines of Si II λ5792 and Si II λ6355. In this subclass, the spectra indicate the high temperature photosphere. This subclass contains the SN 2002cx-like SNe Ia (or Type Iax SNe; SNe Iax, see §1.3.3), overluminous SNe Ia such as SN 1991T or SN 1999aa-like SNe Ia (see §1.3.1 and §1.3.2).

Stritzinger et al. (2018) presented that there are two distinct populations from comparison of the intrinsic $B-V$ color evolution among various SNe Ia within three days from the explosion. SNe Ia that are blue at early phase show the similar spectra to those of SN 1991T- or SN 1999aa-like SNe Ia. These SNe Ia are also consistent with the SS subclass, which are more luminous than typical SNe. On the other hand, SNe Ia that are redder at early phase are corresponding to CN or CL SNe, and these are normal or slightly faint events.

1.3 Peculiar SNe Ia

The previous studies suggest that SNe Ia have some extreme events in the $M_{B,max}$–$\Delta m_{15}(B)$ plane (see Figure 4). In this section, we describe some extreme/peculiar events such as 91T-like SNe, 99aa-like SNe and 02cx-like SNe.

1.3.1 SN 1991T-like SNe

91T-like SNe show the bright peak luminosities and broad LCs. SN 1991T is $\gtrsim$0.6 mag brighter than typical SNe Ia (Filippenko et al. 1992b). The decline rate defined as the

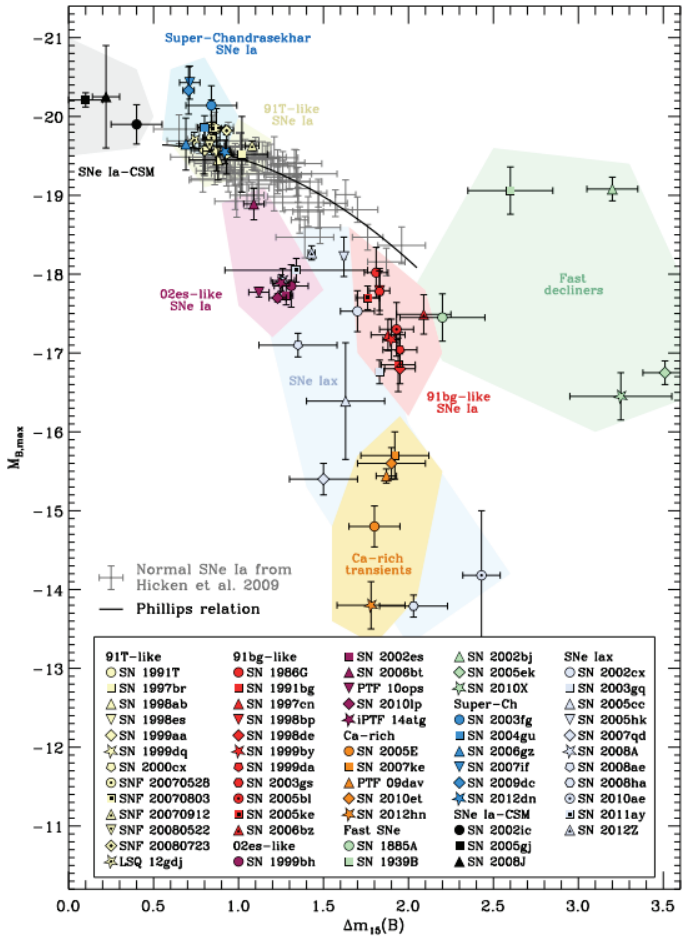

Figure 4: Correlation of the peak absolute magnitudes in the B-band with the decline rate $\Delta m_{15}(B)$. There are normal SNe Ia (gray symbols) and some extreme events. This figure is cited from Taubenberger (2017).

magnitude difference between 0 and 15 days after the maximum light, is $\Delta m_{15}(B) = 0.95 \pm 0.05$ mag (Lira et al. 1998). 91T-like SNe are slightly overluminous than those expected from the WLR with the same $\Delta m_{15}(B)$ (e.g., Taubenberger 2017). In spectra of 91T-like SNe at the early phase, the Fe III absorption lines dominate. Before the maximum light, the spectra of 91T-like SNe show weak or no absorption lines of IME.

1.3.2 SN 1999aa-like SNe

SN 1999aa is overluminous and shows a slowly decline rate ($\Delta m_{15}(B) = 0.746 \pm 0.024$ mag; Krisciunas et al. 2000), similar to SN 1991T. The early spectra of SN 1999aa are similar to those of 91T-like SNe, i.e., the Fe III absorption lines dominate and IME absorption lines are weak (e.g., Garavini et al. 2004). The spectra of SN 1999aa have slight differences compared with those of SN 1991T. The Ca II lines, especially Ca II H and K, are prominent in the spectra of SN 1999aa. 99aa-like SNe could be the transitional event between 91T-like SNe and normal SNe Ia (e.g., Taubenberger 2017).

1.3.3 SN 2002cx-like SNe / Type Iax SNe

Some SNe Ia deviate from the WLR, and their peak luminosities are significantly fainter ($\geq$1 mag) than those of normal SNe Ia with similar decline rates. These outliers have been called SN 2002cx-like SNe (Li et al. 2003) or SNe Iax (Foley et al. 2013). SNe Iax commonly show lower luminosities, lower expansion velocities and hotter photospheres around their maximum light than normal SNe Ia (Foley et al. 2013 and references therein); on the other hand, their maximum magnitudes and decline rates scatter. For example, the maximum magnitude of the faintest SN Iax 2008ha is only -13.74 ± 0.15 mag in the B-band (Foley et al. 2009), which is $\sim$4 mag fainter than that of the prototypical SN Iax SN 2002cx. The line velocities of SNe Iax around the maximum light are 2000–8000 km s^{-1}, whereas those of normal SNe Ia are $\gtrsim$10000 km s^{-1}. The estimated ^{56}Ni mass and the explosion energy of SNe Iax are only 0.003–0.3 M$_\odot$ and 10^{49}–10^{51} erg, respectively (e.g., Foley et al. 2009; Foley et al. 2013; Stritzinger et al. 2015).

The identification of the possible progenitor systems for some SNe Iax have been reported and they could be important for exploring the explosion model and links to normal SNe Ia. For SN 2012Z, a blue hot star (possibly a companion helium star) has been detected in pre-explosion images (McCully et al. 2014a). For SN 2008ha, a luminous redder source has appeared in the post-explosion images, which could be a bound remnant or a survived companion star (Foley et al. 2014). For other SN Iax (SN 2008ge; Foley et al. 2010 and SN 2014ck; Tomasella et al. 2016), only the upper limits for the brightness of the progenitors have been derived. SNe 2004cs and 2007J show the helium emission lines in their spectra (Foley et al. 2013). The helium lines should arise from the progenitor systems, because the helium is not synthesized in the explosion.

From the recent observations, in the case of SNe Iax, the SD scenario are likely somewhat advantageous. Many researchers have discussed plausible models that can reproduce the observed properties assuming SD scenario (see §1.2.1). However, Valenti et al. (2009) suggested that a fraction of SNe Iax could be CC SNe based on of some characteristics in the optical spectra. Moriya et al. (2010) suggested a 'fallback CC SN model' for SNe Iax, where a considerable fraction of the ejecta would fall onto the central remnant, probably a black hole, in a CC SN explosion of a massive star ($\gtrsim$25 M$_\odot$).

To date, the number of SNe Iax for which the evolution of the late phases has been well-observed still remains very small. Late phase observations are expected to carry

important information on the progenitor and explosion through a direct view to the inner part of the ejecta (e.g., Maeda et al. 2010). The spectra of some SNe Iax in the late phase show the permitted lines having the P Cygni profiles, unlike those of SNe Ia. From the analysis of the late phase spectra, Foley et al. (2016) suggested that the ejecta of SNe Iax have two distinct components, one of which creates the photosphere even in the late phase. Thus, the data for SNe Iax in the late phases can provide meaningful constraints on an explosion model.

1.3.4 Goal of This Thesis

There are many observation samples of SNe Ia, however, there are still some unresolved issues. The two different explanations are mainly considered for the progenitor system of SNe Ia (c.f., §1.2.2). To constrain these issues of SNe Ia, we require the more observational data such as the peculiar SNe Ia and SNe Ia at a few days from the explosion.

In this thesis, we focus on two SNe Ia discovered at nearby galaxies. We can obtain the data of nearby SNe from the early to the late phase when the SNe are fainter, because the distance to the galaxy is relatively close. From the observations of these two SNe Ia, we try to determine whether the signature expected by SD scenario can be seen or not. As the first study, we preformed the optical and near-infrared (NIR) observation of SN Iax 2014dt through 400 days from its explosion. There were few sample in which such as long-term observation of SNe Iax were obtained. From the extended observation, we try to constrain the explosion models of the peculiar SN Ia. From the luminosity and the line velocity, we estimate the explosion parameters such as the ^{56}Ni mass, the explosion energy and the ejecta mass. We compare these parameters and the observational features, and constrain the explosion mechanism. As the second study, we performed the optical and ultraviolet (UV) observation of SN Ia 2017erp that was discovered at very early phase, a few days from the explosion. The observational samples of color evolution from early phase is rare. Then, the additional samples is important to constrain the progenitor scenario. From the photometry and spectroscopy around the maximum light, we determine its subclass in SNe Ia, and examine whether the color evolution of SN 2017erp at the early phase shows the signature expected in SD scenario such as the interaction between the SN ejecta and the companion star or CSM.

Chapter 2

Observations and Data Reduction

2.1 Target SNe

About 1000 SNe are discovered each year by extensive supernova survey projects or amateur astronomers. About 70 % of them are SNe Ia. Our targets are nearby SNe Ia within 20 Mpc. For such SNe Ia, we can perform the prompt observations and provide a constraint on the progenitor system through the observations. We can also perform the long-term observations in optical and NIR wavelengths even if the SNe are intrinsically faint. Using these data, we can discuss the explosion properties of faint SNe Ia. In order to collect such data, we use the 1.5 m Kanata telescope in Hiroshima University. We focus on good prospects SNe Ia, SNe 2014dt and 2017erp, discovered in nearby galaxies.

2.1.1 SN 2014dt

SN 2014dt was discovered at 13.6 mag in a nearby galaxy M61 on 2014 October 29.8 UT by a Japanese amateur astronomer, K. Itagaki (Nakano et al. 2014). The spectrum obtained on 2014 October 31 UT by the Asiago Supernova classification program was similar to that of a SN Iax at ∼1 week after the maximum light (Ochner et al. 2014). SN 2014dt is one of the nearest SN Iax ever discovered as mentioned later. Foley et al. (2015) gave upper limit magnitudes using pre-explosion images taken with the Hubble Space Telescope (HST), which is consistent with a system with a low-mass evolved or main-sequence companion, while the upper limit could not reject a Wolf-Rayet star. The distance of M61 has been obtained by several works and they are summarized in the NASA/IPAC Extragalactic Database (NED)[1]. Bose & Kumar (2014) reported the distance obtained by applying the expanding photosphere method (EPM) to a Type II-plateau SN 2008in in appeared in the same galaxy. In the EPM, we compare the radius determined from the expansion velocity and that estimated by fitting observed blackbody fluxes at several phases (Kirshner & Kwan 1974; Schmidt et al. 1992). Bose & Kumar (2014) gave two values as $\mu = 30.45 \pm 0.10$ mag and 30.45 ± 0.10 mag for the distance modulus using two different atmosphere models. In this thesis, we adopt the EPM distance of M61, $\mu = 30.81 \pm 0.20$ mag, which was also consistent with those calibrated with another atmosphere model updated by Dessart & Hillier (2005). For the total extinction towards SN 2014dt, we simply adopted $E(B-V)_{\rm total} = 0.02$ mag, following Foley et al. (2015).

[1] http://ned.ipac.caltech.edu/

2.1.2 SN 2017erp

SN 2017erp was discovered at 16.8 mag in the outskirt of spiral galaxy NGC 5861 on 2017 June 13.6 UT by K. Itagaki (Itagaki 2017). The spectrum was obtained on 2017 June 13.9 UT, and this SN was classified as a SN Ia at about 10 days before the maximum light (Jha et al. 2017). The distance of NGC5861 is reported with many previous studies (e.g., de Vaucouleurs et al. 1981; Willick et al. 1997). We adopted the distance modulus of NGC 5861 as $\mu = 32.04 \pm 0.8$ mag, which is the weighted-average one obtained using the Tully-Fisher relation listed in NED. The dust extinction of this line of sight through the Milky Way is estimated as $E(B-V)_{\rm MW} = 0.0926 \pm 0.0005$ mag (Schlafly & Finkbeiner 2011), and the extinction within the host galaxy is $E(B-V)_{\rm host} = 0.097$ mag (Brown et al. 2018). This $E(B-V)_{\rm host}$ is estimated using the some multi LC fitting methods of SN 2017erp (Brown et al. 2018).

2.2 Telescopes and Instruments

We performed the photometric and spectroscopic observations of these SNe from the UV to NIR wavelengths. The SNe were observed using various telescopes and instruments. We describe the detail of the observations in this section. In Tables 1 and 2, we summarize telescopes, instruments, modes, and filters that used for SN 2014dt and SN 2017erp, respectively.

2.2.1 1.5m Kanata telescope

The Kanata telescope is a 1.5m diameter optical/infrared telescope, and it has a F/12.2 Ritchy-Cretien optics, at Higashi-Hiroshima Observatory located in the Higashi-Hiroshima, Japan. Main scientific targets with the Kanata telescope are transient objects including SNe, gamma-ray bursts (GRBs), active galactic nucleis (AGNs), and many kinds of variable stars. The telescope has high mobility, 5 degrees/second around the azimuth axis, 2 degrees/second around the altitude axis. Three instruments are regularly installed to the Kanata telescope. We use two instruments, Hiroshima One-shot Wide-field Polarimeter (HOWPol; Kawabata et al. 2008) and Hiroshima Optical and Near-InfraRed camera (HONIR; Akitaya et al. 2014) for the SN observations.

HOWPol

HOWPol is installed to the Nasmyth focus of Kanata telescope. This instrument has some observational modes, imaging, spectroscopy, narrow- and wide-field imaging polarimetry in optical wavelengths (4500–10000Å). The field of view of the imaging mode is the 15 arcmin diameter circle. The typical limiting magnitude is measured to be 19.2 mag for 600 second exposure time in the R-band image, and the uncertainty in magnitudes is 0.02 mag. The width of spectroscopy slit is 2.3 arcsec, and the resultant wavelength resolution is $R = \lambda/\Delta\lambda \simeq 400$ at 6000Å.

HONIR

We can simultaneously obtain the optical (5000–10000Å) and NIR (10000–24000Å) data using HONIR. HONIR is installed to the Cassegrain focus of Kanata telescope. The various observational modes are provided by HONIR. We are flexibly available for imaging, spectroscopy, narrow- and wide-field imaging polarimetry and spectropolarometry in the optical and NIR regions, respectively. The field of view of the imaging mode is

Table 1: Summary of telescope and instruments for SN 2014dt

Telescope	Instruments	Mode	Wavelength
1.5m Kanata	HOWPol	Imaging	B, V, R, I
1.5m Kanata	HOWPol	Spectroscopy	4000–10000Å
1.5m Kanata	HONIR	Imaging	J, H, K_s
51cm telescope	Andor	Imaging	B, V, R, I
8.2m Subaru	FOCAS	Imaging	B, V, R, I
8.2m Subaru	FOCAS	Spectroscopy	4700–9400Å

the 10 arcmin square. The observations of NIR are more affected than that of optical by the background light from the atmosphere and the thermal emission of the instruments. The brightness of the background light varies depending on the state of the atmosphere and altitude. We adopted the dithering method that obtained the multiple image with offsets. We can use the combined image as a calibration data. The detail are described in §2.3.2.

2.2.2 51cm telescope

We performed optical $BVRI$-band photometry for SN 2014dt using the 51cm Cassegrain, F/12 telescope at Osaka Kyoiku University (OKU). The data obtained by an Andor DW936N-BV CCD camera, and the field of view is the 16 arcmin square.

2.2.3 8.2m Subaru telescope

The Subaru telescope is a 8.2m diameter optical/infrared telescope, that has a F/12.6 Ritchy-Cretien optics, at the summit of Mauna Kea in Hawai'i, USA, operated by the National Astronomical Observatory of Japan (NAOJ). We performed optical VR-band photometry and spectroscopy using the Faint Object Camera And Spectrograph (FOCAS; Kashikawa et al. 2002) for SN 2014dt. FOCAS can provide various observing modes as optical imaging and long-slit and multi-slit spectroscopy, imaging and spectropolarimetry. The observable wavelength range is 3700–10000Å, and the field of view of the imaging mode is the 6 arcmin diameter circle. The width of the used spectroscopy slit was 0.8 arcsec, and the resultant wavelength resolution was $R = \lambda/\Delta\lambda \simeq 650$ at 6000Å.

2.2.4 *Swift*

The *Swift* is a space craft telescope that is part of NASA's medium explorer program. This is the multi wavelength observatory dedicated to the study GRB. There are three instruments on board, and we used the UV to optical data obtained by the UV/Optical Telescope (UVOT). UVOT is the 30cm telescope, and the observable wavelength is 1700–6500Å. The field of view is 17 arcmin. The UVOT can perform imaging and spectroscopy. We downloaded the imaging data of SN 2017erp from the Swift Data Archive[2].

[2]http://www.swift.ac.uk/swift_portal/

Table 2: Summary of telescope and instruments for SN 2017erp

Telescope	Instruments	Mode	Wavelength
1.5m Kanata	HOWPol	Imaging	B, V, R, I
1.5m Kanata	HOWPol	Spectroscopy	4000–9400Å
Swift	UVOT	Imaging	$UVW2, UVW1, U, B, V$

2.3 Data Reduction

We reduced the data using *IRAF* that is commonly used for the reductions and analysis of astronomical data. *IRAF* is the Image Reduction Analysis Facility, distributed by the National Optical Astronomy Observatory, which is operated by the Association of Universities for Research in Astronomy (AURA) under a cooperative agreement with the National Science Foundation. In this section, we describe the flow of the data reduction.

2.3.1 Optical Data

We take the data of target objects. These are called "object frames". They need to be processed to remove the fake signals by the electronic readout noise, thermal electrons and the difference in sensitivities between pixels and so on. We obtained several types of calibration data due to remove or correct for them.

Corrections of Bias

The obtained data by CCDs have some signals even with zero exposure time. This signals are called bias. We corrected the bias using the frames taken with 0 second exposure and the counts in the overscan region in the object frames. The data obtained by HOWPol and FOCAS have been corrected in this manner.

Corrections of Dark Noise

In cases of using Andor CCD, the cooling of the CCD is not enough to neglect the dark signal. This is caused by the dark noise. It is larger in the higher temperature of the CCD and/or in the longer exposures. The dark noise in HOWPol and FOCAS is negligible because the CCDs are sufficiently cooled (~ -100°C). On the other hand, the temperature of the CCD of Andor is typically -75°C and it varies depending on the ambient temperature. We obtained 10 dark frames with the shutter closed and the same exposure time as object frames every night. We combined the dark frames into a median frame, and subtracted it from the object frames.

Flat-Fielding

The obtained data have a pattern caused by the sensitivity variations of the each pixels of the CCD and other optics. We used a uniformly illuminated screen and obtained the flat frames with each band. We corrected the dark and bias for them, and combined into the flat frame in each band. By correcting the bias frames and dark frames and them dividing by the normalized flat frames, we complete the primary processing of the object frames.

2.3.2 NIR Data

In the data in the NIR bands, we corrected the bias and dark frames and divided the normalized flat frames in the same way as these of the optical bands. Additionally, the data in the NIR bands require several processes.

Masking Bad Pixels

There are generally more bad pixels, where the sensitivity is poor or the dark noise is exceptionally high, on the detector at NIR than that at optical. They badly affect the singles from the astronomical source, therefore we corrected them using the mask frame. In the mask frame, each bad pixel has 1 or a positive integer value as the count and the other normal pixels have 0. In the object frames and the flat frames the bad pixels specified by this mask image are complemented using the pixel counts around the bad pixel.

Flat-Fielding

The observation at the NIR bands greatly affects the background light from the atmosphere and the thermal emission of the instruments. To subtract these, many images were obtained so that the SN, the host galaxy and the field stars. By combining these images with the median value, it is possible to remove the contribution of these objects and only the background light component remains. We made these frame for each NIR band, and subtracted it from the object frames.

2.3.3 Host Galaxy Template Subtraction

If there is a background object on the SN (e.g., the host galaxy), it affects the measurement of the signal from the SN as a contamination. In those cases, we need to subtract the host galaxy template image before we perform the photometry (for details see §2.4). The host galaxy template images should be obtained before the SN appears or after it becomes faint enough that it is negligible. In Figure 5, we show the images before and after the subtraction of the host galaxy template images.

In the case of SN 2014dt, we performed subtraction of the template galaxy in the images obtained by HOWPol, HONIR and FOCAS of the host galaxy template images. For HOWPol and HONIR, the host galaxy template images were obtained on 2018 February 23 (i.e., >1200 days after the discovery) and on 2017 April 23 (i.e., at >900 days after the discovery), respectively. For the data obtained by FOCAS, the host galaxy template images are synthesized using the SDSS $u'g'r'i'z'$ images and the relations for the flux transformation (Smith et al. 2002). We removed the cosmic rays using *L. A. Cosmic* pipeline (van Dokkum 2001; van Dokkum et al. 2012). After that, we remapped the WCS (World Coordinate System) of the obtained images using the *SExtractor* (Bertin & Arnouts 1996), and transformed the template images to fit our images using *wcsremap* [3]. The host galaxy subtraction was performed using *hotpants* [4].

For the images obtained by Andor CCD camera, we skipped the host galaxy template subtraction because the images were significantly affected by fringe patterns and the host galaxy template subtraction cannot be performed well. We, however, note that the host galaxy contamination is negligible for those images, as those were obtained in the early phases when the SN itself was much brighter than the host background (as was confirmed by the subtracted images for the HOWPol data).

[3]http://www.astro.washington.edu/users/becker/v2.0/wcsremap.html
[4]http://www.astro.washington.edu/users/becker/v2.0/hotpants.html

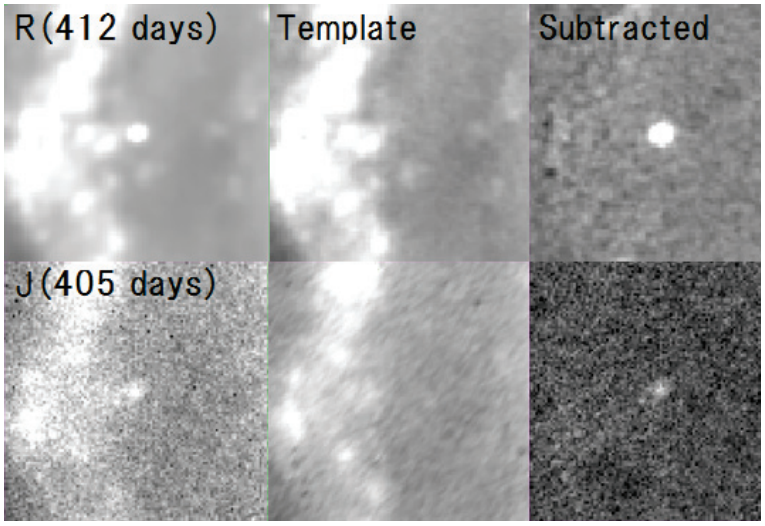

Figure 5: Comparison of the observed (left panels), the template (center), and the subtracted (right) images around SN 2014dt. Upper and lower panels are images in the R-band at 412 days and in the J-band at 405 days, respectively. The field of view is $30'' \times 30''$. The template image in the R-band is synthesized from SDSS images, and that in the J-band was obtained with HONIR (see text).

In the case of SN 2017erp, the contamination of the host galaxy is not significant (see Appendix F), and we skipped the template subtraction.

2.4 Photometry

The photometry is a process to measure the flux of the stellar objects from the obtained images. Two methods are used in our reduction. In this section, we describe them.

2.4.1 Aperture Photometry

In the 'aperture photometry', the signal from the object is integrated within the defined aperture. The aperture size is usually a few times FWHMs of the stellar image profile. The integrated signal contains not only the object but also the signal from the background sky. The sky region is specified in a doughnut-like region outside of the aperture. We calculate the signal from the object after the subtraction of the signal from the sky. In this method, it is difficult there is a contamination from underlying diffuse objects around the target one, such as the host galaxy. After the host galaxy template subtraction is properly done, the contamination is minimized. Then, we performed aperture photometry for those data. For aperture photometry, we used the DAOPHOT package in *IRAF*. We estimated the error for the photometry from the error associated with photometry, and the standard deviation in the magnitude obtained from each comparison stars and the difference images. The error for the photometry includes that caused by the host galaxy template subtraction. In the cases using the galaxy template subtraction, the error is dominated by the incomplete subtraction which cannot be overcome easily.

2.4.2 PSF Photometry

We adopt another photometry method for the data without the host galaxy template subtraction, Point-Spread-Function (PSF) photometry. In the PSF photometry, initially, we prepare the PSF model from the stars taken in the same image as the object to be measured. It fits the model to the peak flux of the object and measure the signal from it. For the subsequent PSF photometry, we used the DAOPHOT package in *IRAF*. We estimated the error in the same way as for the aperture photometry, expect for it caused by the host galaxy template subtraction.

2.4.3 Photometric Calibration

For the magnitude calibration (expect for $Swift$ data), we adopted relative photometry, i.e., using comparison stars taken in the same frame (Figures 6 and 7). The optical magnitudes of the comparison stars for SN 2014dt were calibrated with the photometric standard stars in the Landolt field (SA104; Landolt 1992), observed on photometric nights using HOWPol. We calibrated the NIR magnitude of that in the 2MASS catalog (Skrutskie et al. 2006). The magnitudes of the comparison stars for SN 2017erp were from in the AAVSO Photometric All Sky Survey (APASS) catalog (Henden et al. 2016), and converted from $g'r'i'$-bands to RI-bands using the transformation relations given by Rodgers et al. (2006). We show the obtained magnitudes of the comparison stars in Tables 3 and 4. In the UV data of $Swift$, we adopted the absolute photometry using the zeropoints reported by Breeveld et al. (2011).

For further photometric of calibration, we performed first-order color term correction which minimize the effects originating from the difference between the sensitivity of the

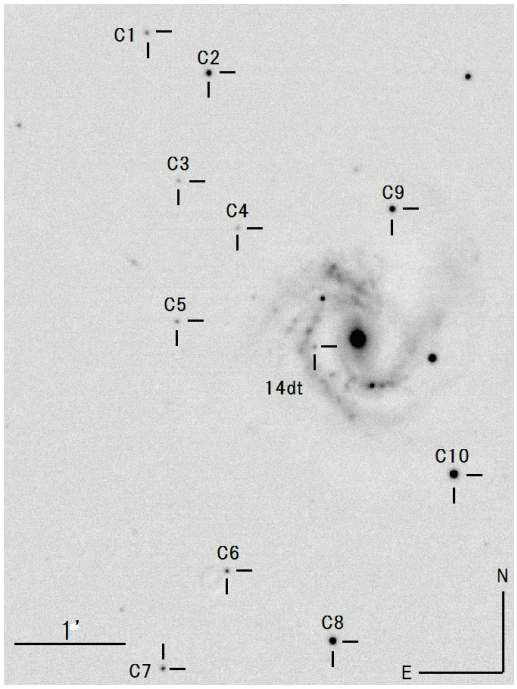

Figure 6: The R-band image of SN 2014dt and comparison stars taken with the Kanata telescope/HOWPol on MJD 57171.51 (2015 March 29).

instruments and the filter transmission function. We skipped S-correction, which is negligible for the purposes of this study (Stritzinger et al. 2002). We list the journal of the photometry in Tables 9, 10, 12 and 13.

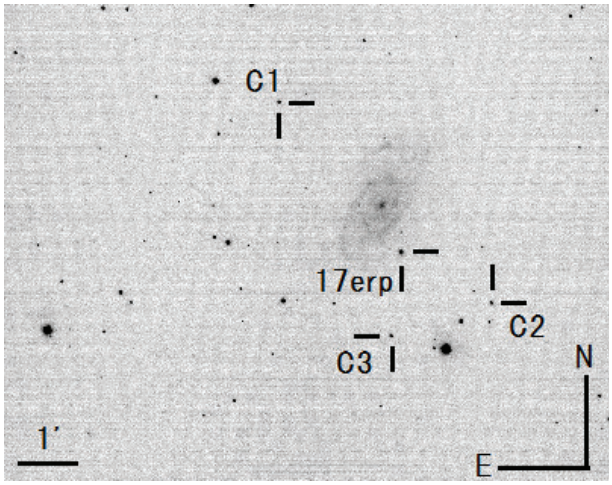

Figure 7: The R-band image of SN 2017erp and comparison stars taken with the Kanata telescope/HOWPol on MJD 57948.54 (2017 July 14).

Table 3: Magnitudes of comparison stars of SN 2014dt

ID	B (mag)	V (mag)	R (mag)	I (mag)	J (mag)	H (mag)	K_s (mag)
C1	17.536 ± 0.026	16.842 ± 0.012	16.338 ± 0.024	15.992 ± 0.012	–	–	–
C2	16.340 ± 0.023	15.505 ± 0.010	14.970 ± 0.034	14.533 ± 0.016	–	–	–
C3	18.451 ± 0.033	17.682 ± 0.015	17.170 ± 0.025	16.812 ± 0.014	–	–	–
C4	19.585 ± 0.066	18.053 ± 0.019	16.971 ± 0.025	16.061 ± 0.012	15.261 ± 0.055	14.571 ± 0.070	14.377 ± 0.099
C5	18.785 ± 0.039	17.552 ± 0.014	16.575 ± 0.024	15.872 ± 0.012	15.135 ± 0.059	14.598 ± 0.051	14.343 ± 0.087
C6	18.280 ± 0.032	16.956 ± 0.012	15.977 ± 0.024	15.252 ± 0.011	14.619 ± 0.042	13.956 ± 0.038	13.831 ± 0.061
C7	18.256 ± 0.032	16.895 ± 0.012	15.878 ± 0.024	15.144 ± 0.011	–	–	–
C8	15.542 ± 0.023	14.731 ± 0.010	14.164 ± 0.024	13.748 ± 0.011	13.525 ± 0.026	13.115 ± 0.028	13.053 ± 0.035
C9	16.844 ± 0.024	15.609 ± 0.010	14.719 ± 0.024	14.048 ± 0.011	13.326 ± 0.023	12.724 ± 0.026	12.602 ± 0.033
C10	–	–	–	–	12.734 ± 0.026	12.388 ± 0.030	12.352 ± 0.031

Table 4: Magnitudes of comparison stars of SN 2017erp

ID	B (mag)	V (mag)	R (mag)	I (mag)
C1	16.301 ± 0.006	15.444 ± 0.062	14.970 ± 0.146	14.541 ± 0.185
C2	16.682 ± 0.050	15.796 ± 0.050	15.250 ± 0.166	14.758 ± 0.294
C3	16.104 ± 0.054	15.449 ± 0.054	15.044 ± 0.118	14.586 ± 0.171

2.5 Spectroscopy

We describe the reduction of the spectroscopic data obtained by HOWPol and FOCAS. After processing in §2.3.1, we determined the position and size of aperture, and corrected the distortion caused by the optics of the instrument by fitting Legendre function. We removed the cosmic rays using *L. A. Cosmic* pipeline, and the background light after the wavelength calibration (see §2.5.1). In this way, we obtain the two-dimensional (wavelength and spatial) spectroscopic images. Then, we integrated the counts along the slit direction (i.e., the spatial direction), and obtained the one-dimensional spectra.

2.5.1 Wavelength Calibration

The wavelength calibration was made the sky emission lines for the data obtained by HOWPol. In the data obtained by FOCAS, we also used the sky emission lines, and the arc lamp (Th-Ar) lines. The wavelengths of each sky emission line and the arc lamp line is known. Then, the relationship between the wavelength and the pixel position was derived.

2.5.2 Flux Calibration

We corrected the spectral sensitivity using the spectrum of the spectrophotometric standard star, because the detector sensitivity and the atmospheric transmission varies with wavelength. The standard star data taken on the same night and used. We removed the atmospheric absorption lines in the spectrum of standard star, and fitted a high-order function to the continuum component of it. Using the fitting results, we calibrated the spectra of the SN. The journal of spectroscopy is listed in Tables 11 and 14.

Chapter 3

SN 2014dt: Extensive Observations of Type Iax

3.1 Results

3.1.1 Light Curves

Figure 8 shows $BVRIJHK_s$-band LCs of SN 2014dt. Although we missed the pre-maximum data because SN 2014dt was discovered after the maximum light, we extensively continued follow-up observations for 412 days, which is one of the longest multi-band monitorings of SNe Iax. By comparison with LCs of other SNe Iax, we estimated the epoch of the B-band maximum as MJD 56950.4 ± 4.0 (see §3.1.4). We adopted the B-band maximum as 0 day.

In Figure 9, we compare the LCs of SN 2014dt and those of SNe Iax 2002cx, 2005hk and 2008A and normal SN Ia 2003hv. In the normal SNe Ia 2003hv, the LCs in NIR bands exhibit the secondary peak. The secondary peak occurs roughly 20 to 30 days after the initial peak due to the ionization evolution of iron group elements in the ejecta in normal SNe Ia. On the other hand, in the LCs of SN 2014dt and those of SNe Iax, there are no secondary peak. This indicates the mixing of the ejecta of SNe Iax occur (Blinnikov et al. 2006; Kasen 2006). The decline rate of SN 2014dt became small after $\sim$60 days. We estimated the decline rate in the late phase by fitting a linear function to the LC. The decline rate of SN 2014dt is 0.009 ± 0.001 mag day^{-1} between 100 – 430 days in the V-band. The fitting error includes uncertainties on the phase and the photometric error. This is slower than those of SNe 2002cx (0.012 mag day^{-1}; McCully et al. 2014b), 2005hk (0.015 mag day^{-1}; McCully et al. 2014b) and 2008A (0.019 mag day^{-1}; McCully et al. 2014b). These late phase decline rates of SNe Iax except for SN 2014dt are similar to that of a normal SN Ia SN 2011fe, which is 0.0151 mag day^{-1} at 100 – 300 days (Zhang et al. 2016). SN 2014dt shows the slowest decline among SNe Ia and Iax. Similarly, SN 2014dt evolves more slowly than normal SN 2003hv in NIR.

We compared the long-term decline rates of SN 2014dt at different epochs with those of SNe 2001el (Krisciunas et al. 2003; Stritzinger & Sollerman 2007) and 2003hv (Leloudas et al. 2009), which are well-observed, non-dust forming normal SNe Ia with available late phase optical-NIR photometric data. Figure 10 shows the relationship between the long-term decline rates in optical and NIR bands for SN 2014dt at three epochs, and for SNe 2001el and 2003hv at two epochs. They are well aligned along straight lines, $m_{\rm NIR}/m_{\rm opt} \simeq 0.5$ – 0.9, suggesting that the declining trends in optical and NIR wavelengths are similar in those SNe.

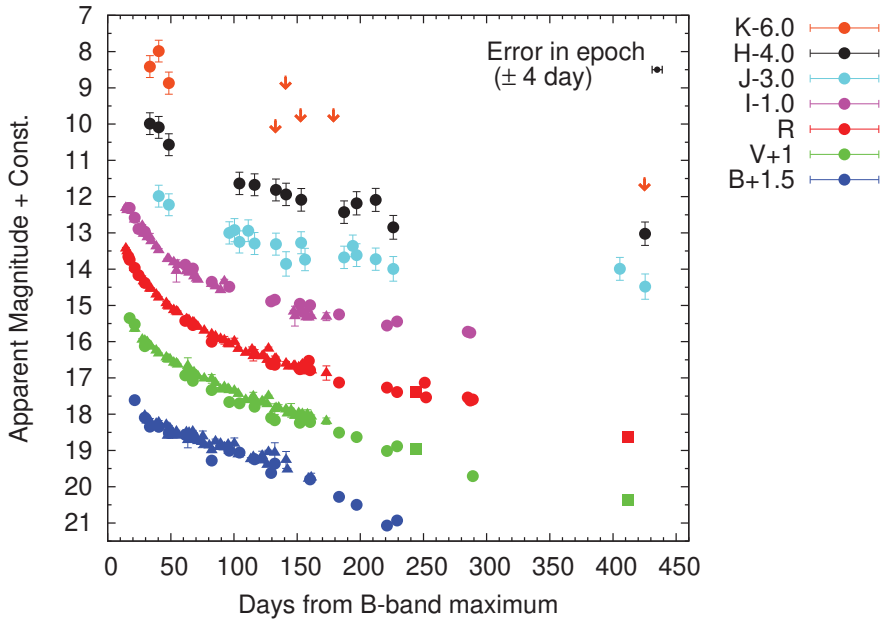

Figure 8: Multi-band light curves of SN 2014dt. The filled circles, triangles and squares denote data that were obtained at Kanata, OKU, and Subaru, respectively. The down arrows are the 3 σ upper limit magnitudes. The light curve of each band is shifted vertically as indicated in the top-right outside of the panel. We adopted MJD 56950.4 $\pm$ 4.0 as 0 day, and show its uncertainty at the top-right in the panel.

3.1.2 Color Evolution

In Figure 11, we show the color evolution of SN 2014dt. The $B-V$ evolution of SN 2014dt is similar that of SN 2005hk until $\sim$80 days. After about 130 days, the color evolution changes. The $B-V$ evolution becomes redder. On the other hand, the evolution in NIR is almost constant. The color evolution of normal SN Ia 2003hv is almost bluer than that of SNe Iax. In the color about $\sim$300 days in NIR, the $J-H$ color of SN 2014dt is comparable to that of SN 2003hv. The details are discussed in §3.1.6.

3.1.3 Spectral Evolution

Figure 12 shows optical spectra of SN 2014dt from 21 days through 412 days. The early phase spectra are characterized by absorption lines of Na I D, Fe II, Co II, and the Ca II IR triplet (Branch et al. 2004; Jha et al. 2006; Sahu et al. 2008). The line identification is partly in debate due to non-negligible line blending (see below). The line of Si II λ6355 is likely hidden by that of Fe II λ6456 at 21 days. These lines are usually seen in SNe Iax at similar epochs. The spectral features of SN 2014dt at 21 – 64 days closely resemble those of SN 2005hk at similar epochs, except that the line width (and the blueshift) of each absorption feature in SN 2014dt is slightly narrower (and smaller) than those in SN 2005hk. This suggests that SN 2014dt had a smaller expansion velocity in the early phase. In Figure 13, we compare the line velocities of Fe II λ6149 and λ6247 lines in SN 2014dt with those in other SNe Iax. We measured the velocities by a Gaussian fit to each absorption line. In each feature, we measured it multiple times. The scatter of the line velocities among the multiple measurements is typically $\sim$400 km s^{-1}. The derived velocity was roughly 4000 km s^{-1} at 21 days and decreased to 2000 – 3000 km s^{-1} at 100 – 120 days. This is slower than those of SNe 2002cx, 2005hk and 2012Z, whereas it

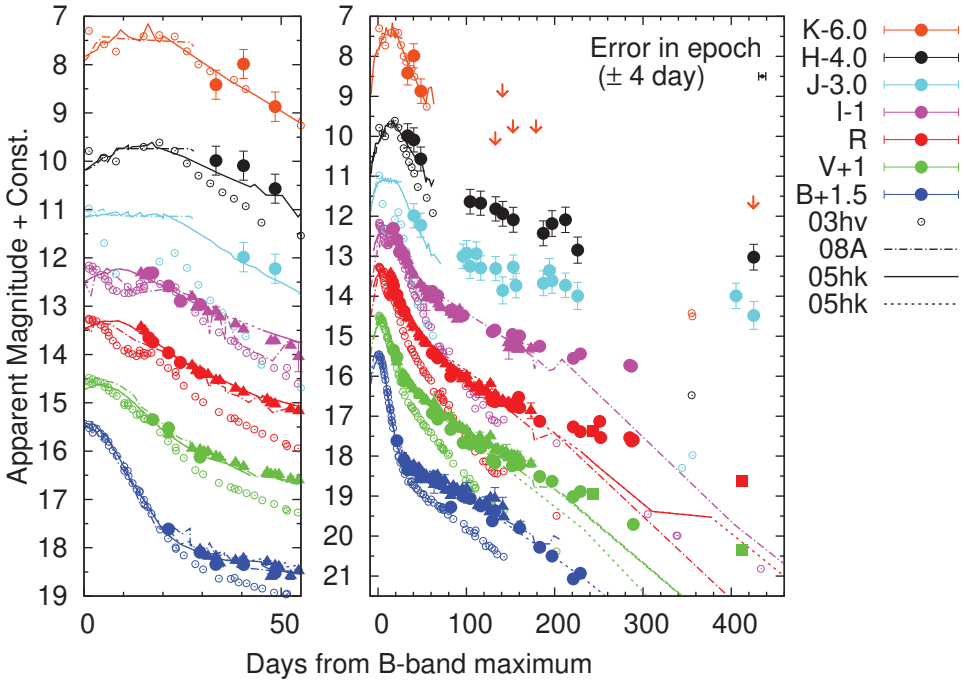

Figure 9: Multi-band light curves of SN 2014dt compared with SNe Iax 2005hk, 2008A and normal SN Ia 2003hv. In the left panel, we show the enlarged light curves for the early phase ($\lesssim$60 days). We show the light curves of SN Iax 2005hk with solid lines (or dashed ones in cases where separation to the neighboring point is $\gtrsim$100 days) ($BVRIJHKs$-bands and $F606W$-band; Phillips et al. 2007, Sahu et al. 2008, Friedman et al. 2015, McClelland et al. 2010, Stritzinger et al. 2015, Krisciunas et al. 2017) and SN 2008A ($BVRI$, $r'i'$ and $F555W, F622W, F625W, F791W, F775W$-bands) with dashed-dotted lines (McClelland et al. 2010, Hicken et al. 2012, Silverman et al. 2012b, Brown et al. 2014, Friedman et al. 2015) and SN Ia 2003hv with the open circles (Leloudas et al. 2009).

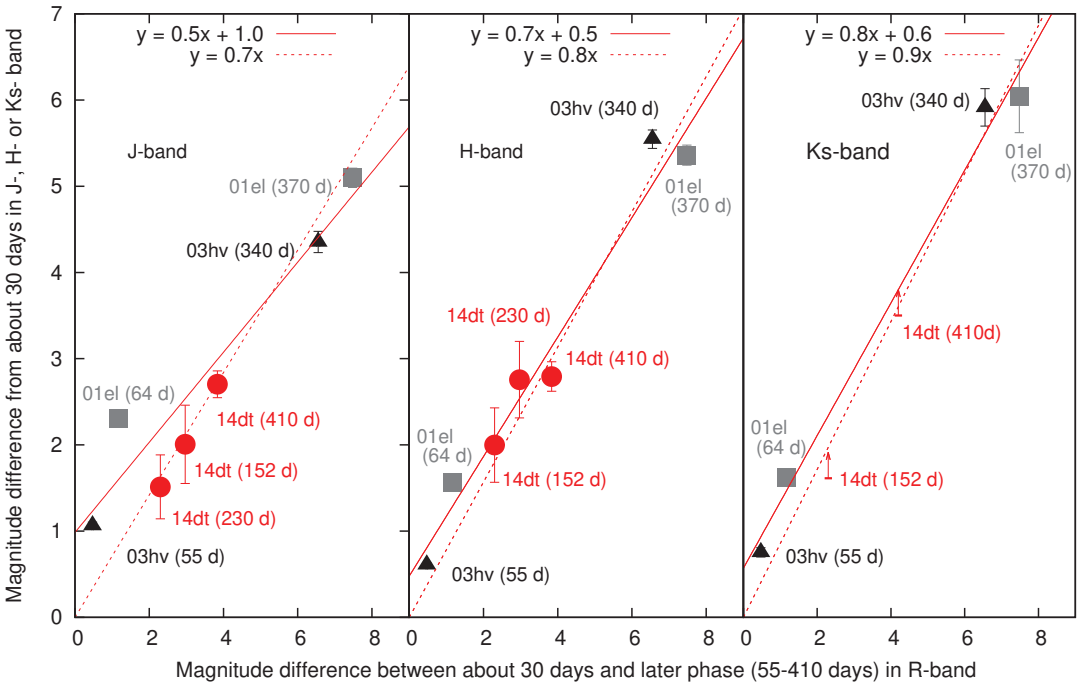

Figure 10: Relationship between the long-term decline rates in the optical and NIR bands for SN 2014dt. The decline rate is measured from ∼30 days to a given epochs (152, 230 and 410 days) in the late phase. The epochs, as measured from the maximum light, are plotted in parentheses in the figure. For comparison, we plotted those of normal, non-dust forming SN Ia 2003hv at 55 and 340 days as black (Leloudas et al. 2009) and SN 2001el at 64 and 370 days as gray (Krisciunas et al. 2003, Stritzinger & Sollerman 2007). The data points were approximately aligned along straight lines suggesting that the long-term decline is homogeneous over optical and NIR bands and that no clear sign of NIR excess was found in SN 2014dt at 230 – 410 days when the MIR excess was observed.

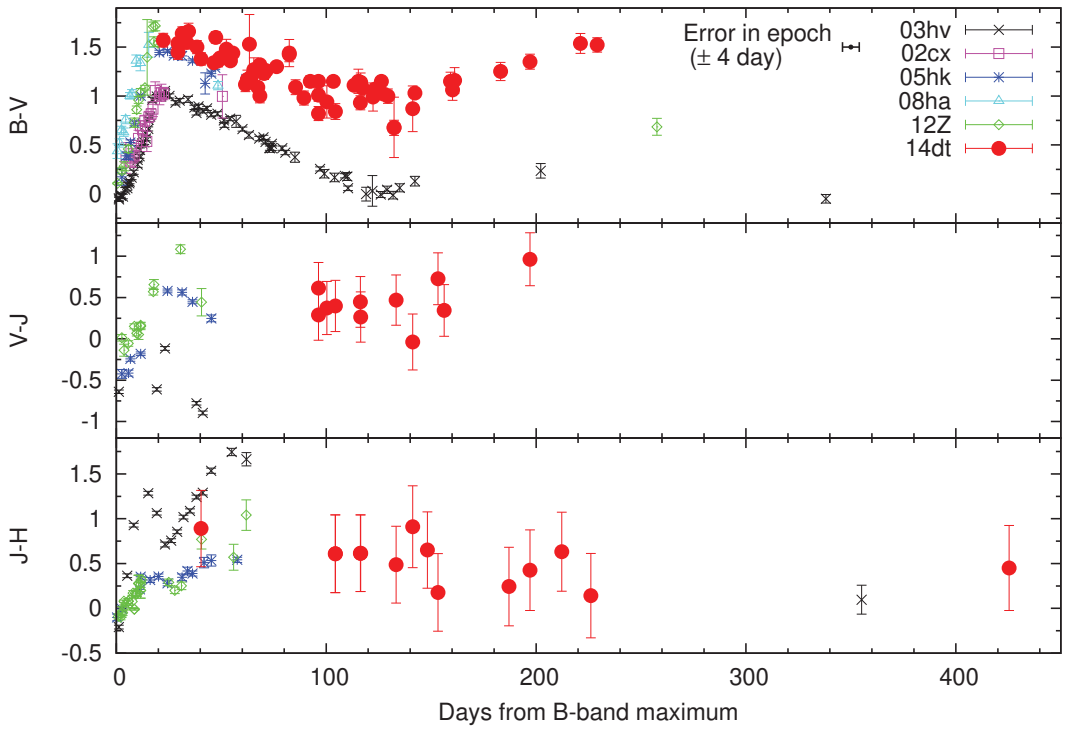

Figure 11: $B-V$, $V-J$ and $J-H$ color evolutions of SN 2014dt. We show those of SNe 2002cx (Li et al. 2003), 2005hk (Sahu et al. 2008), 2008ha (Foley et al. 2009), 2012Z (Yamanaka et al. 2015) and 2003hv (Leloudas et al. 2009). The color has already been corrected for Milky Way and the host galaxy extinctions.

is slightly faster than those of SNe 2009ku (Narayan et al. 2011) and 2014ck (Tomasella et al. 2016).

Here, we should be careful in the treatment of line velocities, because the spectra of SNe Iax show many intermediate-mass and Fe-group elements, and it is thus difficult to identify individual lines (e.g., Szalai et al. 2015) even with the less line blending due to the slower expansion than normal SNe Ia. We synthesized model spectra using *SYN++* code (Thomas et al. 2011) to provide reliable line identifications. The synthetic spectrum is likely to be consistent with the overall features in the observed spectrum (Figure 14). At around 6000 Å, the spectral lines of Fe II likely dominate the observed features, and Fe II λ6149 and λ6247 do not significantly suffer from contamination by other lines (e.g., Co II) as suggested in previous studies (i.e., Stritzinger et al. 2014 for SN 2010ae and Szalai et al. 2015 for SN 2011ay). This supports the idea that the slower expansion of SN 2014dt seen in Figure 13 is real in nature.

In the late phase, at 244 and 412 days, the spectra are characterized by many narrow emission lines (Figure 15). Many permitted lines, such as Fe II, and Ca II, are seen in addition to forbidden lines, such as [Fe I] λ7155 and [Ca II] $\lambda\lambda$7291, 7324. The spectral features at 241 days are still quite similar to those of SN 2005hk at 232 days except for some minor differences, such as the line ratios among emission lines around 8400 – 8700 Å and the width and blueshift of the Na I D absorption line. Generally, the strength ratio of a forbidden line to a permitted one is an index of the density of the line-emitting region; a smaller ratio indicates a larger density (e.g., Li & McCray 1993). We derived the strength of the emission lines simply by a single-Gaussian fit to each line profile. In the spectrum of SN 2014dt at 244 days, the ratio of [Ca II] $\lambda\lambda$7291, 7324 to Ca II λ8542 was 0.7 ± 0.1, whereas that in the spectrum of SN 2005hk at 228 days was much larger, 2.5 ± 0.1. This suggests that the density of the line emitting region in SN 2014dt is higher than that in SN 2005hk.

The spectral evolution through $\simeq$410 days is markedly different between SNe 2014dt and 2005hk. SN 2014dt showed no significant change except that some Fe II lines at the shorter wavelengths become weaker. However, in SN 2005hk, the forbidden lines ([Fe I] λ7155 and [Ca II] $\lambda\lambda$7291, 7324) become stronger relatively to the continuum and most emission lines become narrower. These indicate that the spectral evolution of SN 2014dt in the late phase was slow, which is likely consistent with the slow decline of the optical and NIR luminosity.

3.1.4 Estimation of the Maximum Epoch

It is useful to restrict the epoch of maximum brightness even roughly for comparison with other SNe and theoretical models. We emphasize that the main arguments in this thesis are based on the long-term evolution through the late phase, and thus uncertainty in the maximum epoch and explosion date in several day scale do not alter our main conclusions. However, some of our additional arguments depend on the epoch of maximum brightness. In this subsection, we describe how we estimated the maximum epoch from the observational data of SN 2014dt, for which the maximum date is indeed missing.

Figure 16 shows a spectral comparison of SN 2014dt and other SNe Iax. The spectrum of SN 2014dt on November 10 shows a close resemblance to those of SNe 2002cx at 21 days, 2005hk at 22 days and 2012Z at 21 days. The absorption lines of SNe 2008ha and 2010ae are much narrower; however, the overall spectral features are still similar to those of other SNe Iax at similar epochs. This spectral comparison could provide a tentative estimation of the epoch of SN 2014dt: 2014 November 10 was around 21 – 22 days after the maximum light.

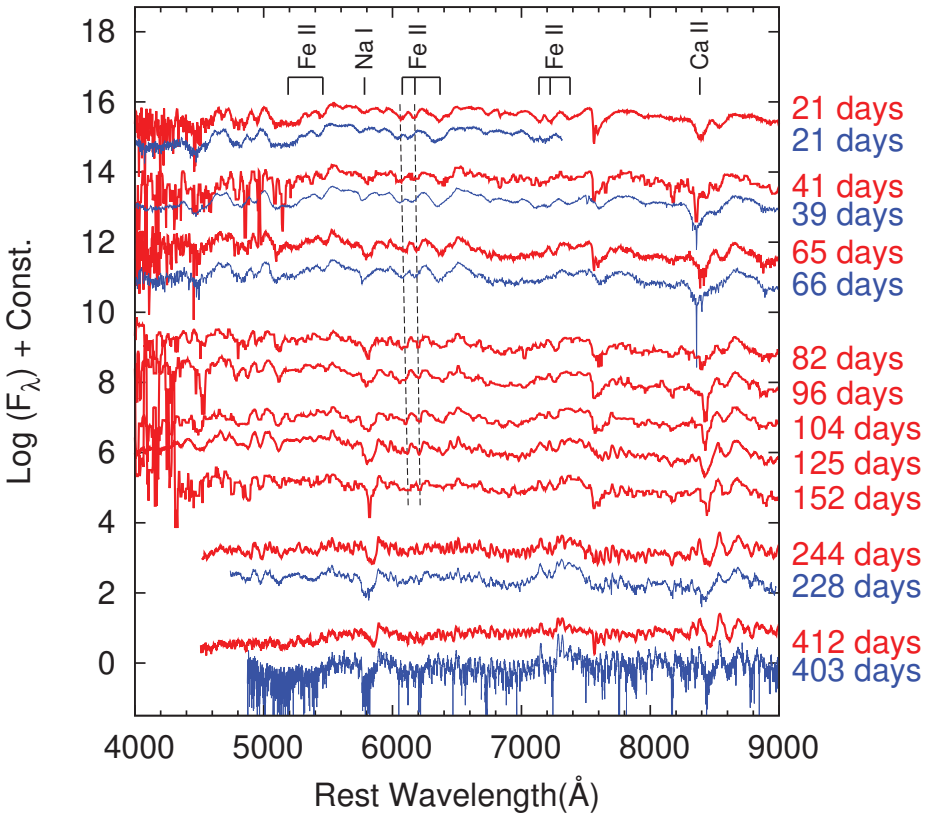

Figure 12: Spectral evolution of SN 2014dt (red solid lines). The epoch of each spectrum is indicated on the right outside of the panel. The vertical dashed lines show the positions of Fe II λ6149 and λ6247 lines. For comparison, we plotted the spectra of SN 2005hk (blue lines; Phillips et al. 2007, Sahu et al. 2008, Blondin et al. 2012, Silverman et al. 2012b).

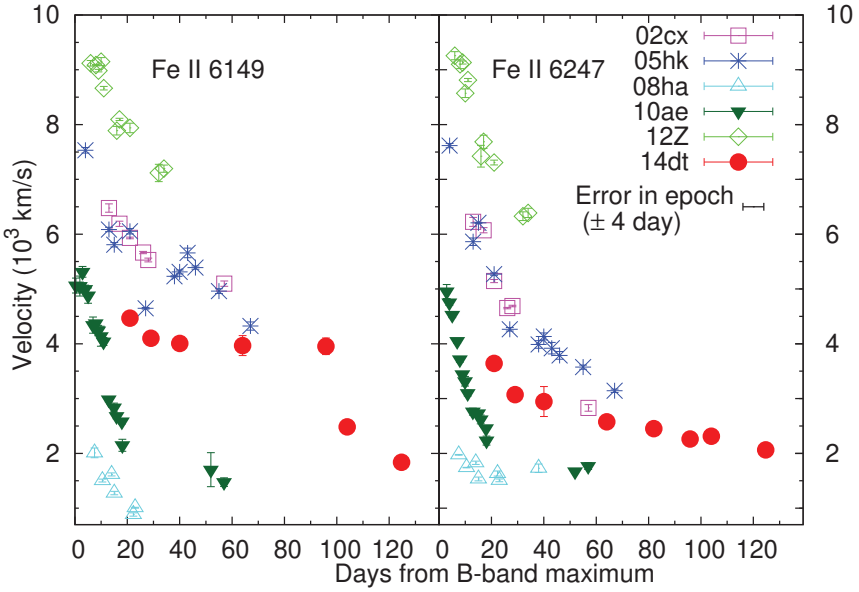

Figure 13: Line velocities of Fe II λ6149 and λ6247 in SN 2014dt. For comparison, we plotted those in SNe Iax 2002cx (Li et al. 2003), 2005hk (Phillips et al. 2007; Blondin et al. 2012; Silverman et al. 2012b), 2008ha (Foley et al. 2009; Valenti et al. 2009), 2010ae (Stritzinger et al. 2014) and 2012Z (Stritzinger et al. 2015; Yamanaka et al. 2015). We measured the velocity of the comparison SNe in the same way as for SN 2014dt.

Next, we considered an estimation of the epoch based on the LCs. Indeed, the multi-band LCs of SN 2014dt apparently closely followed those of SNe 2002cx, 2005hk, and 2012Z in the post-maximum phase, until ∼80 days after the explosion. In this period, the extinction-corrected colors and the spectra of SN 2014dt also resembled those of SNe 2002cx, 2005hk and 2012Z except for a slightly slower expansion velocity (see §3.1.3). These data may allow us to conclude that the multi-band LCs of SN 2014dt even before the discovery were similar to those of SNe 2002cx, 2005hk and 2012Z. To further quantify the similarity and provide a reasonable estimate on evolution of the LCs of SN 2014dt before the discovery, and we examined whether and how the multi-band LCs of these template SNe matched to those of SN 2014dt. The details are given in the Appendix B. Here we provide a summary of our analyses.

First, the initial guess of the phase was set so that it was 21 days after the maximum light on 2014 November 10. For a template LC of each SN in each bandpass, we gave artificial shifts along the time axis Δt and the magnitude axis ΔM within given ranges ($|\Delta t| \leq 10$ days and $|\Delta M| \leq 0.3$ mag). For each set of Δt and ΔM, we computed the sum of the magnitude difference between the SN 2014dt and the hypothesized template LC between the discovery date of SN 2014dt and 60 days after the discovery. Then, we estimated the plausible ranges of Δt and ΔM requiring that the difference should be smaller than a given specific value. Performing the same procedure independently for $BVRI$-band LCs, we determined the plausible range of Δt and ΔM so that the fits in all of the bands were mutually consistent. However, we found that the multi-band LCs of SN 2002cx did not provide a consistent solution among different bands; thus we concluded that the LCs of SN 2002cx should be omitted from the template LCs. As a result, we had a series of 'combined' LCs for SN 2014dt, in which the pre-discovery part

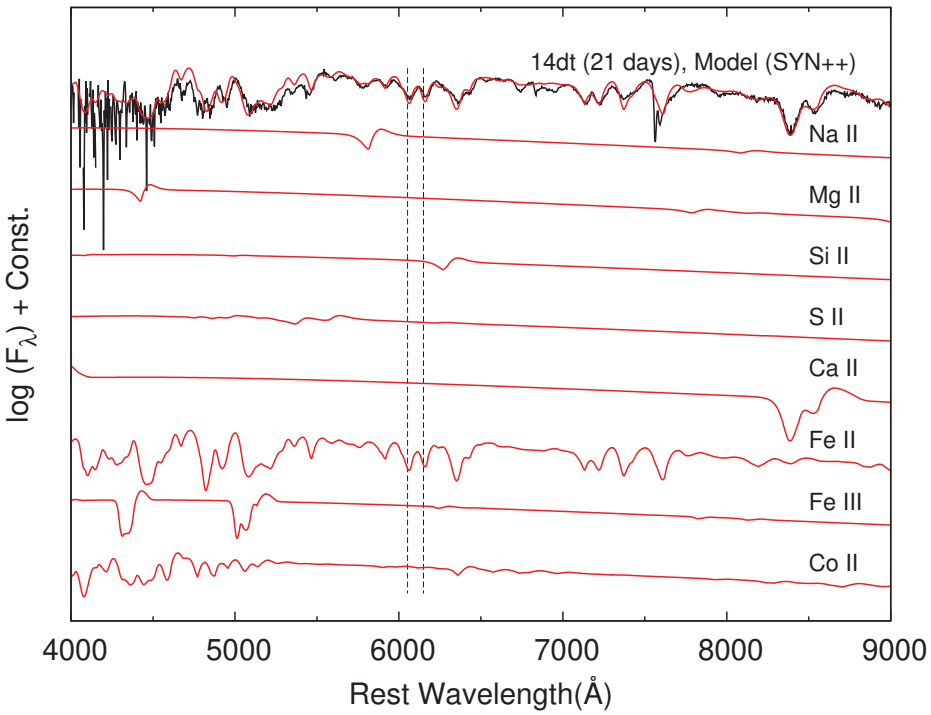

Figure 14: Comparison of the observed spectrum for SN 2014dt at 21 days (black line) and the synthesized spectra calculated with *SYN++* code (red lines). We also show the synthesized spectra of each species indicated in the panel. The vertical dashed lines show the positions of Fe II λ6149 and λ6247 lines. It is likely that Fe II λ6149 and λ6247 are little blended with other species (see text).

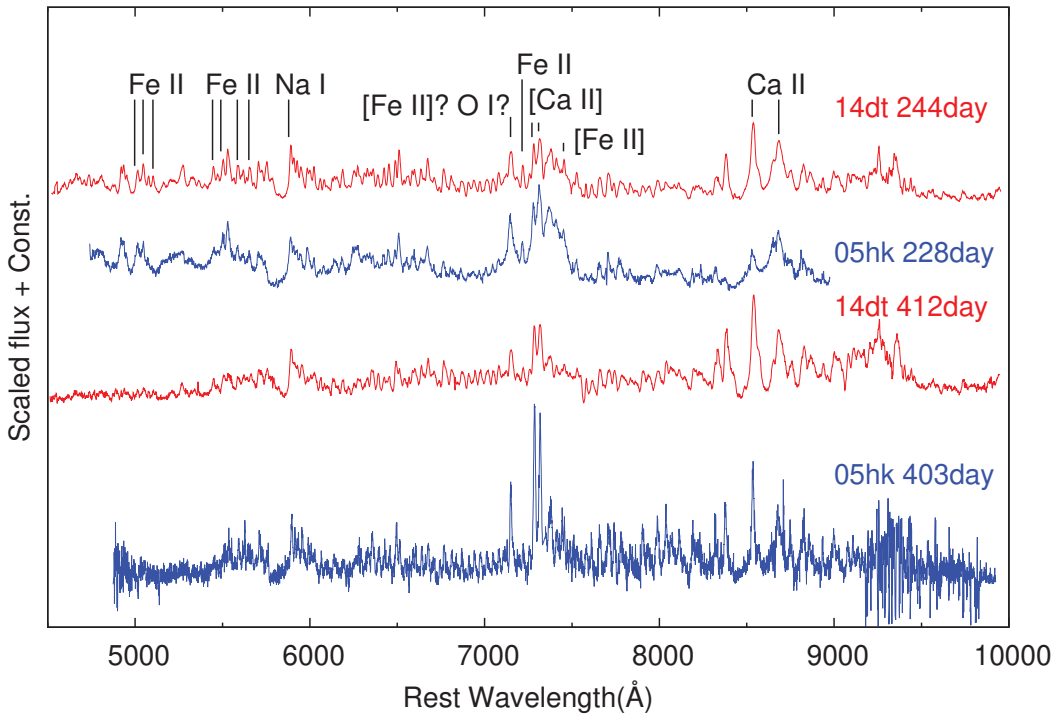

Figure 15: Comparison of the late phase spectra for SNe 2014dt (red solid lines) and 2005hk (blue solid lines; Sahu et al. 2008, Silverman et al. 2012b).

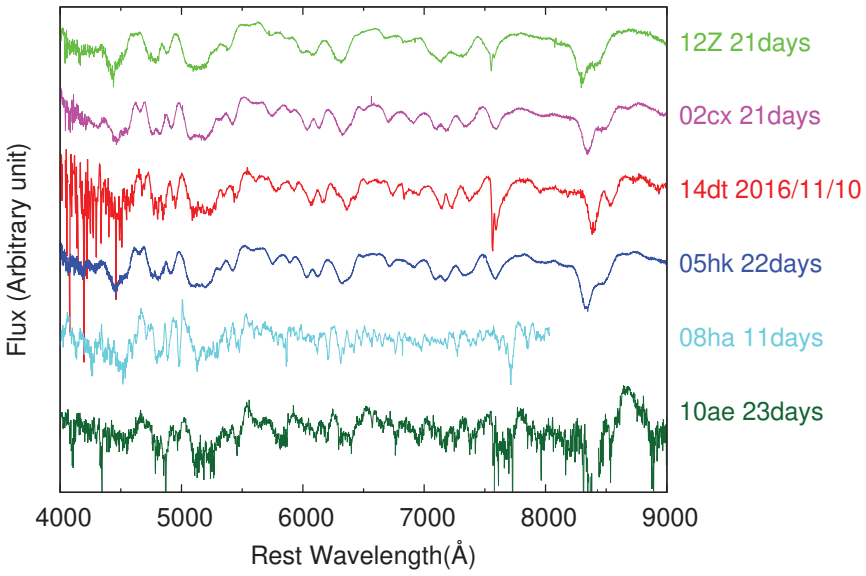

Figure 16: Spectral comparison of SN 2014dt on 2016 November 10 with other SNe Iax; 2012Z (Stritzinger et al. 2015), 2002cx (Li et al. 2003), 2005hk (Blondin et al. 2012), 2008ha (Foley et al. 2009), and 2010ae (Stritzinger et al. 2014). The phase of each spectrum is ∼20 days except for SN 2008ha for which no spectrum at ∼20 days was available.

was replaced by the LC of either SN 2005hk or SN 2012Z, taking into the uncertainty in Δt and ΔM into account. Further details are written in Appendix B. Thus, we derived the epoch of B-band maximum as MJD 56950.4 ± 4.0 (2014 October 20.4 UT), which was in accordance with the results of the spectral comparison and the also with the previous estimate (Foley et al. 2015; Fox et al. 2016; Singh et al. 2018).

3.1.5 Maximum Magnitude v.s. Decline Rates

For the 'combined' LCs constructed in §3.1.4 (see also Appendix B), we estimated the maximum magnitude and the decline rate, Δm_{15}, as well as the epoch of the maximum light in each of the VRI-band (Table 5). After correcting the distance modulus and the total extinction (see §2.1.1), we derived the absolute maximum magnitude in the B-band, $M_{B,\mathrm{max}} = -16.82$–$-17.34$ mag. The derived $M_{B,\mathrm{max}}$ for SN 2014dt is slightly (0.2–1.2 mag) fainter than those of SNe Iax 2002cx ($M_{B,\mathrm{max}} = -17.55 \pm 0.34$ mag; Li et al. 2003), 2005hk ($M_{B,\mathrm{max}} = -18.02 \pm 0.32$ mag; Phillips et al. 2007, $M_{B,\mathrm{max}} = -18.00 \pm 0.25$ mag; Stritzinger et al. 2015), and 2012Z ($M_{B,\mathrm{max}} = -18.27 \pm 0.09$ mag; Stritzinger et al. 2015, $M_{B,\mathrm{max}} \sim -17.61$ mag; Yamanaka et al. 2015 [5]), whereas it was 3.1–3.6 mag brighter than that of SN 2008ha ($M_{B,\mathrm{max}} = -13.74 \pm 0.15$ mag; Foley et al. 2009, $M_{B,\mathrm{max}} = -13.79 \pm 0.14$ mag; Stritzinger et al. 2014). It is noted that this estimate conservatively included the uncertainty in the 'combined' LCs in terms of the template LCs (SN 2005hk or SN 2012Z) and the fitting uncertainties in Δt and ΔM.

[5]The difference in the reported absolute magnitudes is due to the different values of the distance modulus and the dust extinction adopted in the two studies. Stritzinger et al. (2015) adopted $\mu = 32.59 \pm 0.019$ mag and $E(B-V) = 0.11 \pm 0.03$ mag. On the other hand, Yamanaka et al. (2015) adopted $\mu = 32.4 \pm 0.3$ mag and $E(B-V) = 0.036$ mag.

Table 5: Peak magnitude and its epoch of SN 2014dt in each photometric band

Band	Maximum date (MJD)	Maximum magnitude	Δm_{15}
B	56950.4 ± 4.0	13.88–13.76	1.43–1.57
V	56954.9 ± 4.0	13.56–13.50	0.73–0.91
R	56957.5 ± 4.0	13.47–13.28	0.51–0.66
I	56958.5 ± 4.0	13.63–13.30	0.48–0.66

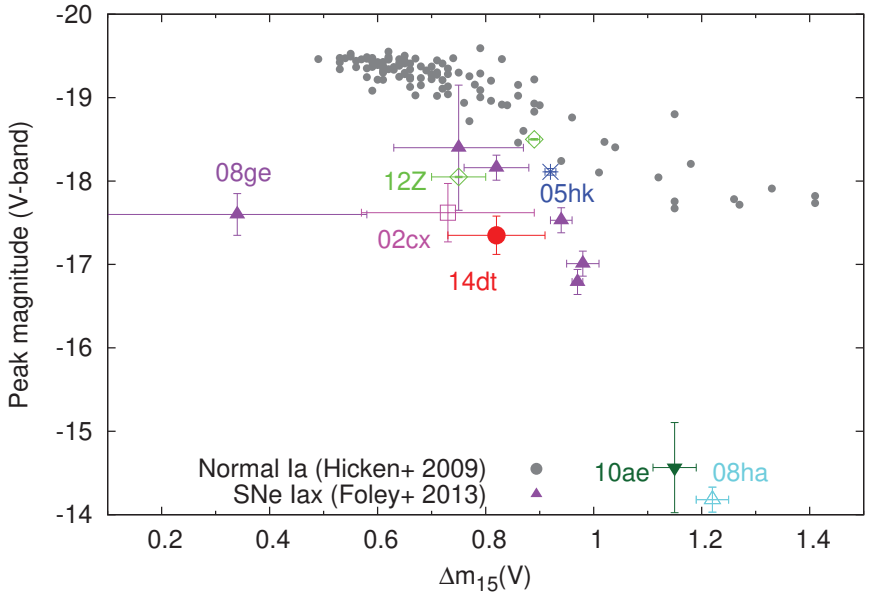

Figure 17: Corrected peak absolute magnitudes in the V-band with the decline rate $\Delta m_{15}(V)$. The gray filled circles are the data points of normal SNe Ia (Hicken et al. 2009), and the other symbols are for SNe Iax (Li et al. 2003; Foley et al. 2009; Foley et al. 2013; Stritzinger et al. 2014; Stritzinger et al. 2015; Yamanaka et al. 2015). For some SNe Iax, the SN IDs are indicated one by one.

The derived decline rate of SN 2014dt is $\Delta m_{15}(B) = 1.43$–1.57 mag. As shown in Table 5, the decline rate was smaller at longer wavelengths. Figure 17 shows the relationship between $M_{V,\mathrm{max}}$ and $\Delta m_{15}(V)$ in some SNe Iax and normal SNe Ia. SN 2014dt apparently belonged to the group of the bright SNe Iax including SNe 2002cx, 2005hk and 2012Z. From 60 through 410 days, the differences in LCs from those of SN 2005hk became significant (Figure 9); SN 2014dt showed a slower decline than SN 2005hk. This is confirmed in Figure 18 where the 'long-term decline rates' (0 to 200–250 days) in the B-band are plotted. Among three SNe Iax for which B-band photometric data at 200–250 days exist SN 2014dt showed the smallest long-term decline rate, and the smallest compared to larger samples of normal SNe Ia. We found no clear trend between the absolute maximum magnitude and the long-term decline rate among SNe Iax samples and also among normal SNe Ia samples. The large error in $\Delta m_{200-250}(B)$ stems from our conservative error estimated in the maximum magnitude. Indeed, it is clear from Figure 9 that the LCs of SN 2014dt are much flatter in the late phase than those of SN 2005hk.

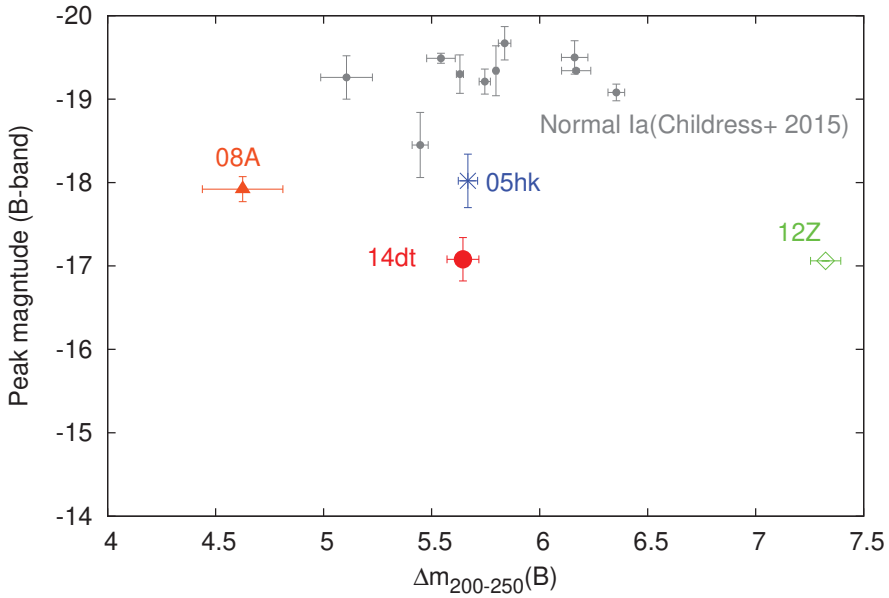

Figure 18: Correlation between the peak absolute magnitudes in the B-band and the long-term decline rate; that is, the magnitude difference between 0 and 200 – 250 days after the maximum light in the B-band. The data for normal SNe Ia are from Sandage et al. (1996), Suntzeff et al. (1999), Pignata et al. (2004), Anupama et al. (2005), Pastorello et al. (2007), Pignata et al. (2008), Richmond & Smith (2012), Kawabata et al. (2014), Zhang et al. (2014), Childress et al. (2015), and Graham et al. (2015).

3.1.6 Spectral Energy Distribution

Our observations may provide the first opportunity to examine the long-term, optical and NIR multi-band photometry for SNe Iax, which enables us to study the evolution of SED through the late phase, including any possible contribution from circumstellar (CS) dust. At longer wavelengths, Fox et al. (2016) reported that SN 2014dt showed brightening around 300 days at mid-infrared (MIR) wavelengths and suggested that thermal emissions from pre-existing, irradiated dust grains could cause the MIR excess.

We derived SEDs of SN 2014dt by combining the optical and NIR photometric data at similar epochs (difference $\lesssim$14 days), and plotted them in Figure 19 together with representative blackbody (BB) spectra. The BB temperature is roughly an indicator of the photospheric temperature. Initially (between 40 days and 132 days) the BB temperature seemed to decrease rapidly from $\sim$5000 K to $\sim$3700 K, but thereafter the BB temperature showed no significant change through 410 days, whereas the peak flux gradually decreased. For some SNe Iax, McCully et al. (2014b) pointed out that temperature evolution obtained by the ratio of the permitted Ca II lines is slower than t^{-1} or even constant. This might be commonly seen in SNe Iax. However, the fluence (λF_λ) at MIR wavelengths gradually increased during the period of 309 – 336 days (Fox et al. 2016), although it was still much smaller than those in optical and NIR wavelengths. The spectral slope of the MIR excess was inconsistent with the main SED component peak at optical wavelengths, and thus the MIR excess would only represent a minor, additional component.

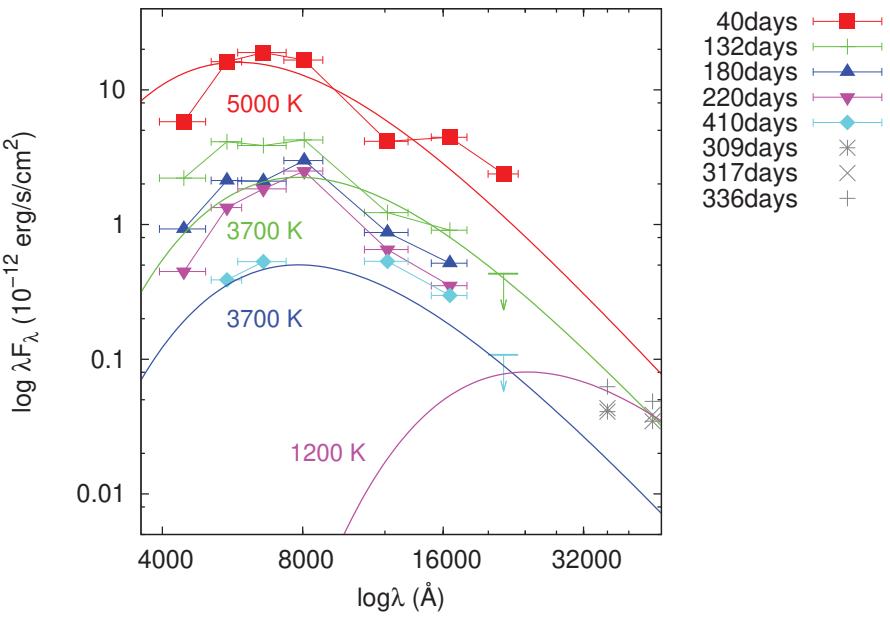

Figure 19: The evolution of the SED of SN 2014dt. For data at 180, 220, and 410 days, we plotted the combined data at similar epochs (difference $\lesssim$14 days) because we did not always have the data exactly at the same epoch. The data at mid-infrared wavelengths (the gray points) are from Fox et al. (2016). For comparison, we plotted the blackbody spectra for 5000, 3700, and 1200 K by the solid lines.

3.2 Discussion

3.2.1 Interpretation of the SED Evolution

As shown in Figure 19, the main SED component ($\sim$3700 K BB emission) dominated the optical and NIR flux from 180 days to 410 days. This long-lasting SED component could be an analog to the component that Foley et al. (2015) found for SN 2005hk by continuum fits to late phase spectra. The authors suggested that the long-lasting photospheric emission could have originated in the wind launched from a bound remnant in a context of the weak deflagration model. It is plausible that this photospheric emission component correspond to the main SED component derived for SN 2014dt.

The combination of the bolometric luminosity and the temperature obtained through the SED fitting suggests that the radius of the photosphere is $R_{\rm ph} \sim 6.2 \times 10^{14}$ cm at 230 days. Assuming that the bolometric luminosity follows the ^{56}Co decay, then the nearly unchanged temperature suggests $R_{\rm ph} \sim 2.9 \times 10^{14}$ cm at 410 days, i.e., the photospheric radius has decreased by about a factor of two from 230 days to 410 days. Assuming that the opacity is 0.1 cm^2 g^{-1}, then $R_{\rm ph}$ at 230 days suggests that $\sim 8 \times 10^{-3} M_\odot$ of the material is confined within this radius. If the photosphere could be located within the homologously expanding inner ejecta (that is the expansion velocity is proportional to the radius), then the corresponding velocity is $\sim$300 km s^{-1} and $\sim$80 km s^{-1} at 230 and 410 days, respectively. To compare to these values of the velocity, the late phase spectra at 232 and 412 days show some permitted lines whose widths are marginally resolved by our spectroscopic observations. Given the resultant wavelength resolution of 650, the velocities of these permitted lines should be an order of 100 km s^{-1}, while the precise measurement is not possible. In the discussion below, we just use the rough

value (a few 100 km s^{-1}) in a qualitative way.

The photospheric radius far exceeds the size of a red supergiant, and therefore it is unlikely that this is created by a (nearly hydrostatic) atmosphere of a hot (remnant) WD within the weak deflagration model. The overall feature may be consistent with the model that the photosphere is located deep in the homologously expanding ejecta, as the inferred velocity is consistent with those measured in the spectra but within the spectral resolution. Indeed, Foley et al. (2015) argued against this interpretation the photosphere in the ejecta for SN 2005hk, by pointing out the discrepancy (in a snapshot spectrum) in the velocities measured in these two different approach. If the photosphere is in the homologously expanding ejecta, it predicts that the associated line velocity decreases as time goes by (see above, i.e., by a factor of nearly 4 from 200 to 400 days), and thus an accurate measurement of the line velocities and their evolution is a key in testing this scenario with the photosphere located deep in the ejecta. This scenario on the other hand naturally explains the decrease in the photospheric radius, as the density of the emitting material decreases.

Alternatively, the photosphere might have formed within the wind lunched by the possible remnant bound to the incompletely burned WD, as suggested by Foley et al. (2015) for SN 2005hk. In this case, a line velocity has no direct link to the photospheric radius but determined by the velocity of the wind. Still, it should be an order of at least 100 km s^{-1} to create the photosphere at $R > 10^{14}$ cm. The mass within the photosphere ($\sim 8 \times 10^{-3} M_\odot$ as measured at 230 days) is translated to the wind mass loss rate of $\sim 10^{-2} M_\odot$ yr^{-1}, and the kinetic power of $\sim 3 \times 10^{37}$ erg s^{-1} to 10^{39} erg s^{-1} for the wind velocity of $\sim$100 – 1000 km s^{-1}. This is roughly the Eddington luminosity for the expected bound remnant, thus is in line with the wind scenario. A possible drawback of the wind scenario is that there is no obvious reason about why the photosphere radius has been decreased, as the 'stationary wind' would not provide a change in the density scale to change the position of the photosphere.

In summary, it is not possible to make a strong conclusion on the origin of the photospheric component. Both of the ejecta model and the wind model have advantage and disadvantage. In any case, we add several new constraints on the nature of this emission to the suggestion by Foley et al. (2015); for example, any model should explain the recession of the photosphere, and the mass of the material must be at least $\sim 10^{-3} M_\odot$. In either case, the need of the high-density material in the inner part of the ejecta could support the weak deflagration model and the existence of the bound remnant.

3.2.2 Interpretation of the MIR Excess

Here we briefly discuss the origin of the minor MIR excess. Foley et al. (2015) suggested that the emission from circumstellar dust seems unlikely, because neither additional reddening nor narrow absorption lines due to a possible circumstellar interaction has been observed in late phase optical spectra of SNe Iax. They further argued against thermal emission from newly formed dust grains within the ejecta, based on the lack of expected signatures such as the blueward shift of the spectral lines and additional reddening. Alternatively, the authors suggested that the emission from a bound remnant with a super-Eddington wind is plausible as a source of the MIR excess. However, as shown above, the main component that we derived for SN 2014dt was indeed an analog to what Foley et al. (2015) suggested for SN 2005hk, representing a possible bound remnant. By this component alone, it is hard to explain the MIR excess.

Thus, we speculate that an echo by CSM is the most likely interpretation of the MIR excess. This would not contradict the lack of strong extinction and narrow emission lines.

For example, the CSM of the over-luminous SN Ia 2012dn is likely to be located off the line of sight, and the separation between the CSM and the SN is too far to allow a strong interaction within the first few years after the explosion (Yamanaka et al. 2016; Nagao et al. 2017). A similar configuration may apply to the case of SN 2014dt.

As mentioned in §3.1.6, the MIR excess only provided a minor contribution to the SED. However, it may not be negligible in the K_s-band at 410 days if the continuum from a hot dust ($\sim$1200 K) is the origin of the MIR excess and it may contaminate the NIR fluxes (see Figure 19). Thus, it is interesting to check the possible contamination in our NIR data. If the possible additional component to the intrinsic SN emission in the NIR bands exists, the data point should be significantly lower than the straight lines in Figure 10. Thus, we exclude the existence of the additional component in the NIR bands, and the dust should not be hot (i.e., $\lesssim$1200 K) if thermal emissions from dust is the origin of the MIR excess.

3.2.3 Two-component Fit to the Bolometric LC: A Support to the Weak Deflagration Model with a Bound Remnant

We derived the bolometric luminosity of SN 2014dt assuming that the sum of fluxes in the $BVRI$-bands occupied about 60 % of the bolometric one (Wang et al. 2009). The derived bolometric LC is shown in Figure 20, which is one of the 'combined LCs', with the template LCs taken from SN 2005hk and $\Delta t = 0$ days (see §3.1.4 and Appendix B). In the early phase, SN 2014dt was 0.1–0.5 dex fainter than SNe 2002cx, 2005hk, and 2012Z. SN 2014dt showed a significantly slow decline after $\sim$ 60 days, and then its luminosity became comparable with that of SN 2005hk as well as $\sim$ 0.5 dex brighter than that of SN 2012Z at 230–250 days. With the peak luminosity ($L_{\rm bol,max}$) and rising time (t_r), we could estimate the mass of the synthesized ^{56}Ni (Arnett 1982; Stritzinger & Leibundgut 2005). The rising part of the LC in SN 2014dt was not observed. SNe Iax show larger diversity, but it is pointed out that the rising time of SNe Iax has a correlation with the peak magnitude (Magee et al. 2016). SN 2014dt is slightly fainter than SNe 2005hk and 2012Z, and it might be not a clear outlier like SN 2007qd (McClelland et al. 2010; Magee et al. 2016). We assume that the rinsing time of SN 2014dt is roughly similar to those of SNe 2005hk and 2012Z. Adopting SN 2005hk and 2012Z as a template, we tested a range of rising times to estimate the ^{56}Ni mass. The definition of the rising time can differ in different literatures, so we decided to check and derive the rising time ourselves. We fitted each of the multi-band LCs of SNe 2005hk and 2012Z by a quadratic function, deriving rising times, and t_r = 16.5–21.0 and 11.8–12.8 days for SNe 2005hk and 2012Z, respectively, which are consistent with those in previous papers within the given ranges. Using $L_{\rm bol,max}$ = (1.2–1.8) $\times 10^{42}$ erg s^{-1} and t_r = 11.8–21.0 days, we estimated the ^{56}Ni mass as 0.04–0.10M$_\odot$ for SN 2014dt. It unfortunately has a large uncertainty, because the data around the maximum light are missing for SN 2014dt, but it is still useful for discussion on the energetics (see §3.2.5).

We also estimated the ^{56}Ni mass from the late phase bolometric LC, which is only subject to little and negligible much less contamination by the error of the explosion epoch. First, we estimated the ^{56}Ni mass by a fit of a simple radioactive-decay LC model in the late phase (e.g., Maeda et al. 2003),

$$\begin{aligned} L_{\rm bol} &= M(^{56}{\rm Ni}) \left[e^{(-t/8.8\ {\rm d})} \epsilon_{\gamma,{\rm Ni}} (1 - e^{-\tau}) \right. \\ &\quad \left. + e^{(-t/111\ {\rm d})} \left\{ \epsilon_{\gamma,{\rm Co}} (1 - e^{-\tau}) + \epsilon_{e^+} \right\} \right], \text{ and} \end{aligned} \tag{3.1}$$

$$\tau \simeq 1000 \times \left[\frac{(M_{\rm ej}/M_\odot)^2}{E_{51}} \right] (t\ {\rm day})^{-2}\ , \tag{3.2}$$

where $\epsilon_{\gamma,\mathrm{Ni}} = 3.9 \times 10^{10}$ erg s^{-1} g^{-1} is the energy deposition rate by ^{56}Ni via γ-rays, $\epsilon_{\gamma,\mathrm{Co}} = 6.8 \times 10^{9}$ erg s^{-1} g^{-1} and $\epsilon_{e^+} = 2.4 \times 10^{8}$ erg s^{-1} g^{-1} are those by the ^{56}Co decay via γ-rays and positron ejection, M_{ej} is the ejecta mass, and E_{51} is the kinetic energy of 10^{51} erg. However, it does not consistently explain the derived bolometric LC at both and early and late phases. The slow tail in the obtained bolometric LC of SN 2014dt after ∼60 days required nearly a full trapping of the deposited energy (that is, a larger τ). However, the full trapping of γ-rays with ∼0.10 M$_\odot$ of ^{56}Ni / ^{56}Co (as derived above to fit the peak) should result in a much larger L_{bol} in the late phase (see Figure 20).

Thus, we adopted a two-component LC model (Maeda et al. 2003) where L_{bol} is a sum of $L_{\mathrm{bol,in}}$ and $L_{\mathrm{bol,out}}$. In this model, we have four independent parameters in total, $M_{\mathrm{in}}(^{56}\mathrm{Ni})$, $[(M_{\mathrm{ej}}/M_\odot)^2/E_{51}]_{\mathrm{in}}$, $M_{\mathrm{out}}(^{56}\mathrm{Ni})$ and $[(M_{\mathrm{ej}}/M_\odot)^2/E_{51}]_{\mathrm{out}}$. The former two parameters (subscripted by 'in') correspond to an inner, larger τ component, and the latter two correspond to the outer, smaller τ one. With this model, we successfully reproduced the LC which well traces the bolometric LC from near maximum light to ∼250 days as shown in Figure 20.

The parameters obtained by the fit were $M_{\mathrm{in}}(^{56}\mathrm{Ni}) = 0.015$–$0.025$ M$_\odot$, $[(M_{\mathrm{ej}}/M_\odot)^2/E_{51}]_{\mathrm{in}} \gtrsim 500$, $M_{\mathrm{out}}(^{56}\mathrm{Ni}) = 0.02$–$0.08$ M$_\odot$ and $[(M_{\mathrm{ej}}/M_\odot)^2/E_{51}]_{\mathrm{out}} \sim 0.8$–$3.0$. Again, we noted that the errors were conservatively associated with a series of the allowed combined LCs for SN 2014dt (§3.1.4), which is also the case for the following analyses. We could only estimate a rough lower-limit for $[(M_{\mathrm{ej}}/M_\odot)^2/E_{51}]_{\mathrm{in}}$ so that it was large enough to fully trap the γ-rays even at 250–410 days. That is, the need for the high-density inner component was robust and insensitive to the parameters for fit. At 410 days, the bolometric LC of SN 2014dt was slightly brighter than the two-component model LC. Contamination by the galaxy background was small in this phase (see Foley et al. 2015). If this excess was real, one possible explanation is the contribution from a scattering component of a presumed CSM echo, corresponding to the MIR excess (§3.2.1).

The existence of the large τ_{in} component suggests that there is an inner component that keeps a high density even in the late phase, regardless of the origin (see §3.2.1). This is consistent with the prediction of the weak deflagration model with a bound remnant (e.g., Fink et al. 2014).

3.2.4 Properties of Ejecta

In the two-component model, the inner, dense component may be connected with the existence of a bound WD, and the outer, less dense one may correspond to the SN ejecta. Assuming that the outer component ($[(M_{\mathrm{ej}}/M_\odot)^2/E_{51}]_{\mathrm{out}} \sim 0.8$–$3.0$) was the main ejecta, we could estimate M_{ej} and E_{k} of the ejecta in SN 2014dt by applying the scaling laws,

$$t_{\mathrm{d}} \propto \kappa^{1/2}\ M_{\mathrm{ej}}^{3/4}\ E_{\mathrm{k}}^{-1/4}, \text{ and} \tag{3.3}$$

$$v \propto E_{\mathrm{k}}^{1/2}\ M_{\mathrm{ej}}^{-1/2}, \tag{3.4}$$

calibrated with the well-studied SNe Ia, where t_{d} is the diffusion timescale (∼ width of the early LC peak), κ is the absorption coefficient for optical photons, and v is the typical expansion velocity of the ejecta. Here, we adopted the parameters derived for the well-studied SN Ia 2011fe (Pereira et al. 2013) for the normalization. From Equations 3.3 and 3.4, we obtained the following equations of the ratios in M_{ej} and E_{k},

$$\frac{M_{\mathrm{ej,14dt}}}{M_{\mathrm{ej,11fe}}} = \left(\frac{t_{\mathrm{d,14dt}}}{t_{\mathrm{d,11fe}}}\right)^2 \times \frac{v_{\mathrm{14dt}}}{v_{\mathrm{11fe}}} \times \frac{\kappa_{\mathrm{11fe}}}{\kappa_{\mathrm{14dt}}}, \text{ and} \tag{3.5}$$

$$\frac{E_{\mathrm{k,14dt}}}{E_{\mathrm{k,11fe}}} = \left(\frac{t_{\mathrm{d,14dt}}}{t_{\mathrm{d,11fe}}}\right)^2 \times \left(\frac{v_{\mathrm{14dt}}}{v_{\mathrm{11fe}}}\right)^3 \times \frac{\kappa_{\mathrm{11fe}}}{\kappa_{\mathrm{14dt}}}. \tag{3.6}$$

The expansion velocity of a SN Ia is usually estimated from the blueshift of the Si II λ6355 absorption line at $\sim$0 day (e.g., $v_{11fe} \simeq 10500$ km s^{-1}; Pereira et al. 2013). The Si II λ6355 absorption line of SN Ia is strong at $\sim$0 day and is little contaminated by other absorption lines (e.g, SN 2011fe; Parrent et al. 2012). However, we have no spectrum of SN 2014dt around the maximum light. In addition, it is often difficult to identify the Si II λ6355 line in the spectra of SNe Iax at 10 days and later. Thus, we estimated the Si II λ6355 line velocity, assuming that the ratio between the velocity of Si II λ6355 at $\sim$0 day and that of Fe II lines velocity at $\sim$20 days was similar among SNe Iax samples (i.e., SNe 2005hk, 2012Z and 2014dt). In SNe Iax, the Fe II λ6149 and λ6247 lines were not much blended (see §3.1.3). In this way, we estimated $v_{14dt} = 3500$–4200 km s^{-1}.

The diffusion timescale, t_d, approximately corresponds to the width of the peak in the bolometric LC. We derived the ratio of $t_{d,14dt}/t_{d,11fe}$ as 1.0–1.6, by comparing the durations for the two SNe from the maximum light to the epoch when the magnitude decreased by 0.5 dex.

For κ, it would not be safe to simply assume that the opacity of SN 2014dt is the same as that of SN 2011fe, because the properties of SN ejecta would be considerably different between SNe Iax and normal SNe Ia (i.e., $\kappa_{14dt} \neq \kappa_{11fe}$). Thus, we kept it as a free parameter and added another observational constraint using the post-maximum LC, when the LC is still dominated by the ejecta (that is, the outer component). With $E_{k,11fe} = 1.2 \times 10^{51}$ erg (Pereira et al. 2013) and $M_{ej,11fe} = 1.4$ M$_\odot$, we obtained $E_{k,14dt} = (0.07$–$0.42) \times 10^{50}$ erg, $M_{ej,14dt} = 0.08$–0.35 M$_\odot$ and $\kappa_{14dt}/\kappa_{11fe} = 1.5$–$11.6$. The relatively large uncertainties reflect the large errors in the estimated explosion epoch (see §3.1.4). Similarly, we obtained $\kappa_{05hk}/\kappa_{11fe} = 2.2$–$4.3$ (see Appendix C for details). Interestingly, the opacity of the SNe Iax was found to be larger than that of normal SNe Ia. Foley et al. (2013) found the ejecta mass of SNe Iax is systematically small based on the LC analysis [6]. The contribution of the iron-group elements to the opacity could differ from those in the ejecta of normal SNe Ia. This large ratio $\kappa_{Iax}/\kappa_{11fe}$ indicates that such a difference exists. However, for a more realistic treatment, one has to take into account the different physical properties (e.g., ionization) in SNe Iax and normal SNe Ia, which is beyond the scope of this study.

3.2.5 Explosion Mechanism

We discuss the explosion mechanism of SN 2014dt based on the explosion parameters derived above. Since the derived explosion parameters have a large uncertainty, the discussion here should be regarded as being qualitative. For SNe Iax, several different explosion models have been suggested (e.g., the weak deflagration model with or without a bound remnant, the pulsating delayed detonation; PDD, and the fallback CC models). For the weak deflagration model without a bound remnant (Nomoto et al. 1976; Branch et al. 2004; Jha et al. 2006; Sahu et al. 2008), our analysis suggests that this model clould not explain the slow decline LC in the late phase (see §3.2.3). As previously mentioned, the observational properties of SNe Iax are explained by the PDD model (e.g., SN 2012Z; Stritzinger et al. 2015). In the PDD model, the detonation is triggered after the deflagration phase. This creates a high-density inner ejecta, and thus it may explain the slow evolution and low velocities seen in the late time spectra of SN 2014dt.

In Table 6, we show the characteristic explosion parameters predicted by the weak deflagration model with a bound remnant (Fink et al. 2014) and by the fallback CC SN model (Moriya et al. 2010). They are apparently consistent with those derived for SN 2014dt. In the fallback CC model, some progenitor models (a He star with initial

[6] In previous paper, some authors pointed out that the ejecta mass of SNe Iax is consistent with a Chandrasekhar-mass (e.g., Sahu et al. 2008; Stritzinger et al. 2015).

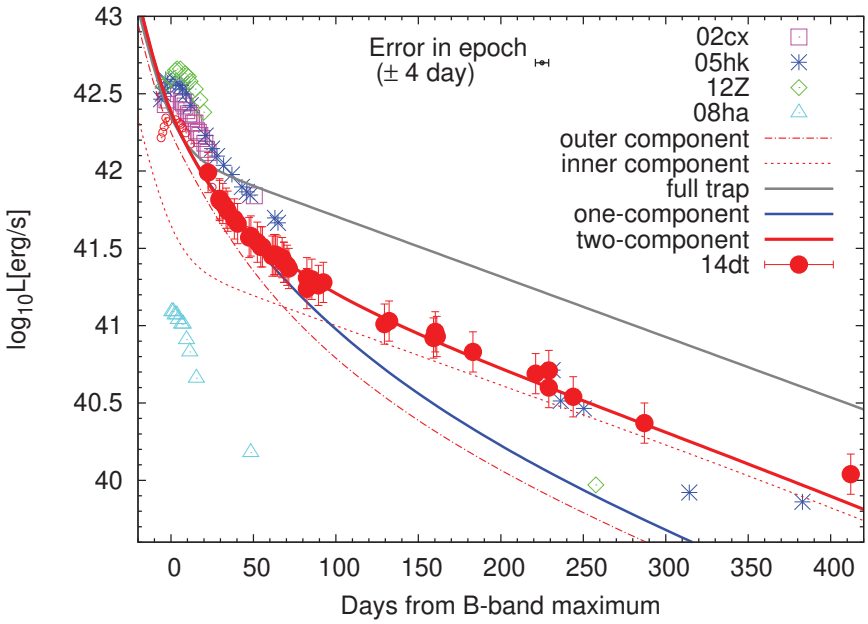

Figure 20: The bolometric light curve of SN 2014dt. This is the 'combined' bolometric LC with the template LCs taken from SN 2005hk and $\Delta t = 0$ days (see Appendix B). The red filled and open circles are the bolometric luminosities obtained from the sum of fluxes in the $BVRI$-bands and those from fitted template LCs in SN 2005hk, respectively. At 232, 287 and 412 days, we calculated the bolometric luminosity from only V- and R-band fluxes under the assumption of the non-evolving SED shape at $\gtrsim$ 100 days because we do not have B- and I-band data. For comparison, we plotted the LCs of SNe 2002cx (Li et al. 2003), 2005hk (Sahu et al. 2008), 2008ha (Foley et al. 2009) and 2012Z (Yamanaka et al. 2015). The gray, blue and red solid lines show the full-trap model, and one- and two-component LC models, respectively. In these models, the total ^{56}Ni mass is set to be $\sim$0.10 $M_\odot$. The dashed and dotted lines indicate the outer and inner components, respectively, in the two-component model.

mass of 40 $M_\odot$, CO stars with initial masses of 25 and 40 $M_\odot$) seem to explain the observations. However, Foley et al. (2015) gave the upper-limit of the brightness of the progenitor from the pre-explosion images taken by the HST and suggested that an existence of a massive star in the progenitor system is unlikely. Thus, we consider that the weak deflagration model with a bound remnant is most plausible for SN 2014dt. However, the explosion parameters of SN 2014dt have large uncertainties due to a lack of pre-maximum data. Thus, we do not argue strongly that the derived parameters provide a strong evidence of the weak deflagration model. Rather, we list this analysis as a supporting evidence to the arguments in the late phase behaviors, which led us to suggest the weak deflagration model for SNe 2014dt and 2005hk. The slow evolution in the SED of SN 2014dt in the same phase (§3.2.1) seems consistent with this model.

Our late time data revealed the nearly unchanged SED and full γ-ray trapping, which is difficult to explain by the expanding SN ejecta with decreasing density. It is thus tempting to connect these properties to the weak deflagration model, in which the bound remnant and its atmosphere may serve as a high-density "stationary" source of the energy input. If the PDD model also created a slow, high-density Fe-rich ejecta which keeps opaque for 400 days, and this could also be a viable model, while this may require fine-tuning in the model. We suggest the weak deflagration as a straightforward interpretation, but distinguishing these two models will require further study both in theory and model. Indeed, there are two possible drawbacks so far raised for the weak deflagration model. (1) The weak deflagration model by Fink et al. (2014) leads to a rapid decline in the post-maximum phase. However, the model does not include the effect of the central remnant, and thus the investigation of the effects of the bound remnant in the LC is strongly encouraged. (2) The weak deflagration model inevitably leads to a well-mixed, non-stratified structure in the ejecta, while the layered structure has been inferred at least for some SNe Iax from the velocity evolution (SN 2012Z; Stritzinger et al. 2015) and through spectral modeling (SN 2011ay; Barna et al. 2017). Indeed, this feature has been suggested to be consistent with the PDD model rather than the weak deflagration model (Stritzinger et al. 2015). To further add possible diagnostics to differentiate the two models, we encourage to investigate the evolution of line velocities in the late phase. The two scenarios may predict the difference in the formation of the low velocity permitted lines in the late phase. The weak deflagration model could produce the permitted lines both in the remnant WD and the slow expanding ejecta, while only the latter is possible in the PDD. As these two mechanism will lead to different evolution in the line velocities, a high-resolution spectroscopy in the late phase may solve this issue.

Table 6: Comparison of explosion parameters with candidate models

Model	Explosion energy (10^{50}erg)	Ejecta mass ($M_\odot$)	^{56}Ni mass ($M_\odot$)
Weak deflagration [7]	0.149–0.439	0.0843–0.195	0.0345–0.0730
Core collapse (40He) [8]	0.12–0.33	0.10–0.23	-
Core collapse (25CO) [8]	0.073–0.33	0.056–0.24	-
Core collapse (40CO) [8]	0.038–0.39	0.029–0.25	-
SN 2014dt [9]	0.07–0.42	0.08–0.35	0.04–0.10
SN 2005hk [9]	0.42–0.88	0.21–0.42	0.17 ± 0.02

[7] With a bound remnant. N1def and N3def models for Fink et al. (2014).
[8] He star with initial mass of 40 $M_\odot$, CO stars with initial masses of $25, 40$ $M_\odot$ for Moriya et al. (2010).
[9] This study. ^{56}Ni mass of SN 2005hk is referred to Sahu et al. (2008).

3.2.6 Comparison with Parameter Correlation Predicted by Model Calculation

In §3.2.3 and §3.2.5, we estimated the explosion parameters obtained from the observation for SNe 2014dt, and compared them with those predicted by some explosion models. From some observations of SNe Iax, weak correlations between the maximum magnitude and the decline rate, line velocity and rising time have been suggested (e.g., Narayan et al. 2011; Foley et al. 2013; Magee et al. 2016). We discuss whether it is possible for the correlations to explain in the weak deflagration model with a bound remnant. In Table 1 of Fink et al. (2014) and Kromer et al. (2015), they show the explosion parameters that obtained from the model calculations with various initial values. We use four parameters among them; the ejecta mass, the bound remnant mass, the ^{56}Ni mass, kinetic energy. We assume the peak luminosity from the ^{56}Ni mass,

$$L_{\rm peak} \propto M(^{56}{\rm Ni}). \tag{3.7}$$

Other parameters, e.g., the rising time (see Equations 3.1), are also important for estimating the ^{56}Ni mass. There are not many samples of SNe Iax in which these parameters are obtained precisely. We simply assume that other parameters required for estimating the ^{56}Ni mass are same those of SNe 2014dt and 2005hk, and apply the scaling laws. In the same way, we can estimate the width of LC (here, the ratio of $t_{\rm d,SNeIax}/t_{\rm d,11fe}$) and expansion velocity from Equations 3.3 and 3.4. The width of LC can be paraphrased by the decline rate. If the width of LC is broader, the decline rate is slower. Additionally, we assume that SNe experience nearly full trapping of the deposited energy in the late phase as in the case of SN 2014dt. Then, we compare the peak luminosity, the width of LC and the luminosity in the late phase (about 200–250 days) predicted from the model calculations with the observation data of SNe Iax. In Table 7, we summarize the sample of SNe Iax used for comparison. In the observations of other SNe Iax, there are no data for some bands or same filter system. If the data obtained with the other filter system (e.g., SDSS filters), we cannot estimate the bolometric luminosity using the method described in §3.2.3. The bolometric luminosity is here estimated by interpolating the SED, and integrating it. Additionally, we compared them with the bolometric luminosity of SN 2011fe, and added a constant due to there is no data for some bands. The difference by estimation method of the bolometric luminosity is small, in the case of SN 2014dt, the bolometric luminosity obtained by integration of SED is slightly brighter, about $\sim$0.05 dex at $\sim$20 days, than that of obtained by using the methods described in §3.2.3.

After ∼20 days, the difference of the estimated bolometric luminosity becomes larger, and they depend on which the data with the bands is used. The ratio of $t_{\rm d,SNeIax}/t_{\rm d,11fe}$ was determined by matching the bolometric luminosity until ∼20 days. The details are given in the Appendix C.

In Figure 21, we show the correlation between the peak bolometric luminosity and the LC width. The difference is seen between the predicted parameters using the data SN 2014dt and those of SN 2005hk due to missing the pre-maximum data of SN 2014dt. Although there is such a difference, the weak deflagration model predicts a correlation with the peak bolometric luminosity and the LC width. The data obtained from the observations are roughly consistent with the data predicted from the weak deflagration model, expect for SNe 2008ha and 2010ae. However, more samples of SNe Iax are required to discuss whether there is the correlation actually. The model of Kromer et al. (2015) (the open circles in Figure 21) was calculated to explain the observable behavior of SN 2008ha. On the other hand, in Figure 21, the data obtained from the observations of SN 2008ha are not consistent. In this thesis, we assume the diffusion timescale of SNe 2014at and 2005hk are same as that of these fainter SNe Iax such as SN 2008ha. In the model of Fink et al. (2014), the smaller explosion energy, the ratio of the mass for the iron group elements (IGE) and the ejecta mass (M_{IGE} / M_{ej}) is larger. It indicates that the opacity of the SNe is larger in the model with smaller explosion energy. For N1def model, that is with the smallest explosion energy in the calculations of Fink et al. (2014), the ratio of M_{IGE} / M_{ej} ∼ 1.8. On the other hand, in Kromer et al. (2015), the ratio of M_{IGE} / M_{ej} ∼ 0.4 and smaller opacity are expected. In the fainter SNe Iax, that the physical properties, such as the opacity of ejecta, are different from those in other SNe Iax.

In Figure 22, we show the correlation between the peak bolometric luminosity and the long-term decline rates (0 to 200–250 days) of the bolometric luminosity. The data obtained from the observations are not consistent with the data of SNe 2008ha and 2012Z. In the Figure 20, the decline rate of SN 2012Z in the late phase is fastest among those of comparison SNe Iax. The bolometric LC of SN 2012Z can be explained without the high-density material in the inner part unlike SNe 2014dt and 2005hk. It might be explained by the difference of the distribution of ^{56}Ni remaining in the inner component. There is more diversity in the late phase of SNe Iax, and the data samples of SNe Iax in the late phase are small, the larger sample of well-observed SNe Iax are needed.

Table 7: Data sets of SNe Iax and the properties

SN	L_{peak} (10^{42} erg/s)	$\Delta L_{200-250}$ (dex)	$t_{d,SNeIax}/t_{d,11fe}$	Distance (Mpc)	$E(B-V)$	Band	References
2002cx	3.2	–	0.9	104.2	0.034	$BVRI$	1
2005cc	1.1	–	0.8	37.0	0.0056	$BVRI$	2,3,4,5
2005hk	3.6	1.8	0.9–1.1	49.2	0.02	$BVRI$ $ugriz$	6,7,8
2008A	5.4	–	0.9	70.0	0.0427	$BVRI$	9
2008ge	2.5	–	1.3	16.8	0.0109	V	10
2008ha	0.1	1.6	0.5–0.8	21.3	0.075	$BVRI$ $ugri$	11,12
2010ae	0.3	–	0.5–0.6	13.1	0.62	BV gri	13
2011ay	6.0	–	0.8–0.9	86.9	0.081	$BVRI$	14
2012Z	4.5	2.7	0.9–1.1	30.2	0.036	$BVRI$ $ugri$	15,16
2014ck	3.2	–	0.9	24.4	0.48	gri	17
2014dt	1.2–1.8	1.7	1.0–1.6	14.5	0.02	$BVRI$	18
2014ek	3.2	–	0.9	99.5	0.054	$BVRI$ gri	19

(1) Li et al. (2003); (2) Ganeshalingam et al. (2010); (3) Silverman et al. (2012b); (4) Lennarz et al. (2012); (5) Foley et al. (2013); (6) Sahu et al. (2008); (7) Holtzman et al. (2008); (8) Lennarz et al. (2012); (9) Hicken et al. (2012); (10) Foley et al. (2010); (11) Foley et al. (2009); (12) Stritzinger et al. (2014); (13) Stritzinger et al. (2014); (14) Szalai et al. (2015); (15) Stritzinger et al. (2015); (16) Yamanaka et al. (2015); (17) Tomasella et al. (2016); (18) This sturdy.; (19) Li et al. (2018a)

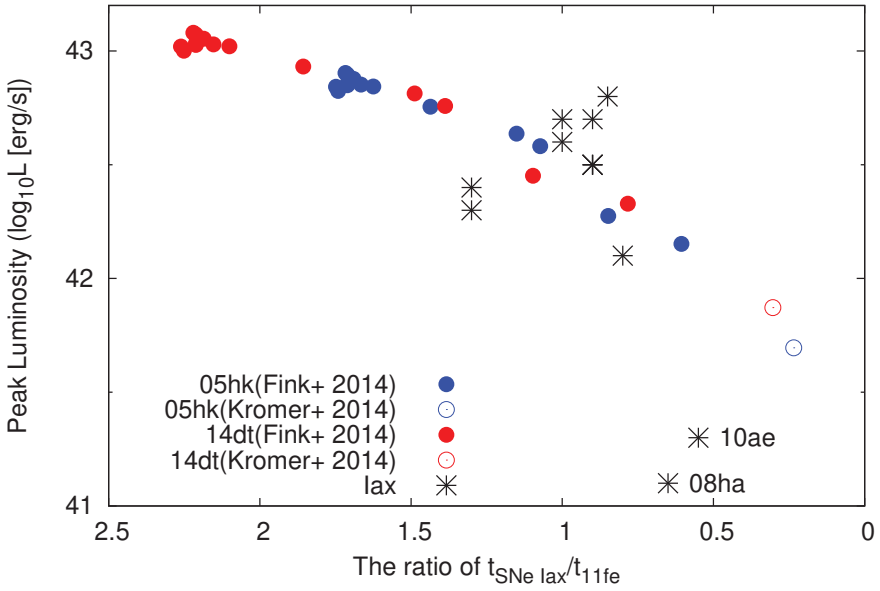

Figure 21: Correlation between the peak bolometric luminosity and the LC width; the ratio of $t_{\rm d,SNeIax}/t_{\rm d,11fe}$. The black asterisk symbols are obtained from the observations (see Table 7). The red or blue points are the parameters estimated from the weak deflagration model using scaling laws of SNe 2014dt and 2005hk, respectively. The filled and open circles are obtained from the model by Fink et al. (2014) and Kromer et al. (2015), respectively.

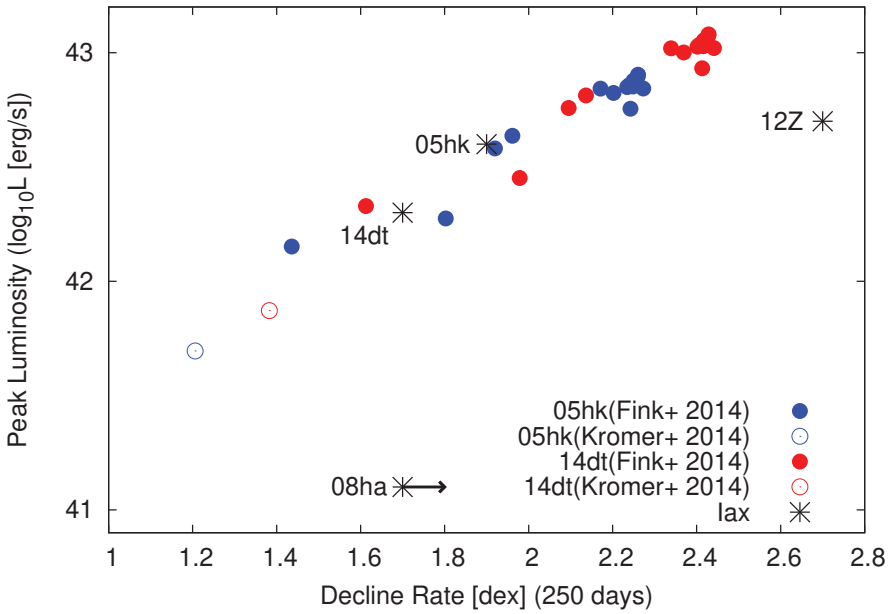

Figure 22: Correlation between the peak bolometric luminosity and the long-term decline rates (0 to 200–250 days) of the bolometric luminosity. The symbols are the same as in Figure 21.

Chapter 4

SN 2017erp: Additional Emission Component in Earliest Phase

4.1 Results

4.1.1 Light Curves

In Figure 23, we obtained the UV and optical LCs since the rising part of SN 2017erp. We compare the LCs of SN 2017erp and those of SN 2005cf in Figure 23. SN 2017erp is essentially similar to SN 2005cf.

We estimated the epoch of the B-band maximum as MJD 57935.41 (2017 July 1.4 UT) using Kanata and UVOT data by polynomial fitting at around the maximum light. In this thesis, we adopted the B-band maximum as 0 day. Additionally, we estimated the decline rate, Δm_{15}, as well as the epoch of the maximum light in each of the $V, B, U, UVW1, UVW2$ band (Table 8). After correcting the distance modulus and the total extinction (see §2.1.2), we derived the absolute maximum magnitude and Δm_{15} in the B-band; $M_{B,max} = -19.17 \pm 0.09$ mag and 1.26 ± 0.03 mag, respectively. The $M_{B,max}$ of SN 2017erp is consistent with those of SNe 2005cf ($M_{B,max} = -19.53 \pm 0.11$ mag; Wang et al. 2009) and 2011fe ($M_{B,max} = -19.21$ mag; Richmond & Smith 2012, $M_{B,max} = -19.33$ mag; Munari et al. 2013) within the error. The decline rate, Δm_{15} of SN 2017erp is slightly large or comparable to those of SNe 2005cf (1.07 ± 0.03 mag; Wang et al. 2009) and 2011fe (1.17 ± 0.04 mag; Pereira et al. 2013, 1.21 ± 0.03 mag; Richmond & Smith 2012, 1.11 mag; Munari et al. 2013). These values are slightly different from those obtained by Brown et al. (2018). These are caused by the various factors, e.g., insufficient calibration for insturment effects, the value of magnitude for comparison stars and the methods of photometry. We discuss the difference from Brown et al. (2018) in Appendix F.

Table 8: Peak magnitude and its epoch of SN 2017erp in each photometric band

Band	Maximum date (MJD)	Maximum magnitude	Δm_{15}
V	57937.4 ± 0.7	13.53 ± 0.03	0.80 ± 0.05
B	57935.4 ± 0.7	13.69 ± 0.02	1.26 ± 0.03
U	57933.7 ± 0.1	13.87 ± 0.01	1.58 ± 0.05
$UVW1$	57933.6 ± 0.3	15.18 ± 0.01	1.44 ± 0.04
$UVW2$	57934.6 ± 0.1	16.64 ± 0.01	1.38 ± 0.01

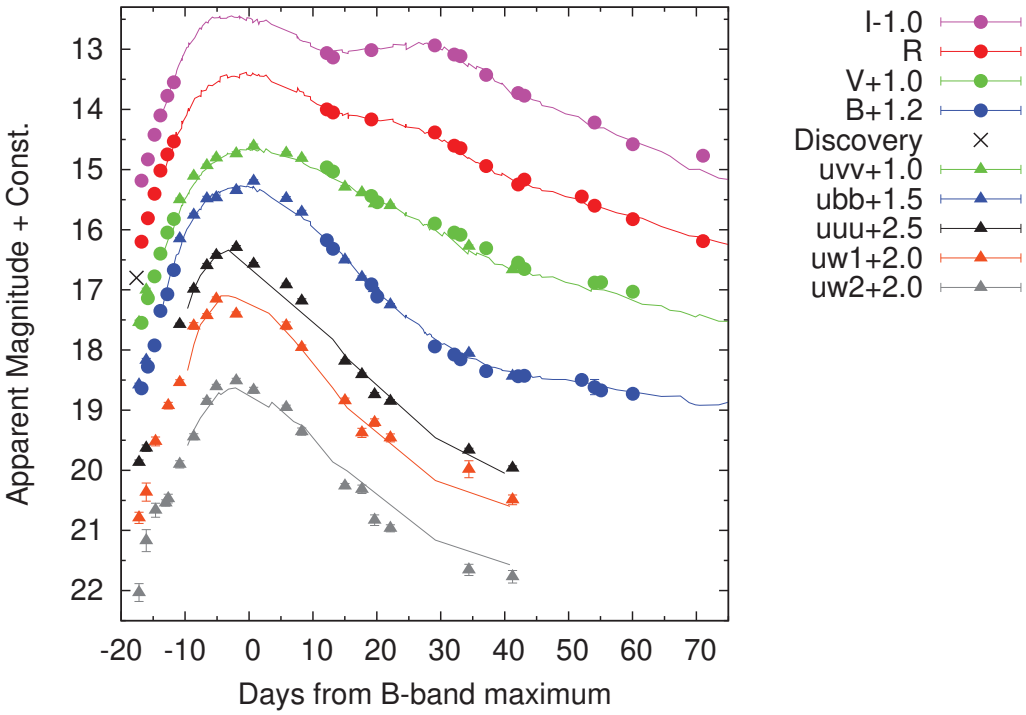

Figure 23: Multi-band light curves of SN 2017erp. The filled circles and triangles denote data that were obtained using Kanata and *Swift*, respectively. The cross symbol is the discovery magnitude in white light (Itagaki 2017) which is close to *R*-band magnitude. The light curve of each band is shifted vertically as indicated in the top-right portion outside of the panel. We adopted MJD 57935.4 ± 0.7 as 0 day. For comparison, we show the light curves of SN 2005cf with solid lines (Wang et al. 2009).

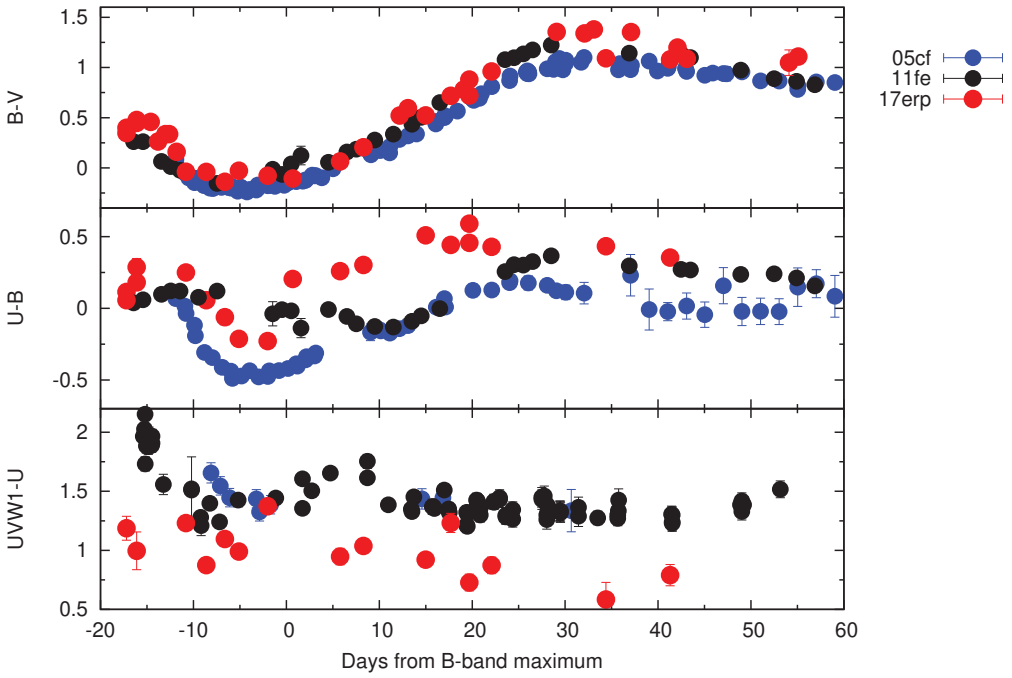

Figure 24: $B-V$, $U-B$ and $UVW1-U$ color evolutions of SN 2017erp (red symbols). We show those of normal SNe Ia 2005cf (blue symbols; Wang et al. 2009) and 2011fe (black symbols; Richmond & Smith 2012, Munari et al. 2013, Tsvetkov et al. 2013, Brown et al. 2014). The color has been corrected for the extinctions in Milky Way and the host galaxy.

4.1.2 Color Evolution

In Figure 24, we show the color evolutions of SN 2017erp. The $B-V$ evolution of SN 2017erp is similar to those of SNe 2005cf and 2011fe. On the other hand, the difference among UV colors is large. In the $U-B$ evolution, until about 20 days after the maximum light, the color evolution is different. The color of SN 2017erp is redder than those of SNe 2005cf and 2011fe after the maximum light. The $UVW1-U$ evolution is almost constant after -10 days from the maximum light. The color of SN 2017erp is bluer ($\sim$0.5 mag) in the most phases.

4.1.3 Spectral Evolution

Figure 25 shows the optical spectra of SN 2017erp from -17 days through 42 days. The spectra are characterized by absorption lines of Si II, S II, Fe II, Fe III and the Ca II IR triplet. The possible shallow C II absorption line is seen around 6300 Å in the spectrum at -17 days.

SN 2017erp is similar to SNe 2005cf and 2011fe, however, the spectra of SN 2017erp show the high velocity features at the earlier phases. In the early spectra of SN 2017erp, they show the high velocity features of Fe II, Si II and Ca II IR triplet lines. Such features are also seen in some SNe Ia (e.g., SN 1994D; Hatano et al. 1999, SN 2002cx; Li et al. 2001, SN 2001el; Wang et al. 2003, SN 2003du; Gerardy et al. 2004, SN 1999ee; Hamuy et al. 2002 and Stritzinger et al. 2002). The line velocity of Si II 6355 in SN 2017erp is $\sim$20000 km s^{-1} at -17 days, and that of Si II 6355 in SN 2011fe is $\sim$15000 km s^{-1}. After about -12 days, the velocity of SN 2017erp is almost the same with as

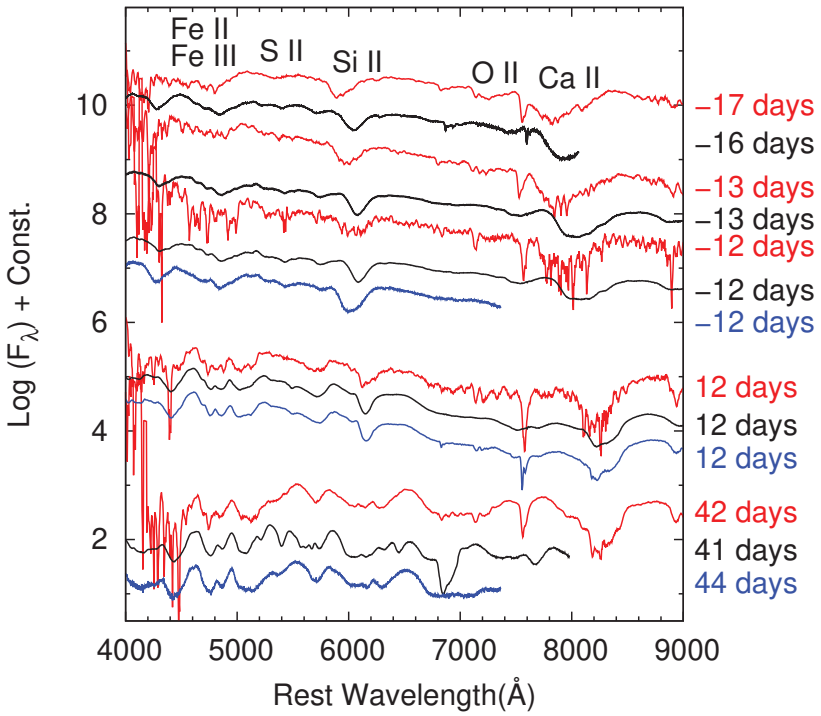

Figure 25: Spectral evolution of SN 2017erp (red solid lines). The epoch of each spectrum is indicated on the right outside of the panel. For comparison, we plotted the spectra of SN 2005cf (blue lines; Garavini et al. 2007, Wang et al. 2009, Gall et al. 2012), SN 2011fe (black lines; Pereira et al. 2013, Maguire et al. 2014, Mazzali et al. 2014).

that of SNe 2005cf and 2011fe.

4.2 Discussion

4.2.1 Estimation of the Rising Time

We successfully obtained the data of SN 2017erp from the earliest rising part. From these observation data, we can constrain the rising time (time taken from the explosion to the maximum light). Fitting a quadratic curve to the R-band LC of SN 2017erp, we estimate the rising time. The explosion date is determined as MJD 57914.91 ± 0.5 (2017 June 10.9 UT). The rising time is defined as the period from the explosion date through the maximum date of B-band. Then, the rising time of SN 2017erp is 20.5 ± 0.9 day. It is slightly longer than the rising time of SNe 2005cf (18.4 ± 0.5 day; Wang et al. 2009) and 2011fe (17.8 ± 0.1 day; Nugent et al. 2011b, Pereira et al. 2013).

In some previous studies, the relation between the rising time and the decline rate has been studied (e.g., Riess et al. 1999; Conley et al. 2006; Hayden et al. 2010; Ganeshalingam et al. 2011). Compared with Figure 6 of Ganeshalingam et al. (2011), the rising time of SN 2017erp is longest among their samples. The rising time of SN 2017erp is significantly larger than those of normal SNe Ia, rather similar to overluminous SNe (e.g., SN 1991T/SN 1999aa-like).

Branch et al. (2006) suggested a new classification methods of SNe Ia by the measurements of the pseudo equivalent width of absorption lines for Si II λ5792 and Si II λ6355 (see §1.2.3). According to it, we try to classify SN 2017erp using the spectra

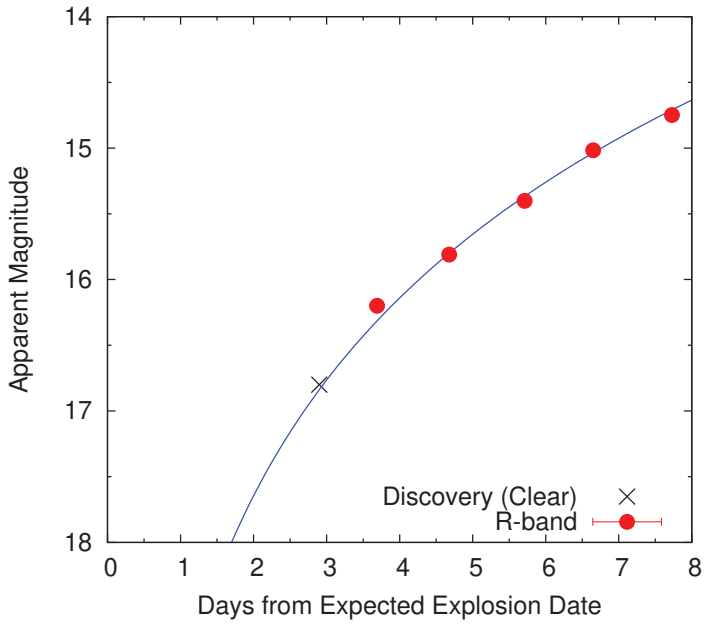

Figure 26: The R-band light curves of SN 2017erp. The cross symbol is the discovery magnitude (Itagaki 2017). The explosion date is estimated as MJD 57914.91 $\pm$ 0.5 by fitting of a quadratic function (blue solid line).

around maximum light (see the detail of the subclass in §1.2.3). Because we do not obtain the data around maximum light, we use the data obtained by Brown et al. (2018). At -1 days, the pseudo equivalent width of absorption lines for Si II λ5792 and Si II λ6355 of SN 2017erp are 22.5 $\pm$ 1.1 and 109.9 $\pm$ 1.7, respectively. In Figure 27, we show the pseudo equivalent width of Si II λ5792 lines v.s. Si II λ6355 lines. The position of SN 2017erp locates in BL subclass. Even though SN 2017erp is normal SN Ia, i.e., not belonging to overluminous subclass, it has long rising time.

4.2.2 Presence of Early Phase Emission

In this section, we discuss what the longer rising time of SN 2017erp originates from. In the previous papers, authors discuss about the early phase emission of SNe Ia (see §1.2.2), and this emission affects the rising part of the LC. In this thesis, we consider the three physical process as the possible origin of the emission component, the SN ejecta-companion interaction, the SN ejecta-CSM interaction, and ^{56}Ni distribution.

First, we consider the SN ejecta-companion interaction. If SNe Ia is caused by the SD scenario, a non-degenerate companion star such as a main sequence or red giant star, should exist. The ejecta of SN Ia collides with the companion star, and creates heat and thermal energy. The thermal energy is cooled quickly due to the adiabatic expansion. The signature will disappear in a few days from the explosion, depending on the separation of the progenitor binary. In Figures 28 and 29, we compare the interaction between the SN ejecta and the companion star model (Maeda et al. 2018). In these model LCs, the contribution of ^{56}Ni is not considered, this will affect from a few days after the explosion. We compare the observed data at earlier phase with them, the observed ones are roughly consistent with the model at smaller separation, and the separation of the binary is 5×10^{11} cm, expect for the first data point in the $UVW1 - V$ color. However, in the model at smaller separation, we should recognize that the $B - V$ color is more significantly affected by the contribution of ^{56}Ni than

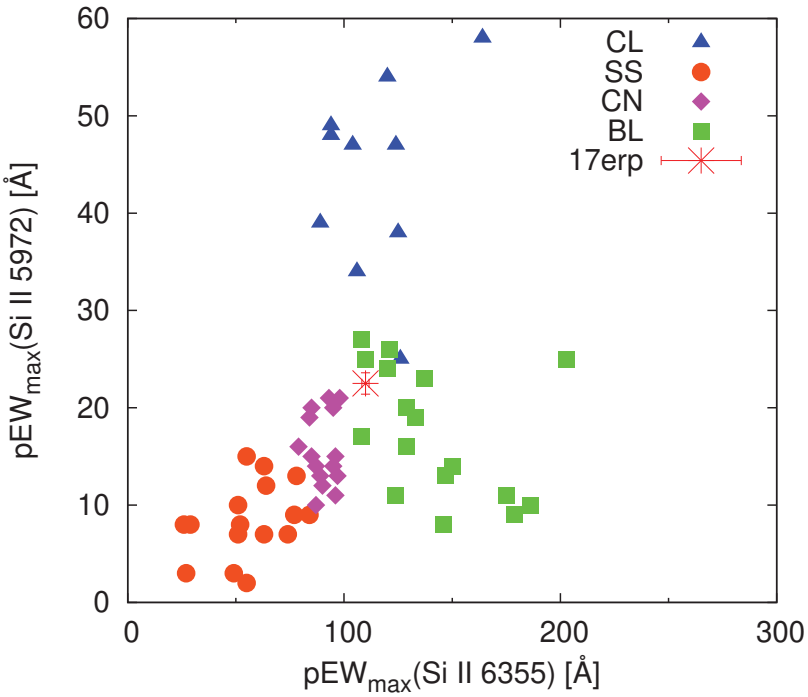

Figure 27: Pseudo equivalent width of Si II λ5792 lines v.s. Si II λ6355 lines. The diamond, square, triangle and circle symbols denote the "Core Normal (CN)", "Broad Line (BL)", "Cool (CL)", and "Shallow Silicon (SS)" subclass, respectively. The data and classification of other SNe Ia are referred to from Silverman et al. (2012a).

in the $UVW1 - V$ color (Maeda et al. 2018). It can only limit roughly the size. SN 2017erp shows bluer or constant color in the early phase, and it is considered that there is additional contribution other than ^{56}Ni. The binary has the filled Roche-lobe, and we can estimate the mass of the companion star, about 2 $M_\odot$ main sequence star in the case that the separation of the binary is 5×10^{11} cm.

Secondly, we consider the SN ejecta-CSM interaction. The emission mechanism is almost same as the model of the interaction between SN and the companion star; however, the timescale of the color evolution should be faster due to the difference of the diffusion timescale and initial internal energy. The color of SN 2017erp at earlier phase roughly agrees with that in the model of the CSM mass, 0.3 $M_\odot$, and the separations of the binary, 10^{12} cm.

Finally, we consider the contribution of ^{56}Ni. If ^{56}Ni distributes in the outer layer by the mixing, we can see the emission from the radioactive elements at the earlier phase. Piro & Morozova (2016) calculated the color evolution with various density distributions of ^{56}Ni. In Figure 8 of Piro & Morozova (2016), they compared the color evolution of SN 2011fe with the $B - V$ color evolution derived by the model. The color of SN 2017erp is slightly redder than that of SN 2011fe until -10 days (see Figure24). The model expects that SN Ia have redder color in the earlier phase, and that ^{56}Ni is not expected to be distributed in outer layer. It is difficult to explain the distribution of ^{56}Ni using the model results by by Piro & Morozova (2016).

Therefore, SN 2017erp might be affected by the interaction between SN ejecta and the companion star or CSM in the early phase. However, we can not distinguish either. The redder color in the early phase is also explained by the model, depending on the explosion mechanism (e.g., helium detonation model). To constrain them, it needs the

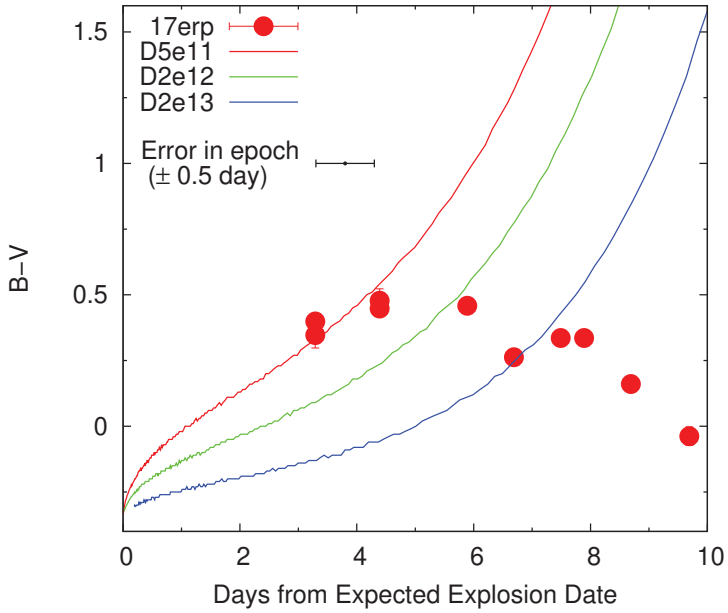

Figure 28: Comparison of the $B-V$ color evolution of SN 2017erp with the $B-V$ evolution expected by the SN ejecta-companion interaction. The red, green and blue solid lines denote the models at different separations, 5×10^{11}, 2×10^{11} and 2×10^{13} cm, respectively (Maeda et al. 2018). In these models, the contribution of ^{56}Ni is not considered.

dense observation from the earlier phase. Additionally, Brown et al. (2018) suggested that SN 2017erp has the different metallicity from that of SN 2011fe. It is not sure how much the heavy elements, such as Fe II, and affect the color evolution. We need to obtain a larger sample of well-observed in UV bands in the future.

Stritzinger et al. (2018) examined the early phase intrinsic $B-V$ color using the data of SNe Ia discovered within 3 days from the explosion. The $B-V$ color within 5 days from explosion is divided in two populations; the blue events or the red events at early time. The blue events are classified as SN 1991T/SN 1999aa-like, SS subclass. On the other hand, the red events are classified mostly as CN or CL subclass. In Figure 30, we show the early phase $B-V$ color, although the colors are scaled to match at the maximum light. SN 2017erp has red in the $B-V$ color in the early phase, it is consistent with the suggestion of Stritzinger et al. (2018).

For these samples, we examined the $UVW1-V$ color in the early phase. The SNe belonging to the blue events in the $B-V$ color are bluer in the early phase, also in the $UVW1-V$ color. However, SN 2017erp is bluer in the early phase, it is similar to the blue events. The early phase emission of SN 2017erp might be prominent in UV bands. However, the samples obtained the $UVW1-V$ color in the early phase are limited, and the additional data samples will be required further.

[10]http://swift.gsfc.nasa.gov/docs/swift/sne/swift_sn.html. The reduction is based on that of Brown et al. (2009), including subtraction of the host galaxy count rates and uses the revised UV zeropoints and time-dependent sensitivity from Breeveld et al. (2011).

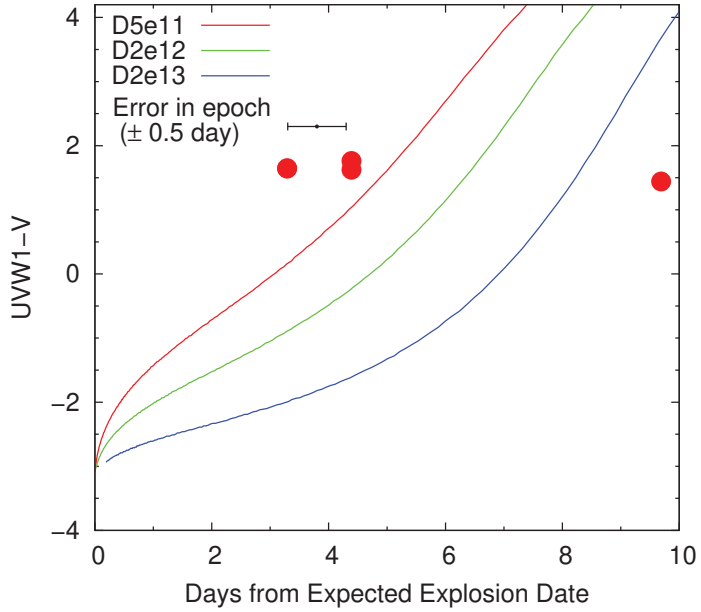

Figure 29: Comparison of the $UVW1-V$ color evolution of SN 2017erp with the $B-V$ evolution expected by the SN ejecta-companion interaction. The lines are plotted in the same manner as in Figure 28.

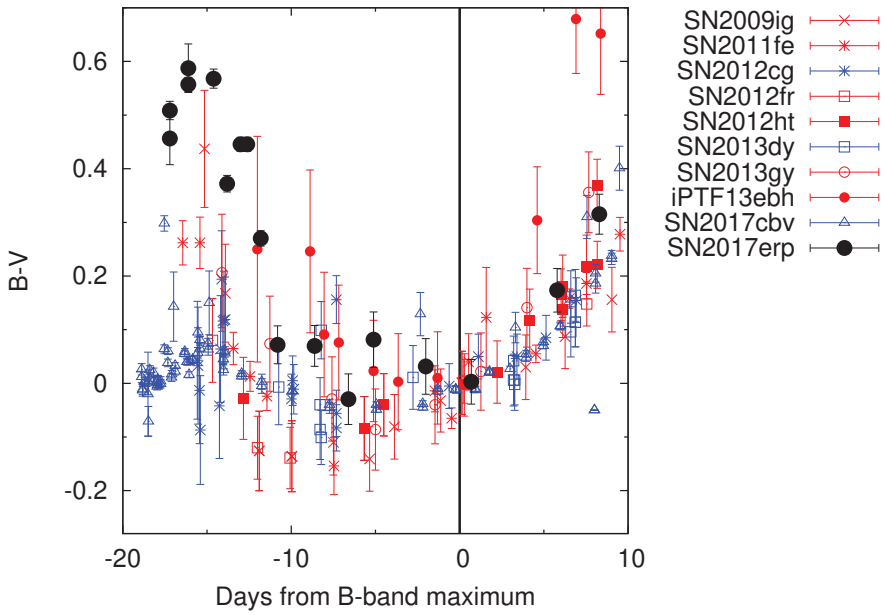

Figure 30: The early phase $B-V$ color evolution of SN 2017erp (black circles). For comparison, we plotted the data of SNe 2009ig, 20011fe, 2012cg, 2012fr, 2012ht, 2013dy, 2013gy, 2017cbv, iPTF13ebh. The data of the comparison SNe Ia are downloaded from the Swift's Optical/Ultraviolet Supernova Archive[10] (SOUSA; Brown et al. 2014). The color scales to 0 as the color at the maximum light. The red or blue symbols denote to the red events and blue events, respectively, as classified by Stritzinger et al. (2018).

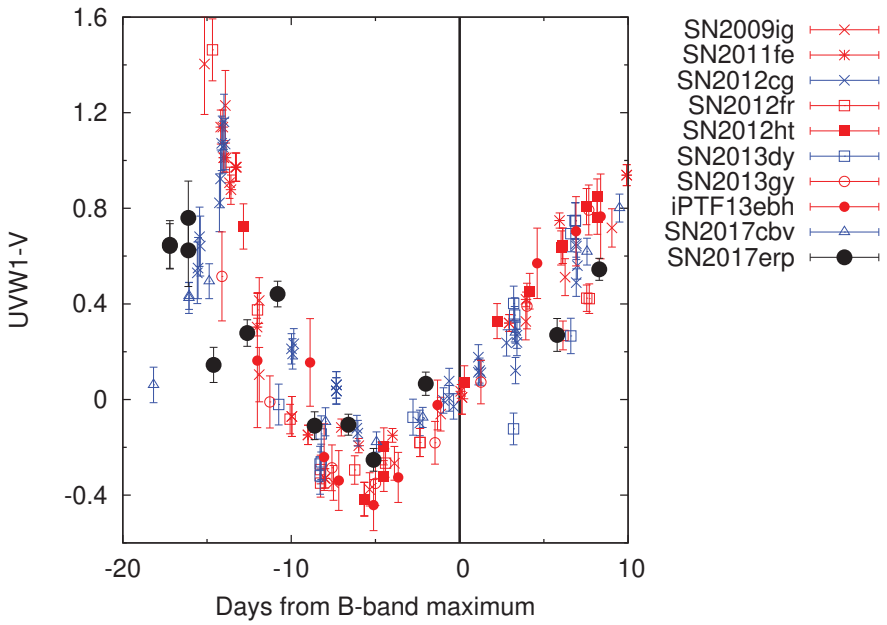

Figure 31: The early phase $UVW1 - V$ color evolution of SN 2017erp. We plot it in the same manner as in Figure 30.

Chapter 5

Conclusions

We presented long-term optical and NIR observations of SN 2014dt up to 410 days after the maximum light. The data for SNe Iax in the NIR bands are rare, especially in the late phase. We successfully obtained the NIR data for SN 2014dt through the late phase. The LC showed a considerably slow decline in the late phase; the decline rate was the smallest among well-studied SNe Iax samples. From the evolution of the SED, SN 2014dt did not show significant change in the BB temperature after 180 days. The evolution of the spectral features was also slow in SN 2014dt in the late phase. A bound remnant left after the explosion gives a good account of these observational properties. By scaling the explosion parameters of normal SN Ia 2011fe, we suggest that the mass of synthesized ^{56}Ni was 0.04–0.10 $M_\odot$, the kinetic energy was (0.07–0.42) $\times 10^{50}$ erg, and the ejecta mass was $M_{\rm ej} = 0.08$–0.35 $M_\odot$. These values are consistent with the prediction of the weak deflagration model with a bound remnant. However, the uncertainties in the derived explosion parameters for SN 2014dt were large, reflecting our conservative error estimation associated with a possible range of the missed the pre-maximum LCs. The overall properties derived from the long-term observations of SN 2014dt could be explained with the weak deflagration model which leaves a bound remnant after the explosion. Indeed, by applying the same model to SN 2005hk, we found that SN 2005hk could also be explained by the weak deflagration model with an explosion energy larger than for SN 2014dt. With the larger kinetic energy, the model does not leave a bound remnant. The present work demonstrates the significance and importance of late phase observations to uncover the origin of SNe Iax. To further test of the explosion models, we need to obtain a larger sample of well-observed SNe Iax in the future.

Next, we presented UV and optical observations of SN 2017erp from a few days after the explosion. The properties of LC (the absolute maximum magnitude, $M_{B,max} = -19.17 \pm 0.09$ mag and Δm_{15} in the B-band, 1.26 ± 0.03 mag) and spectra for SN 2017erp are consistent with those of normal SNe Ia except that it has a long rising time (20.5 ± 0.9 day in the R-band). It suggests that an additional emission component exists only during the pre-maximum phase. We compare the color evolution of SN 2017erp with that predicted from the model to find out the causes of the early phase emission. It is expected that the early phase emission caused by ^{56}Ni spreading out to the outside turn into bluer color. The color of SN 2017erp was redder throughout the early phase, suggesting that the early phase emission is caused by not ^{56}Ni but other energy source. From the comparison with the model, we can explain it with the interaction between the SN ejecta and the companion star or CSM; however, we cannot distinguish which is more plausible. There is significant difference between the color of SN 2017erp and that expected by these model. In the models for comparison, the radiation from ^{56}Ni was not considered and easily affected by model parameters. We need to investigate other observational features, e.g., the high dispersion spectroscopy around maximum

light; it will be a clue to constrain the progenitor system. Again, it needs to find out the physical parameters at an earlier phase.

In summary, the observational features of SN 2014dt are consistent with the model expected by SD scenario. The color evolution in the early phase for SN 2017erp is consistent with the SN ejecta-companion interaction, and it supports the SD scenario, also. On the other hand, the color evolution is explained by the SN ejecta-CSM interaction. In the SD scenario, it is likely that there is a (dense) CSM produced by the mass loss in the companion star. Thus, these observational material in SNe 2014dt and 2017erp, which are both not very normal SNe Ia, is likely explained by the SD scenario, although we cannot reject the DD scenario completely.

Acknowledgements

I would particularly like to thank Koji S. Kawabata. Many advices and comments given by him has been a great help. Without them help this thesis would not have been possible.

I am deeply grateful to Masayuki Yamanaka. He gave me helpful comments and advice for this thesis. I would like to express my gratitude to Ken'ichi Nomoto and Keiichi Maeda, Masaomi Tanaka. They give insightful comments and suggestions. I thank K. Aoki and members of observation team at Kanata and OKU for their helps with the observations. I have had the support and encouragement of Yousuke Utsumi.

References

Akitaya, H., Moritani, Y., Ui, T., et al. 2014, in Proc. SPIE, Vol. 9147, Ground-based and Airborne Instrumentation for Astronomy V, 91474O

Altavilla, G., Fiorentino, G., Marconi, M., et al. 2004, MNRAS, 349, 1344

Anupama, G. C., Sahu, D. K., & Jose, J. 2005, A&A, 429, 667

Arnett, W. D. 1969a, Ap&SS, 5, 180

—. 1969b, ApJ, 157, 1369

—. 1982, ApJ, 253, 785

Barna, B., Szalai, T., Kromer, M., et al. 2017, MNRAS, 471, 4865

Benetti, S., Cappellaro, E., Mazzali, P. A., et al. 2005, ApJ, 623, 1011

Bertin, E., & Arnouts, S. 1996, A&AS, 117, 393

Blinnikov, S. I., Röpke, F. K., Sorokina, E. I., et al. 2006, A&A, 453, 229

Blondin, S., Prieto, J. L., Patat, F., et al. 2009, ApJ, 693, 207

Blondin, S., Matheson, T., Kirshner, R. P., et al. 2012, AJ, 143, 126

Bloom, J. S., Kasen, D., Shen, K. J., et al. 2012, ApJ, 744, L17

Bose, S., & Kumar, B. 2014, ApJ, 782, 98

Branch, D., Baron, E., Thomas, R. C., et al. 2004, PASP, 116, 903

Branch, D., Dang, L. C., Hall, N., et al. 2006, PASP, 118, 560

Breeveld, A. A., Landsman, W., Holland, S. T., et al. 2011, in American Institute of Physics Conference Series, Vol. 1358, American Institute of Physics Conference Series, ed. J. E. McEnery, J. L. Racusin, & N. Gehrels, 373–376

Brown, P. J., Breeveld, A. A., Holland, S., Kuin, P., & Pritchard, T. 2014, Ap&SS, 354, 89

Brown, P. J., Holland, S. T., Immler, S., et al. 2009, AJ, 137, 4517

Brown, P. J., Hosseinzadeh, G., Jha, S. W., et al. 2018, ArXiv e-prints, arXiv:1808.04729

Childress, M. J., Hillier, D. J., Seitenzahl, I., et al. 2015, MNRAS, 454, 3816

Colgate, S. A., & McKee, C. 1969, ApJ, 157, 623

Conley, A., Howell, D. A., Howes, A., et al. 2006, AJ, 132, 1707

de Vaucouleurs, G., Peters, W. L., Bottinelli, L., Gouguenheim, L., & Paturel, G. 1981, ApJ, 248, 408

Dessart, L., & Hillier, D. J. 2005, A&A, 439, 671

Filippenko, A. V. 1997, ARA&A, 35, 309

Filippenko, A. V., Richmond, M. W., Matheson, T., et al. 1992a, ApJ, 384, L15

Filippenko, A. V., Richmond, M. W., Branch, D., et al. 1992b, AJ, 104, 1543

Fink, M., Kromer, M., Seitenzahl, I. R., et al. 2014, MNRAS, 438, 1762

Foley, R. J., Jha, S. W., Pan, Y.-C., et al. 2016, MNRAS, 461, 433

Foley, R. J., McCully, C., Jha, S. W., et al. 2014, ApJ, 792, 29

Foley, R. J., Van Dyk, S. D., Jha, S. W., et al. 2015, ApJ, 798, L37

Foley, R. J., Chornock, R., Filippenko, A. V., et al. 2009, AJ, 138, 376

Foley, R. J., Rest, A., Stritzinger, M., et al. 2010, AJ, 140, 1321

Foley, R. J., Challis, P. J., Chornock, R., et al. 2013, ApJ, 767, 57

Fox, O. D., Johansson, J., Kasliwal, M., et al. 2016, ApJ, 816, L13

Friedman, A. S., Wood-Vasey, W. M., Marion, G. H., et al. 2015, ApJS, 220, 9

Gall, E. E. E., Taubenberger, S., Kromer, M., et al. 2012, MNRAS, 427, 994

Ganeshalingam, M., Li, W., & Filippenko, A. V. 2011, MNRAS, 416, 2607

Ganeshalingam, M., Li, W., Filippenko, A. V., et al. 2010, ApJS, 190, 418

Garavini, G., Folatelli, G., Goobar, A., et al. 2004, AJ, 128, 387

Garavini, G., Nobili, S., Taubenberger, S., et al. 2007, A&A, 471, 527

Gerardy, C. L., Höflich, P., Fesen, R. A., et al. 2004, ApJ, 607, 391

Graham, M. L., Foley, R. J., Zheng, W., et al. 2015, MNRAS, 446, 2073

Hachisu, I., Kato, M., & Nomoto, K. 1999, ApJ, 522, 487

Hamuy, M., Maza, J., Pinto, P. A., et al. 2002, AJ, 124, 417

Hatano, K., Branch, D., Fisher, A., Baron, E., & Filippenko, A. V. 1999, ApJ, 525, 881

Hayden, B. T., Garnavich, P. M., Kessler, R., et al. 2010, ApJ, 712, 350

Henden, A. A., Templeton, M., Terrell, D., et al. 2016, VizieR Online Data Catalog, 2336

Hicken, M., Challis, P., Jha, S., et al. 2009, ApJ, 700, 331

Hicken, M., Challis, P., Kirshner, R. P., et al. 2012, ApJS, 200, 12

Hillebrandt, W., & Niemeyer, J. C. 2000, ARA&A, 38, 191

Hoeflich, P., & Khokhlov, A. 1996, ApJ, 457, 500

Hoeflich, P., Khokhlov, A. M., & Wheeler, J. C. 1995, ApJ, 444, 831

Holtzman, J. A., Marriner, J., Kessler, R., et al. 2008, AJ, 136, 2306

Iben, Jr., I., & Tutukov, A. V. 1984, ApJ, 284, 719

Itagaki, K. 2017, Transient Name Server Discovery Report, 647

Jha, S., Branch, D., Chornock, R., et al. 2006, AJ, 132, 189

Jha, S. W., Camacho, Y., Dettman, K., et al. 2017, The Astronomer's Telegram, 10490

Jordan, IV, G. C., Perets, H. B., Fisher, R. T., & van Rossum, D. R. 2012, ApJ, 761, L23

Junde, H., Dailing, H., Chunmei, Z., et al. 1987, Nucl. Data Sheets; (United States), 51, doi:10.1016/S0090-3752(87)80018-2

Kasen, D. 2006, ApJ, 649, 939

—. 2010, ApJ, 708, 1025

Kashikawa, N., Aoki, K., Asai, R., et al. 2002, PASJ, 54, 819

Kawabata, K. S., Nagae, O., Chiyonobu, S., et al. 2008, in Proc. SPIE, Vol. 7014, Ground-based and Airborne Instrumentation for Astronomy II, 70144L

Kawabata, K. S., Akitaya, H., Yamanaka, M., et al. 2014, ApJ, 795, L4

Kelly, P. L., Fox, O. D., Filippenko, A. V., et al. 2014, ApJ, 790, 3

Khokhlov, A. M. 1991, A&A, 245, 114

Kirshner, R. P., & Kwan, J. 1974, ApJ, 193, 27

Krisciunas, K., Hastings, N. C., Loomis, K., et al. 2000, ApJ, 539, 658

Krisciunas, K., Suntzeff, N. B., Candia, P., et al. 2003, AJ, 125, 166

Krisciunas, K., Contreras, C., Burns, C. R., et al. 2017, AJ, 154, 211

Kromer, M., Fink, M., Stanishev, V., et al. 2013, MNRAS, 429, 2287

Kromer, M., Ohlmann, S. T., Pakmor, R., et al. 2015, MNRAS, 450, 3045

Kutsuna, M., & Shigeyama, T. 2015, PASJ, 67, 54

Landolt, A. U. 1992, AJ, 104, 340

Leibundgut, B., Kirshner, R. P., Phillips, M. M., et al. 1993, AJ, 105, 301

Leloudas, G., Stritzinger, M. D., Sollerman, J., et al. 2009, A&A, 505, 265

Lennarz, D., Altmann, D., & Wiebusch, C. 2012, A&A, 538, A120

Li, H., & McCray, R. 1993, ApJ, 405, 730

Li, L., Wang, X., Zhang, J., et al. 2018a, MNRAS, 478, 4575

Li, W., Filippenko, A. V., Gates, E., et al. 2001, PASP, 113, 1178

Li, W., Filippenko, A. V., Chornock, R., et al. 2003, PASP, 115, 453

Li, W., Bloom, J. S., Podsiadlowski, P., et al. 2011, Nature, 480, 348

Li, W., Wang, X., Vinkó, J., et al. 2018b, arXiv e-prints, arXiv:1811.10056

Lira, P., Suntzeff, N. B., Phillips, M. M., et al. 1998, AJ, 115, 234

Maeda, K., Jiang, J.-a., Shigeyama, T., & Doi, M. 2018, ApJ, 861, 78

Maeda, K., Mazzali, P. A., Deng, J., et al. 2003, ApJ, 593, 931

Maeda, K., Benetti, S., Stritzinger, M., et al. 2010, Nature, 466, 82

Magee, M. R., Kotak, R., Sim, S. A., et al. 2016, A&A, 589, A89

Maguire, K., Sullivan, M., Pan, Y.-C., et al. 2014, MNRAS, 444, 3258

Maoz, D., & Mannucci, F. 2008, MNRAS, 388, 421

Marion, G. H., Brown, P. J., Vinkó, J., et al. 2016, ApJ, 820, 92

Mazzali, P. A., Sullivan, M., Hachinger, S., et al. 2014, MNRAS, 439, 1959

McClelland, C. M., Garnavich, P. M., Galbany, L., et al. 2010, ApJ, 720, 704

McCully, C., Jha, S. W., Foley, R. J., et al. 2014a, Nature, 512, 54

—. 2014b, ApJ, 786, 134

Moriya, T., Tominaga, N., Tanaka, M., et al. 2010, ApJ, 719, 1445

Munari, U., Henden, A., Belligoli, R., et al. 2013, New A, 20, 30

Nagao, T., Maeda, K., & Yamanaka, M. 2017, ApJ, 835, 143

Nakano, S., Itagaki, K., Guido, E., et al. 2014, Central Bureau Electronic Telegrams, 4011

Narayan, G., Foley, R. J., Berger, E., et al. 2011, ApJ, 731, L11

Nelemans, G., Voss, R., Roelofs, G., & Bassa, C. 2008, MNRAS, 388, 487

Nomoto, K. 1982, ApJ, 253, 798

Nomoto, K., Sugimoto, D., & Neo, S. 1976, Ap&SS, 39, L37

Nomoto, K., Thielemann, F.-K., & Yokoi, K. 1984, ApJ, 286, 644

Nugent, P. E., Howell, D. A., Bishop, D., et al. 2011a, Central Bureau Electronic Telegrams, 2792

Nugent, P. E., Sullivan, M., Cenko, S. B., et al. 2011b, Nature, 480, 344

Ochner, P., Tomasella, L., Benetti, S., et al. 2014, Central Bureau Electronic Telegrams, 4011

Pakmor, R., Kromer, M., Röpke, F. K., et al. 2010, Nature, 463, 61

Pakmor, R., Kromer, M., Taubenberger, S., et al. 2012, ApJ, 747, L10

Parrent, J. T., Howell, D. A., Friesen, B., et al. 2012, ApJ, 752, L26

Pastorello, A., Mazzali, P. A., Pignata, G., et al. 2007, MNRAS, 377, 1531

Patat, F., Benetti, S., Justham, S., et al. 2007, A&A, 474, 931

Pereira, R., Thomas, R. C., Aldering, G., et al. 2013, A&A, 554, A27

Perlmutter, S., Aldering, G., Goldhaber, G., et al. 1999, ApJ, 517, 565

Phillips, M. M. 1993, ApJ, 413, L105

Phillips, M. M., Li, W., Frieman, J. A., et al. 2007, PASP, 119, 360

Pignata, G., Patat, F., Benetti, S., et al. 2004, MNRAS, 355, 178

Pignata, G., Benetti, S., Mazzali, P. A., et al. 2008, MNRAS, 388, 971

Piro, A. L., & Morozova, V. S. 2016, ApJ, 826, 96

Raskin, C., & Kasen, D. 2013, ApJ, 772, 1

Richmond, M. W., & Smith, H. A. 2012, Journal of the American Association of Variable Star Observers (JAAVSO), 40, 872

Riess, A. G., Press, W. H., & Kirshner, R. P. 1996, ApJ, 473, 88

Riess, A. G., Filippenko, A. V., Challis, P., et al. 1998, AJ, 116, 1009

Riess, A. G., Filippenko, A. V., Li, W., et al. 1999, AJ, 118, 2675

Rodgers, C. T., Canterna, R., Smith, J. A., Pierce, M. J., & Tucker, D. L. 2006, AJ, 132, 989

Sahu, D. K., Tanaka, M., Anupama, G. C., et al. 2008, ApJ, 680, 580

Saio, H., & Nomoto, K. 1985, A&A, 150, L21

Sandage, A., Saha, A., Tammann, G. A., et al. 1996, ApJ, 460, L15

Schlafly, E. F., & Finkbeiner, D. P. 2011, ApJ, 737, 103

Schmidt, B. P., Kirshner, R. P., & Eastman, R. G. 1992, ApJ, 395, 366

Shen, K. J., Bildsten, L., Kasen, D., & Quataert, E. 2012, ApJ, 748, 35

Silverman, J. M., Kong, J. J., & Filippenko, A. V. 2012a, MNRAS, 425, 1819

Silverman, J. M., Foley, R. J., Filippenko, A. V., et al. 2012b, MNRAS, 425, 1789

Simon, J. D., Gal-Yam, A., Gnat, O., et al. 2009, ApJ, 702, 1157

Singh, M., Misra, K., Sahu, D. K., et al. 2018, MNRAS, 474, 2551

Skrutskie, M. F., Cutri, R. M., Stiening, R., et al. 2006, AJ, 131, 1163

Smith, J. A., Tucker, D. L., Allam, S. S., & Jorgensen, A. M. 2002, in Bulletin of the American Astronomical Society, Vol. 34, American Astronomical Society Meeting Abstracts, 1272

Stritzinger, M., & Leibundgut, B. 2005, A&A, 431, 423

Stritzinger, M., & Sollerman, J. 2007, A&A, 470, L1

Stritzinger, M., Hamuy, M., Suntzeff, N. B., et al. 2002, AJ, 124, 2100

Stritzinger, M. D., Hsiao, E., Valenti, S., et al. 2014, A&A, 561, A146

Stritzinger, M. D., Valenti, S., Hoeflich, P., et al. 2015, A&A, 573, A2

Stritzinger, M. D., Shappee, B. J., Piro, A. L., et al. 2018, ApJ, 864, L35

Suntzeff, N. B., Phillips, M. M., Covarrubias, R., et al. 1999, AJ, 117, 1175

Szalai, T., Vinkó, J., Sárneczky, K., et al. 2015, MNRAS, 453, 2103

Tanikawa, A., Nakasato, N., Sato, Y., et al. 2015, ApJ, 807, 40

Taubenberger, S. 2017, The Extremes of Thermonuclear Supernovae, ed. A. W. Alsabti & P. Murdin, 317

Thomas, R. C., Nugent, P. E., & Meza, J. C. 2011, PASP, 123, 237

Tomasella, L., Cappellaro, E., Benetti, S., et al. 2016, MNRAS, 459, 1018

Truran, J. W., Arnett, W. D., & Cameron, A. G. W. 1967, Canadian Journal of Physics, 45, 2315

Tsvetkov, D. Y., Shugarov, S. Y., Volkov, I. M., et al. 2013, Contributions of the Astronomical Observatory Skalnate Pleso, 43, 94

Turatto, M., Benetti, S., Cappellaro, E., et al. 1996, MNRAS, 283, 1

Valenti, S., Pastorello, A., Cappellaro, E., et al. 2009, Nature, 459, 674

van Dokkum, P. G. 2001, PASP, 113, 1420

van Dokkum, P. G., Bloom, J., & Tewes, M. 2012, L.A.Cosmic: Laplacian Cosmic Ray Identification, Astrophysics Source Code Library, ascl:1207.005

Wang, L., Baade, D., Höflich, P., et al. 2003, ApJ, 591, 1110

Wang, X., Li, W., Filippenko, A. V., et al. 2009, ApJ, 697, 380

Webbink, R. F. 1984, ApJ, 277, 355

Whelan, J., & Iben, Jr., I. 1973, ApJ, 186, 1007

Willick, J. A., Courteau, S., Faber, S. M., et al. 1997, The Astrophysical Journal Supplement Series, 109, 333

Yamanaka, M., Maeda, K., Kawabata, K. S., et al. 2015, ApJ, 806, 191

Yamanaka, M., Maeda, K., Tanaka, M., et al. 2016, PASJ, 68, 68

Zhang, J.-J., Wang, X.-F., Bai, J.-M., et al. 2014, AJ, 148, 1

Zhang, K., Wang, X., Zhang, J., et al. 2016, ApJ, 820, 67

Appendix A

Observation Log of SN 2014dt

Table 9: Log of optical photometry of SN 2014dt

MJD	Phase[11]	B (mag)	V (mag)	R (mag)	I (mag)	Site[12]
56964.85	14.4	–	–	13.43 ± 0.03	13.31 ± 0.02	OKU
56965.84	15.4	–	–	13.51 ± 0.04	13.37 ± 0.01	OKU
56966.83	16.4	–	–	13.654 ± 0.051	13.313 ± 0.050	Kanata
56967.86	17.5	–	14.349 ± 0.054	13.743 ± 0.055	13.312 ± 0.051	Kanata
56971.84	22.4	16.113 ± 0.050	14.522 ± 0.050	13.965 ± 0.051	13.580 ± 0.051	Kanata
56971.85	22.4	–	14.65 ± 0.07	13.97 ± 0.04	13.63 ± 0.04	OKU
56974.84	24.4	–	–	14.165 ± 0.050	13.894 ± 0.120	Kanata
56977.83	27.4	–	14.95 ± 0.03	14.23 ± 0.05	13.81 ± 0.03	OKU
56978.86	28.5	–	–	14.34 ± 0.03	14.03 ± 0.02	OKU
56979.85	29.4	16.54 ± 0.04	14.98 ± 0.02	14.35 ± 0.03	14.02 ± 0.02	OKU
56979.85	29.4	16.594 ± 0.054	15.125 ± 0.051	14.380 ± 0.050	13.964 ± 0.050	Kanata
56980.84	30.4	–	15.02 ± 0.08	–	–	OKU
56981.84	31.4	16.68 ± 0.06	15.02 ± 0.03	14.42 ± 0.03	14.12 ± 0.02	OKU
56983.84	33.4	16.846 ± 0.050	–	–	–	Kanata
56983.85	33.4	16.68 ± 0.07	15.11 ± 0.01	14.54 ± 0.03	14.11 ± 0.10	OKU
56984.83	34.4	16.82 ± 0.08	15.14 ± 0.03	14.54 ± 0.03	14.23 ± 0.02	OKU
56988.84	38.4	16.77 ± 0.06	15.25 ± 0.03	14.70 ± 0.03	14.37 ± 0.02	OKU
56990.85	40.4	16.73 ± 0.06	15.33 ± 0.02	14.78 ± 0.03	14.48 ± 0.05	OKU
56990.87	40.5	16.848 ± 0.050	–	–	–	Kanata
56996.86	46.5	16.80 ± 0.03	15.44 ± 0.02	14.94 ± 0.05	–	OKU
56997.80	47.4	17.10 ± 0.05	15.48 ± 0.03	15.03 ± 0.03	14.72 ± 0.02	OKU
56998.86	48.5	16.87 ± 0.06	15.49 ± 0.01	15.03 ± 0.03	14.72 ± 0.02	OKU
56998.86	48.5	17.020 ± 0.054	–	–	–	Kanata
56999.84	49.4	16.90 ± 0.04	15.49 ± 0.03	–	–	OKU
57002.80	52.4	17.08 ± 0.08	15.58 ± 0.06	15.13 ± 0.03	14.81 ± 0.01	OKU
57004.81	54.4	16.98 ± 0.04	15.60 ± 0.02	15.17 ± 0.03	15.05 ± 0.31	OKU
57005.86	55.5	17.09 ± 0.04	15.63 ± 0.02	15.19 ± 0.03	14.89 ± 0.02	OKU
57011.86	61.5	17.068 ± 0.050	15.931 ± 0.052	15.425 ± 0.051	14.880 ± 0.051	Kanata
57012.80	62.4	17.00 ± 0.08	15.81 ± 0.05	15.38 ± 0.04	15.06 ± 0.01	OKU
57013.85	63.4	17.22 ± 0.21	15.67 ± 0.22	15.40 ± 0.03	15.01 ± 0.10	OKU
57014.83	64.4	17.01 ± 0.03	15.79 ± 0.02	15.41 ± 0.04	15.10 ± 0.02	OKU
57015.87	65.5	17.15 ± 0.11	15.86 ± 0.05	15.48 ± 0.06	–	OKU
57017.78	67.4	16.98 ± 0.03	15.87 ± 0.02	15.47 ± 0.04	15.05 ± 0.08	OKU
57017.87	68.4	17.099 ± 0.050	16.078 ± 0.051	15.541 ± 0.051	14.984 ± 0.050	Kanata

Table 9: Log of optical photometry of SN 2014dt

MJD	Phase[11]	B (mag)	V (mag)	R (mag)	I (mag)	Site[12]
57018.80	68.4	17.18 ± 0.03	15.84 ± 0.03	15.48 ± 0.03	15.20 ± 0.01	OKU
57020.80	70.4	17.18 ± 0.06	15.93 ± 0.01	15.56 ± 0.03	15.26 ± 0.01	OKU
57021.83	71.4	17.24 ± 0.04	15.96 ± 0.02	15.59 ± 0.03	15.29 ± 0.02	OKU
57024.86	74.4	17.27 ± 0.15	–	–	–	OKU
57025.80	75.4	17.11 ± 0.15	–	–	–	OKU
57026.83	76.4	17.34 ± 0.04	16.02 ± 0.02	15.70 ± 0.03	–	OKU
57030.86	80.5	17.36 ± 0.04	–	–	–	OKU
57032.80	82.4	17.49 ± 0.07	16.03 ± 0.12	15.80 ± 0.03	15.41 ± 0.02	OKU
57032.83	82.4	17.778 ± 0.054	16.334 ± 0.051	16.002 ± 0.051	15.348 ± 0.050	Kanata
57035.79	85.4	17.25 ± 0.07	16.14 ± 0.03	15.86 ± 0.03	15.47 ± 0.02	OKU
57038.76	88.4	17.41 ± 0.04	–	–	–	OKU
57039.82	89.4	17.32 ± 0.04	16.32 ± 0.06	15.93 ± 0.04	15.58 ± 0.02	OKU
57042.76	92.4	17.42 ± 0.05	16.25 ± 0.03	15.96 ± 0.11	15.34 ± 0.06	OKU
57045.82	96.3	17.34 ± 0.06	16.31 ± 0.02	16.06 ± 0.06	–	OKU
57046.67	96.3	17.506 ± 0.050	16.665 ± 0.052	–	15.484 ± 0.051	Kanata
57046.69	96.3	17.51 ± 0.05	16.34 ± 0.02	16.08 ± 0.04	–	OKU
57050.71	100.3	17.31 ± 0.16	16.35 ± 0.04	15.99 ± 0.09	–	OKU
57053.77	103.4	17.61 ± 0.03	16.44 ± 0.02	16.20 ± 0.05	–	OKU
57054.75	104.3	17.57 ± 0.04	–	–	–	OKU
57054.76	104.4	17.560 ± 0.059	16.699 ± 0.056	–	–	Kanata
57059.72	109.3	–	16.61 ± 0.04	16.31 ± 0.03	–	OKU
57063.71	113.3	17.74 ± 0.04	16.61 ± 0.02	–	–	OKU
57064.75	114.3	–	–	16.22 ± 0.07	–	OKU
57065.75	115.3	17.68 ± 0.03	16.51 ± 0.12	16.40 ± 0.13	–	OKU
57066.69	116.3	17.744 ± 0.050	16.793 ± 0.051	–	–	Kanata
57066.81	116.4	17.77 ± 0.09	16.61 ± 0.03	16.29 ± 0.07	–	OKU
57067.74	117.3	17.75 ± 0.03	16.65 ± 0.02	16.39 ± 0.04	–	OKU
57072.67	122.3	17.65 ± 0.13	16.64 ± 0.06	16.40 ± 0.03	–	OKU
57073.72	123.3	17.77 ± 0.05	16.68 ± 0.03	16.38 ± 0.05	–	OKU
57076.70	126.3	17.90 ± 0.03	16.73 ± 0.03	16.50 ± 0.05	–	OKU
57077.67	127.3	17.54 ± 0.05	16.50 ± 0.03	16.19 ± 0.05	–	OKU
57079.83	129.4	18.120 ± 0.050	17.101 ± 0.054	16.615 ± 0.053	15.889 ± 0.053	Kanata
57082.68	132.3	17.864 ± 0.050	17.169 ± 0.059	16.637 ± 0.058	15.845 ± 0.052	Kanata
57082.74	132.3	17.56 ± 0.27	16.86 ± 0.15	16.48 ± 0.08	–	OKU
57083.72	133.3	–	16.83 ± 0.02	16.47 ± 0.05	–	OKU
57085.78	135.4	–	16.82 ± 0.08	–	–	OKU
57091.65	141.2	17.76 ± 0.23	16.87 ± 0.04	16.61 ± 0.06	–	OKU
57092.69	142.3	18.03 ± 0.03	16.98 ± 0.03	–	–	OKU
57093.60	143.2	–	16.97 ± 0.02	16.69 ± 0.04	–	OKU
57095.66	145.3	–	16.90 ± 0.19	–	–	OKU
57097.59	147.2	–	16.98 ± 0.02	16.68 ± 0.05	16.17 ± 0.03	OKU
57098.59	148.2	–	17.05 ± 0.05	16.67 ± 0.06	16.30 ± 0.27	OKU
57101.62	151.2	–	16.97 ± 0.04	16.71 ± 0.03	16.19 ± 0.04	OKU
57102.53	152.1	–	17.238 ± 0.056	16.757 ± 0.052	15.955 ± 0.052	Kanata
57102.62	152.2	–	17.03 ± 0.07	16.75 ± 0.07	16.19 ± 0.11	OKU
57103.69	153.3	–	17.05 ± 0.08	16.68 ± 0.05	16.19 ± 0.06	OKU
57104.59	154.2	–	17.00 ± 0.08	16.63 ± 0.05	16.14 ± 0.02	OKU
57105.58	155.2	–	17.07 ± 0.11	16.75 ± 0.05	16.21 ± 0.04	OKU

Table 9: Log of optical photometry of SN 2014dt

MJD	Phase[11]	B (mag)	V (mag)	R (mag)	I (mag)	Site[12]
57106.56	156.2	–	17.13 ± 0.05	16.75 ± 0.06	16.25 ± 0.03	OKU
57107.53	157.1	–	17.12 ± 0.08	16.82 ± 0.04	16.33 ± 0.04	OKU
57108.55	158.1	–	17.01 ± 0.13	16.73 ± 0.07	16.11 ± 0.14	OKU
57109.57	159.2	18.28 ± 0.05	17.11 ± 0.08	16.81 ± 0.05	16.34 ± 0.05	OKU
57109.60	159.2	–	–	16.529 ± 0.056	–	Kanata
57110.61	160.2	18.297 ± 0.085	17.215 ± 0.062	16.787 ± 0.061	15.993 ± 0.056	Kanata
57111.59	161.2	18.25 ± 0.12	17.07 ± 0.05	16.79 ± 0.03	16.30 ± 0.03	OKU
57123.53	173.1	–	17.19 ± 0.09	16.87 ± 0.20	16.31 ± 0.11	OKU
57133.53	183.1	18.780 ± 0.050	17.509 ± 0.078	17.127 ± 0.057	16.250 ± 0.052	Kanata
57147.46	197.1	19.000 ± 0.050	17.629 ± 0.059	–	–	Kanata
57171.51	221.1	19.571 ± 0.087	18.013 ± 0.052	17.269 ± 0.051	16.557 ± 0.050	Kanata
57179.51	229.1	19.430 ± 0.050	17.887 ± 0.054	17.389 ± 0.054	16.444 ± 0.051	Kanata
57194.26	243.9	–	17.959 ± 0.014	17.375 ± 0.014	–	Subaru
57201.47	251.1	–	–	17.132 ± 0.059	–	Kanata
57202.47	252.1	–	–	17.535 ± 0.063	–	Kanata
57235.48	285.1	–	–	17.540 ± 0.066	16.726 ± 0.058	Kanata
57237.47	287.1	–	–	17.623 ± 0.053	16.751 ± 0.054	Kanata
57239.47	289.1	–	18.709 ± 0.091	17.596 ± 0.061	–	Kanata
57362.59	412.2	–	19.355 ± 0.017	18.621 ± 0.011	–	Subaru

[11] The phase has inevitably large uncertainty, ±4 days. See §3.1.4.
[12] See §2.

Table 10: Log of NIR photometry SN 2014dt

MJD	Phase[13]	J (mag)	H (mag)	K_s (mag)
56983.87	33.5	–	13.987 ± 0.300	14.415 ± 0.301
56990.84	40.4	14.986 ± 0.301	14.090 ± 0.301	13.987 ± 0.301
56998.87	48.5	15.224 ± 0.301	14.568 ± 0.301	14.870 ± 0.305
57046.65	96.2	15.999 ± 0.306	–	–
57050.80	100.4	15.925 ± 0.318	–	–
57054.70	104.3	16.249 ± 0.305	15.635 ± 0.309	–
57061.72	111.3	15.939 ± 0.300	–	–
57066.66	116.3	16.294 ± 0.303	15.674 ± 0.302	–
57083.63	132.2	16.309 ± 0.303	15.816 ± 0.303	> 15.9
57091.64	141.2	16.855 ± 0.336	15.939 ± 0.310	> 14.7
57103.58	153.2	16.271 ± 0.303	16.088 ± 0.310	> 15.6
57106.69	156.3	16.734 ± 0.308	–	–
57129.64	179.2	–	–	> 15.6
57137.55	187.1	16.676 ± 0.309	16.427 ± 0.311	–
57144.45	194.0	16.359 ± 0.300	–	–
57147.49	197.1	16.614 ± 0.315	16.183 ± 0.321	–
57162.61	212.2	16.727 ± 0.307	16.090 ± 0.316	–
57176.47	226.1	16.993 ± 0.340	16.846 ± 0.326	–
57355.82	405.4	16.991 ± 0.316	–	–
57375.84	425.4	17.481 ± 0.348	17.025 ± 0.323	> 17.5

[13] The uncertainty of the phase is ±4 days. See §3.1.4.

Table 11: Log of spectroscopic observations of SN 2014dt

MJD	Phase[14]	Telescope (Instrument)	Wavelength Range (Å)	Resolution[9]
56971.84	21.4	Kanata (HOWPol)	4000–9000	400
56979.86	29.5	Kanata (HOWPol)	4000–9000	400
56990.88	40.5	Kanata (HOWPol)	4000–9000	400
57014.86	64.5	Kanata (HOWPol)	4000–9000	400
57032.84	82.4	Kanata (HOWPol)	4000–9000	400
57046.69	96.3	Kanata (HOWPol)	4000–9000	400
57054.77	104.4	Kanata (HOWPol)	4000–9000	400
57066.70	116.3	Kanata (HOWPol)	4000–9000	400
57075.55	125.1	Subaru (FOCAS)	3800–10000	650
57083.67	133.3	Kanata (HOWPol)	4000–9000	400
57102.55	152.1	Kanata (HOWPol)	4000–9000	400
57127.53	177.1	Kanata (HOWPol)	4000–9000	400
57138.53	188.1	Kanata (HOWPol)	4000–9000	400
57171.52	221.1	Kanata (HOWPol)	4000–9000	400
57194.26	243.6	Subaru (FOCAS)	3800–10000	650
57362.59	412.2	Subaru (FOCAS)	3800–10000	650

[14] The uncertainty of the phase is ±4 days. See §3.1.4.

Appendix B

Estimation of the Pre-maximum to Maximum LC

Here we describe how to constrain the maximum brightness and the maximum date of SN 2014dt. We compared its early multi-band LCs with those of well-observed SNe Iax 2002cx, 2005hk, and 2012Z for which the spectra are similar to those of SN 2014dt.

We adopted the multi-band LCs of SNe 2002cx, 2005hk, and 2012Z as templates because those LCs cover both their own maximum phases and the phase when the data of SN 2014dt exist. Moreover, there are spectral resemblances and apparent similarities in the decaying part of the multi-band LCs (see §3.1.1–3.1.4). Our initial guess of the B-band maximum date of SN 2014dt was MJD 56950.8 (20.8 October 2014) in terms of the similarity in the spectral phase (§3.1.4). For a LC of each SN in a given bandpass, we allowed a shift in the time axis Δt and in the magnitude axis ΔM. Here, $\Delta t = 0$ corresponds to the initial guess, and we allowed the range of $\Delta t = \pm 10$ days with an interval of 2 days. In this procedure, the relatively densely-sampled LC data of SN 2014dt were interpolated to provide the magnitude at the (assumed) same epochs with the data points available for the reference/template SNe Iax. For each set of Δt and ΔM, we computed a residual between the SN 2014dt and the hypothesized template LC between $\sim$ 20 (the discovery date) and 60 days after the discovery of SN 2014dt. This residual, $\bar{M}$ is defined as follows;

$$\bar{M} = \sqrt{\Sigma \frac{(m_{Iax} - m_{14dt})^2}{N}}, \tag{B.1}$$

where m_{Iax} is the $BVRI$-band magnitude of the reference SN Iax, m_{14dt} is that of SN 2014dt, and N is the number of data points of SN 2014dt that overlap with the template LCs. We first obtained the 'canonical magnitude offset' in the magnitude axis, where $\bar{M}$ takes the minimum value (ΔM_0) for given Δt. To further evaluate the uncertainty in the magnitude axis in the fit, we varied the magnitude axis by Δm against ΔM_0 within the range of ± 0.3 mag with an interval of 0.1 mag, and then adopted $\Delta M = \Delta M_0 + \Delta m$. These procedures provided the distribution of $\bar{M}$ as an indicator of the similarity of the LCs among SN 2014dt and the reference SNe in each band separately ($BVRI$-band), as a function of Δt and ΔM. The set of Δt and ΔM that provided the minimum $\bar{M} \equiv \bar{M}_0$ was adopted as our tentative best-fit model for each band. To evaluate their uncertainties and avoid possible local minima, we searched the area in the Δt–ΔM plane ($|\Delta t| \leq 10$ days and $|\Delta M| \leq 0.3$ mag) where $\bar{M} < 2 \times \bar{M}_0$ holds. The ensemble of the set of Δt and ΔM satisfying above condition was adopted as acceptable ones and we estimated the uncertainties from their ranges. The choice of this criterion is somewhat arbitrary, but provides a reasonable estimate as judging by visual inspection of the fitting results.

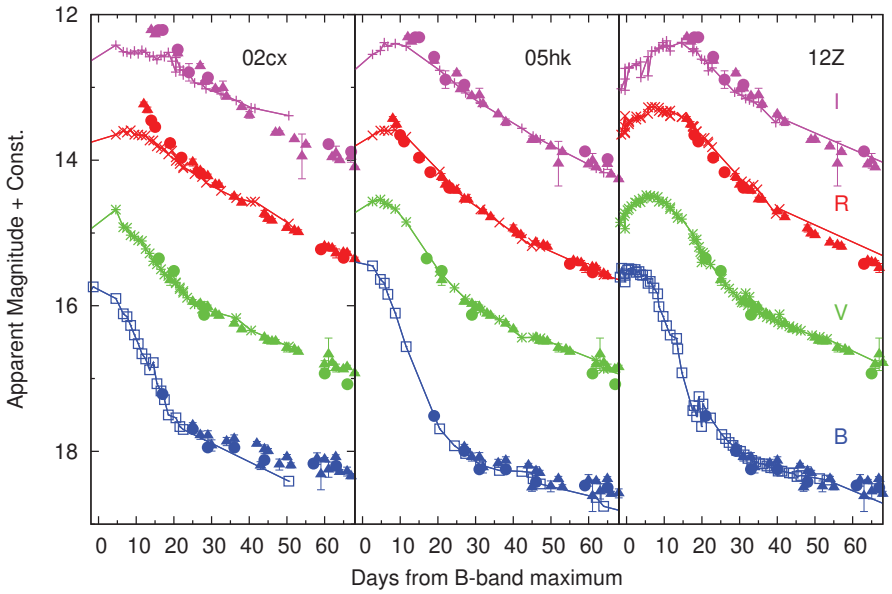

Figure 32: The best-fit LCs of SN 2014dt in the $BVRI$-band. These were derived in order to construct 'combined' LCs in the period before the discovery (i.e., around the maximum light of SN 2014dt). We adopt the LCs of SNe 2002cx (left panel), 2005hk (middle) and 2012Z (right) as templates (see text for details). For SN 2014dt, the symbols are plotted in the same manner as in Figure 8. We show the fitted reference LCs by crosses connected by solid lines.

Performing the same procedure independently for $BVRI$-band LCs, we determined the allowed range of Δt and ΔM so that the fits in all bands were mutually consistent. Indeed, we found that the multi-band LCs of SN 2002cx did not provide a consistent solution in each band (see below), and thus we concluded that the LCs of SN 2002cx should be omitted as templates. As a result, we have a series of 'combined' LCs for SN 2014dt, in which the pre-discovery part was replaced by the LC of SNe 2005hk or 2012Z, taking into account the uncertainty in Δt and ΔM.

The derived range of acceptance for Δt is $\Delta t = -2 \sim +4$ and $-4 \sim 0$, for SNe 2005hk and 2012Z, respectively, as templates. From these acceptance ranges, we assumed an uncertainty of ± 4 days in the maximum epoch throughout this thesis. Thus, we adopted the epoch of the B-band maximum and its error as MJD 56950.8 ± 4.0. Then, we have a series of 'combined' LCs in which the LCs of SN 2014dt in the pre-discovery epoch were reconstructed using the LCs of a reference SN (either SNe 2005hk or 2012Z), taking into account the conservative uncertainty in Δt and ΔM. Throughout this thesis, in cases where the pre-maximum LC data are used for the relevant analyses (e.g., the maximum magnitudes, explosion parameters), our estimation includes the error associated with this uncertainty (also including the difference in results between the two reference SNe).

To demonstrate the fitting result, and especially how it was dependent on the template SNe, we showed the best-fit LCs for each template SN (including SN 2002cx) in Figure 32. In the B- and V-bands, all of the reference SNe provided an acceptable fit for SN 2014dt. However, in the R- and I-bands, the LCs of SN 2002cx showed significantly slower decline than those of SN 2014dt and never provided a good fit, as was clear even by visual inspection.

Appendix C

Review of Another SN Iax 2005hk in Comparison with SN 2014dt

It is interesting seen in discuss the diversities in the observed properties of SNe Iax 2005hk, 2012Z and 2014dt from a viewpoint of the prediction of the weak deflagration model. As shown in §3, the diversities in photometric and spectroscopic data are likely more significant in the late phase than in the early phase. In this subsection, we apply the modeling procedure adopted in the previous sections to another SN Iax 2005hk, to investigate whether SN 2005hk can be explained within the same context of the weak deflagration model.

For SN 2005hk, Sahu et al. (2008) suggested the weak deflagration model without a bound remnant, which could reproduce the LC. The LC model 'E03' in Figure 11 is the LC presented by Sahu et al. (2008), where the explosion parameters are $E_{\rm k,05hk} = 3.0 \times 10^{50}$ erg and $M_{\rm ej,05hk} = 1.4$ M$_\odot$. In the sequence of the weak deflagration models by Fink et al. (2014), it is expected that such a small $E_{\rm k}$ model would leave a bound remnant. The critical value is $\sim$(6.0–7.0) $\times 10^{50}$ erg (Fink et al. 2014). However, considering the uncertainty in the model, it is difficult to conclude that kinetic energy as small as 3.0×10^{50} erg should be associated with a bound remnant.

Alternatively, a two-component model can also explain the LC of SN 2005hk, which mimics the presence of a bound remnant (Figure 33). The parameters of the two-component model are $M_{\rm in}(^{56}{\rm Ni}) \sim 0.04$ M$_\odot$, $[(M_{\rm ej}/M_\odot)^2/E_{51}]_{\rm in} \sim 30$, $M_{\rm out}(^{56}{\rm Ni}) \sim 0.14$ M$_\odot$ and $[(M_{\rm ej}/M_\odot)^2/E_{51}]_{\rm out} \sim 1.0$–$2.0$. SN 2005hk has a smaller fraction of the ^{56}Ni mass in the inner component than SN 2014dt. In the same way, we estimated the explosion parameters for SN 2005hk as $E_{\rm k,05hk}$ =(0.42–0.88) $\times 10^{50}$ erg and $M_{\rm ej,05hk} = 0.21$–0.42 M$_\odot$ within the context of the two-component model. The derived $[(M_{\rm ej}/M_\odot)^2/E_{51}]_{\rm in}$ indicates that the average density in the inner component of SN 2014dt may be larger than that of SN 2005hk, consistent with indications from the late phase spectra (§3.1.3). The $E_{\rm k,05hk}$ and $M_{\rm ej,05hk}$ are consistent with the weak deflagration model with a bound remnant, whose mass is smaller than in SN 2014dt (Fink et al. 2014).

In summary, we conclude that SN 2005hk can be explained by the weak deflagration model as well. It is unclear whether SN 2005hk left a bound remnant. If a bound remnant was left, the mass of the remnant would be smaller than in SN 2014dt.

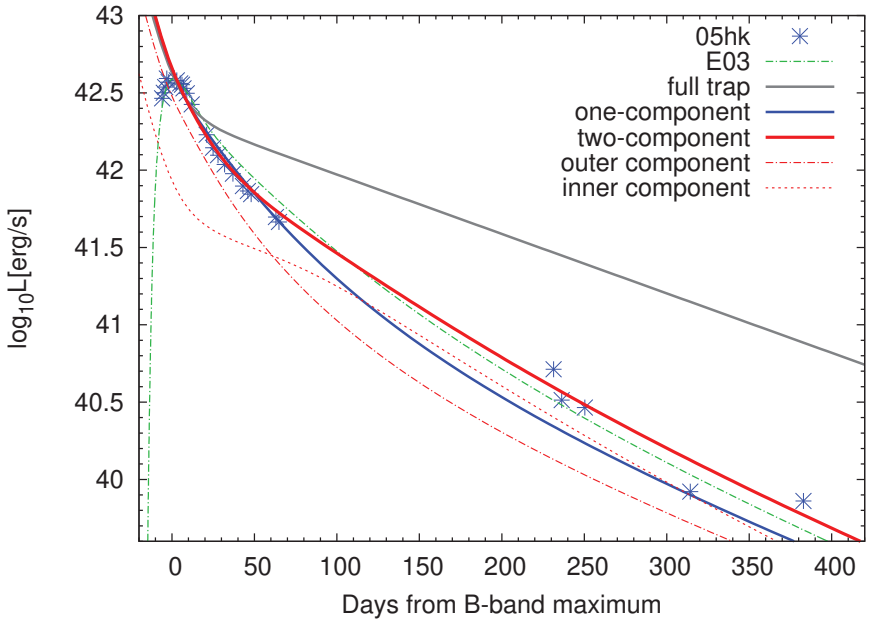

Figure 33: The bolometric light curve of SN 2005hk and corresponding LC models. The lines are plotted in the same manner as in Figure 20. The total ^{56}Ni mass is 0.18 $M_{\odot}$. We also plotted the LC of the E03 model (weak deflagration model without a bound remnant; Sahu et al. 2008) by a green dashed line (see §3.2.5), which also well represents the entire LC from the early through the late phases.

Appendix D

Bolometric LC of Other SNe Iax

As mentioned in §3.2.6, the bolometric luminosity of other SNe Iax were calculated by interpolating the SED and integrating it. First, we estimate the bolometric luminosity of SN 2005hk using the photometric data in some bands. The estimated luminosity was smaller than the actual bolometric luminosity because we only use the data in a limited number of the bands. In Figure 34, we compare the bolometric LCs of SN 2005hk that estimated from the data with the combination of the data of SN 2005hk in some bands and the bolometric LC of SN 2011fe at similar epoch. We examine these difference from the luminosity around maximum light, and take into the difference when we estimate the luminosity of other SNe Iax. We show the bolometric LCs of other SNe Iax in Figures 35, 36 and 37. In the case of SN 2014dt, we also compare the bolometric luminosity assuming that the sum of fluxes in the $BVRI$-bands occupied about 60 % of the bolometric one (see §3.2.3), and there is no significant difference between this bolometric luminosity and that by interpolating and integrating the SED (Figure 37). The bolometric luminosity after ∼30 days of SNe Iax exhibits a larg difference from that estimated using other bands and that of SN 2011fe. Then, the width of the bolometric LC for SN 2011fe is stretched to fit that for other SNe Iax until ∼30 days.

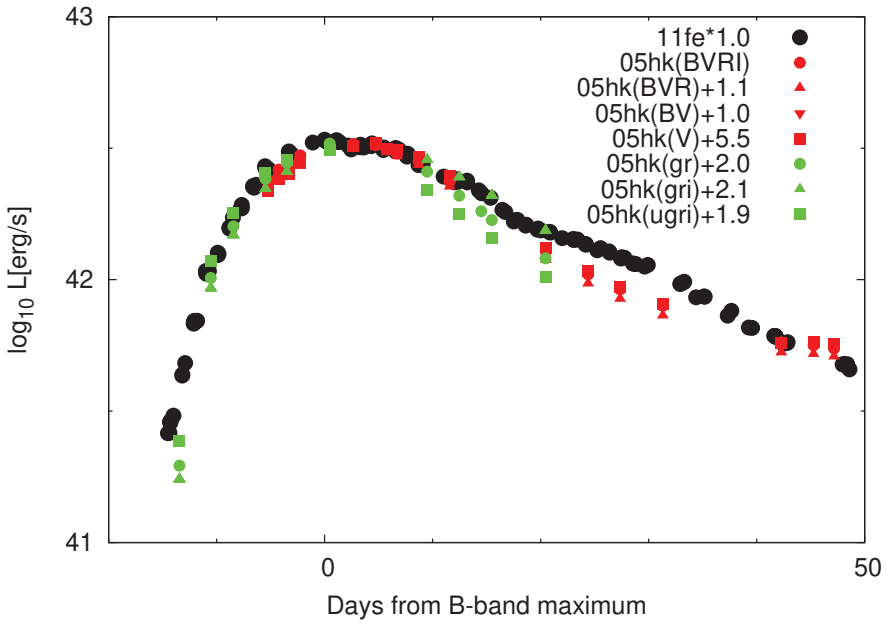

Figure 34: The bolometric light curves of SN 2005hk. The difference between the symbol and color denote the luminosity estimated using the different bands. The bolometric light curves of SN 2005hk are shifted vertically as indicated in the top-right portion of the panel to match with the bolometric one of SN 2011fe around maximum light. We show the bolometric light curve of SN 2011fe as the black circles, and it is multiplied the constant.

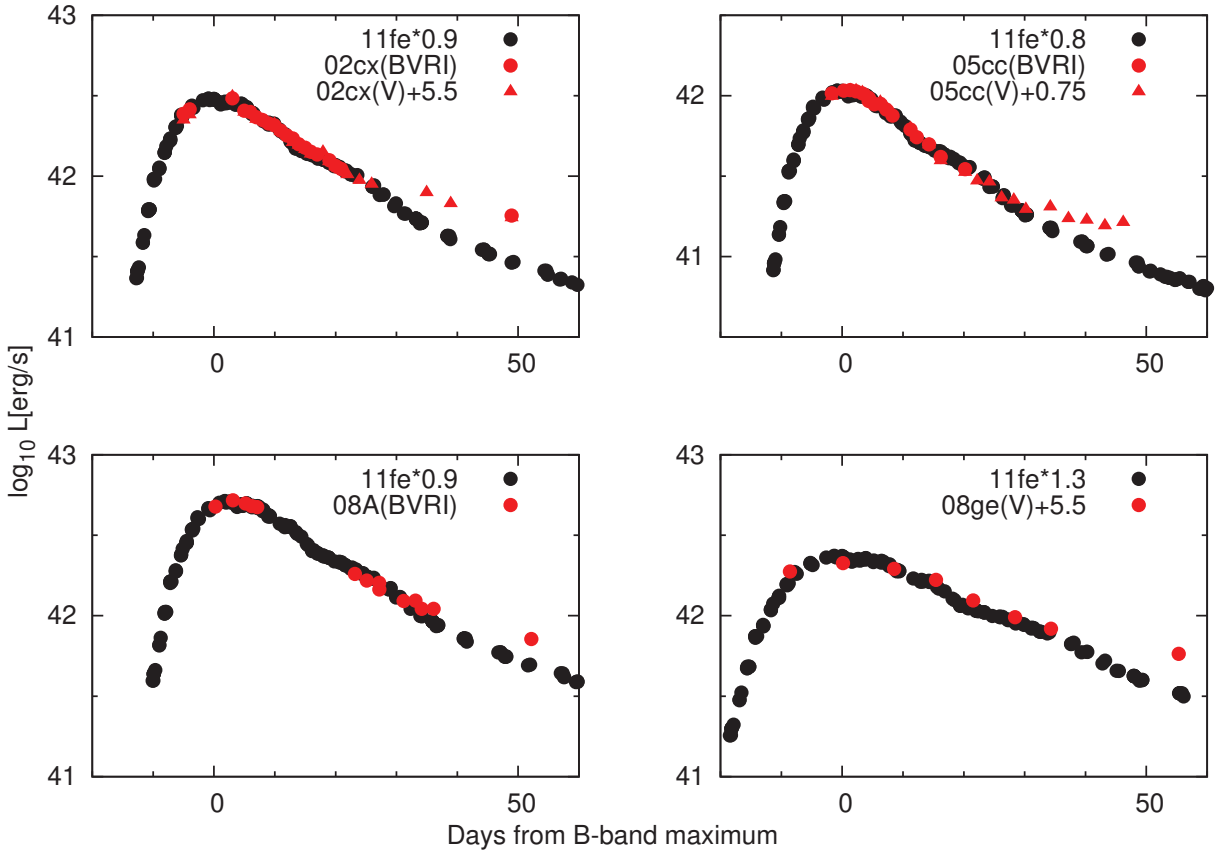

Figure 35: The bolometric light curves of SNe 2002cx (left top), 2005cc (right top), 2008A (left bottom), 2008ge (right bottom). We plot in the same manner as in Figure 34.

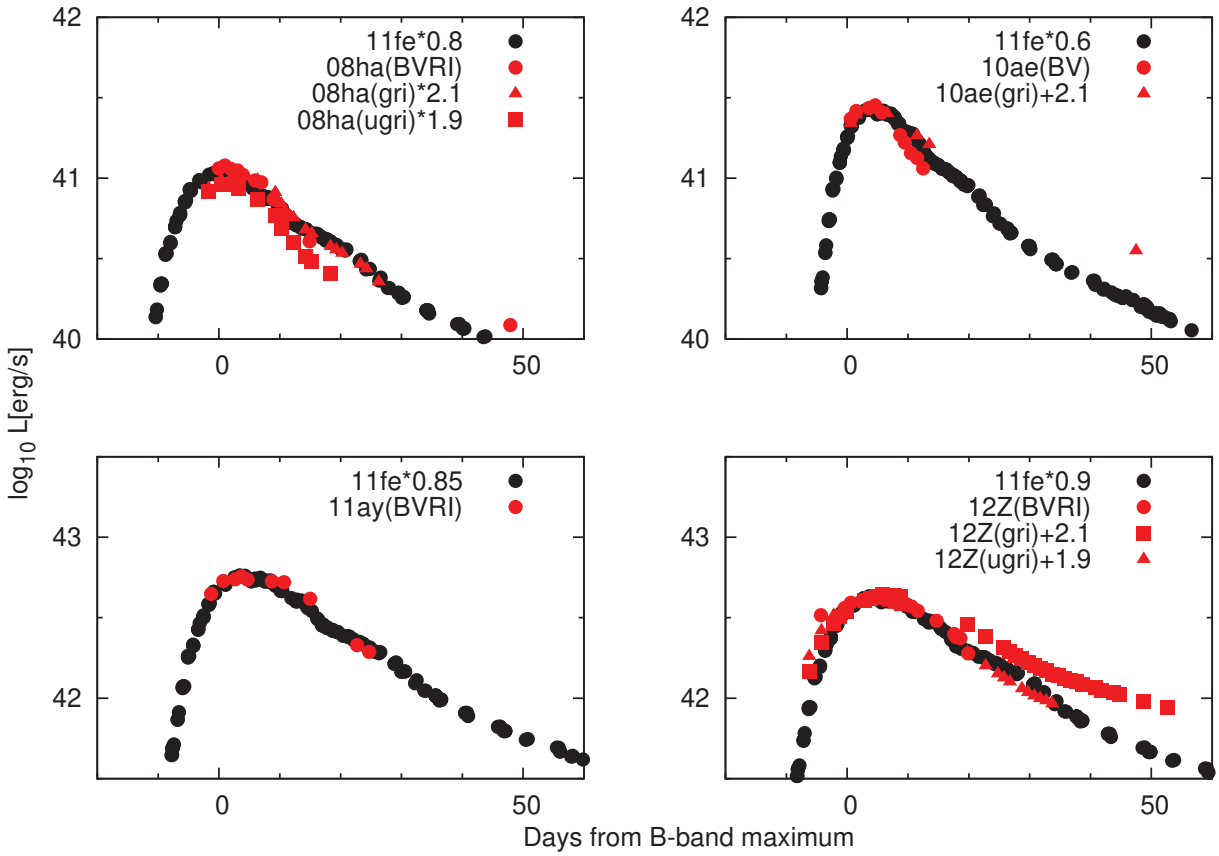

Figure 36: The bolometric light curves of SNe 2008he (left top), 2010ae (right top), 2011ay (left bottom), 2012Z (right bottom). We plot in the same manner as in Figure 34.

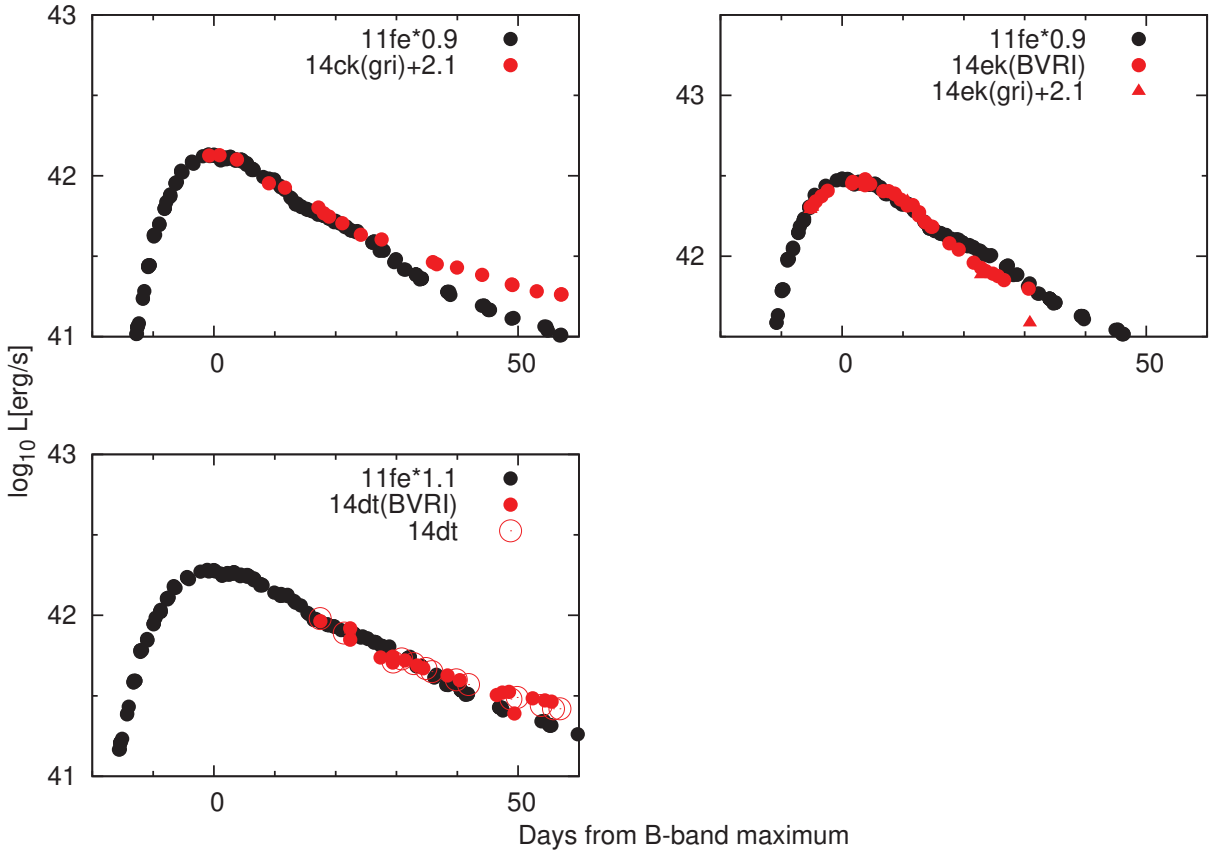

Figure 37: The bolometric light curves of SNe 2014ck (left top), 2014ek (right top), 2014dt (left bottom). We plot in the same manner as in Figure 34. The open circles of SN 2014dt is the bolometric light curve assuming that the sum of fluxes in the $BVRI$-bands occupied about 60 % of the bolometric one.

Appendix E

Observation Log of SN 2017erp

Table 12: Log of optical photometry of SN 2017erp

MJD	Phase[15]	B (mag)	V (mag)	R (mag)	I (mag)	Site[16]
57918.60	−16.8	17.438 ± 0.014	16.549 ± 0.010	16.200 ± 0.008	16.185 ± 0.012	Kanata
57919.59	−15.8	17.076 ± 0.010	16.139 ± 0.008	15.810 ± 0.008	15.830 ± 0.009	Kanata
57920.62	−14.8	16.724 ± 0.015	15.776 ± 0.010	15.402 ± 0.010	15.421 ± 0.010	Kanata
57921.56	−13.9	16.150 ± 0.012	15.398 ± 0.010	15.017 ± 0.009	15.100 ± 0.009	Kanata
57922.64	−12.8	15.872 ± 0.011	15.046 ± 0.007	14.749 ± 0.008	14.774 ± 0.006	Kanata
57923.65	−11.8	15.472 ± 0.013	14.821 ± 0.007	14.531 ± 0.007	14.548 ± 0.007	Kanata
57947.58	12.2	14.974 ± 0.008	13.964 ± 0.006	14.000 ± 0.008	14.062 ± 0.009	Kanata
57948.55	13.1	15.117 ± 0.013	14.032 ± 0.011	14.052 ± 0.012	14.137 ± 0.012	Kanata
57954.55	19.1	15.707 ± 0.007	14.438 ± 0.005	14.166 ± 0.010	14.013 ± 0.013	Kanata
57955.48	20.1	15.913 ± 0.018	14.543 ± 0.026	–	–	Kanata
57964.48	29.1	16.741 ± 0.051	14.897 ± 0.020	14.383 ± 0.018	13.936 ± 0.016	Kanata
57967.52	32.1	16.877 ± 0.018	15.048 ± 0.008	14.602 ± 0.013	14.087 ± 0.009	Kanata
57968.50	33.1	16.954 ± 0.011	15.085 ± 0.006	14.645 ± 0.007	14.115 ± 0.006	Kanata
57972.50	37.1	17.151 ± 0.032	15.308 ± 0.008	14.942 ± 0.022	14.426 ± 0.010	Kanata
57977.51	42.1	17.236 ± 0.024	15.548 ± 0.007	15.248 ± 0.008	14.726 ± 0.008	Kanata
57978.49	43.1	17.229 ± 0.017	15.652 ± 0.017	15.166 ± 0.055	14.771 ± 0.043	Kanata
57987.48	52.1	17.297 ± 0.042	–	–	15.448 ± 0.010	Kanata
57989.48	54.1	17.417 ± 0.126	15.879 ± 0.012	15.601 ± 0.009	15.219 ± 0.007	Kanata
57990.48	55.1	17.472 ± 0.024	15.873 ± 0.013	–	–	Kanata
57995.45	60.0	17.528 ± 0.025	16.031 ± 0.010	15.824 ± 0.009	15.578 ± 0.007	Kanata
58006.44	71.0	–	–	16.189 ± 0.009	15.769 ± 0.019	Kanata

[15] See §4.1.1.
[16] See §2.

Table 13: Log of Swift UVOT ultraviolet/optical photometry of SN 2017erp

MJD	Phase[17]	$UVW2$ (mag)	$UVW1$ (mag)	U (mag)	B (mag)	V (mag)
57918.21	−17.2	20.033 ± 0.148	18.792 ± 0.093	17.368 ± 0.040	17.081 ± 0.028	16.544 ± 0.040
57919.33	−16.1	19.170 ± 0.183	18.363 ± 0.151	17.131 ± 0.052	16.671 ± 0.032	16.003 ± 0.032
57920.78	−14.6	18.664 ± 0.117	17.521 ± 0.073	–	–	–
57922.78	−12.6	18.471 ± 0.072	16.925 ± 0.055	–	–	–
57922.38	−13.0	18.543 ± 0.053	–	–	–	–
57924.58	−10.8	17.901 ± 0.060	16.541 ± 0.047	15.075 ± 0.022	14.651 ± 0.024	14.500 ± 0.026
57926.76	−8.6	17.443 ± 0.050	15.600 ± 0.055	14.489 ± 0.026	14.259 ± 0.033	14.109 ± 0.019

Table 13: Log of Swift UVOT ultraviolet/optical photometry of SN 2017erp

MJD	Phase[17]	$UVW2$ (mag)	$UVW1$ (mag)	U (mag)	B (mag)	V (mag)
57928.83	−6.6	16.855 ± 0.050	15.429 ± 0.036	14.097 ± 0.036	13.985 ± 0.040	13.934 ± 0.025
57930.29	−5.1	16.610 ± 0.039	15.154 ± 0.037	13.928 ± 0.030	13.968 ± 0.042	13.806 ± 0.030
57933.41	−2.0	16.513 ± 0.043	15.403 ± 0.036	13.794 ± 0.032	13.849 ± 0.040	13.737 ± 0.033
57936.13	0.7	16.670 ± 0.051	–	14.072 ± 0.026	13.694 ± 0.024	13.611 ± 0.034
57941.24	5.8	16.957 ± 0.041	15.598 ± 0.064	14.415 ± 0.027	13.981 ± 0.032	13.728 ± 0.025
57943.65	8.2	17.358 ± 0.060	15.957 ± 0.042	14.685 ± 0.036	14.208 ± 0.032	13.813 ± 0.019
57950.41	15.0	18.261 ± 0.043	16.844 ± 0.045	15.687 ± 0.023	15.003 ± 0.018	14.291 ± 0.024
57953.07	17.7	18.316 ± 0.069	17.377 ± 0.076	15.909 ± 0.027	15.292 ± 0.024	14.385 ± 0.020
57955.06	19.7	18.830 ± 0.088	17.207 ± 0.062	16.243 ± 0.035	15.479 ± 0.019	14.568 ± 0.019
57957.54	22.1	18.965 ± 0.059	17.462 ± 0.066	16.353 ± 0.026	15.750 ± 0.022	14.600 ± 0.029
57969.82	34.4	19.656 ± 0.094	17.984 ± 0.141	17.164 ± 0.032	16.557 ± 0.015	15.275 ± 0.021
57976.65	41.2	19.770 ± 0.105	18.491 ± 0.081	17.465 ± 0.038	16.937 ± 0.023	15.666 ± 0.021

[17] See §4.1.1.

Table 14: Log of spectroscopic observations of SN 2017erp

MJD	Phase[18]	Telescope (Instrument)	Wavelength Range (Å)	Resolution
57918.62	−16.8	Kanata (HOWPol)	4000–9000	400
57920.64	−14.8	Kanata (HOWPol)	4000–9000	400
57922.61	−12.8	Kanata (HOWPol)	4000–9000	400
57923.62	−11.8	Kanata (HOWPol)	4000–9000	400
57947.59	12.2	Kanata (HOWPol)	4000–9000	400
57977.49	42.1	Kanata (HOWPol)	4000–9000	400

[18] See §4.1.1.

Appendix F

On the Systematics in Photometry for SN 2017erp

SNe may be affected by the contamination from the host galaxy. In the case of SN 2017erp, we attempt to use some photometry methods, and change the parameters; aperture photometry that the aperture is 3 and 5 arcsec respectively, PSF photometry; aperture photometry that 3 arcsec aperture after we subtract the host galaxy. Additionally, we compare with the result of Brown et al. (2018). We show the comparison in Figures 38 and 39. In the V-band, our results are slightly fainter, but there is little or no difference due to the photometry methods or the photometric parameters. Thus, the contamination is small in the V-band. In the $UVW1$-band, although some differences are seen, the contamination has not affected. Although the result using PSF photometry is consistent with that of Brown et al. (2018), the difference is seen in the $UVW1$-band like the V-band. Then, we adopt the PSF photometry for SN 2017erp to avoid the influence of the contamination as much as possible.

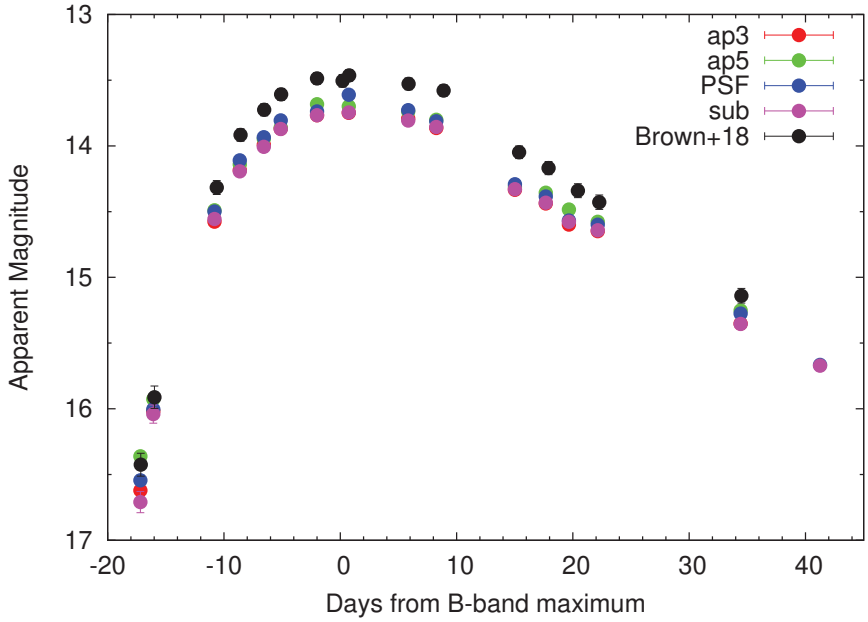

Figure 38: The V-band light curves of SN 2017erp. The red, green, blue and pink symbols denote aperture photometry that the aperture is 3 arcsec, aperture photometry that the aperture is 5 arcsec, PSF photometry and aperture photometry that 3 arcsec aperture after we subtract the host galaxy, respectively. For comparison, we plotted the light curve from Brown et al. (2018) as black symbols.

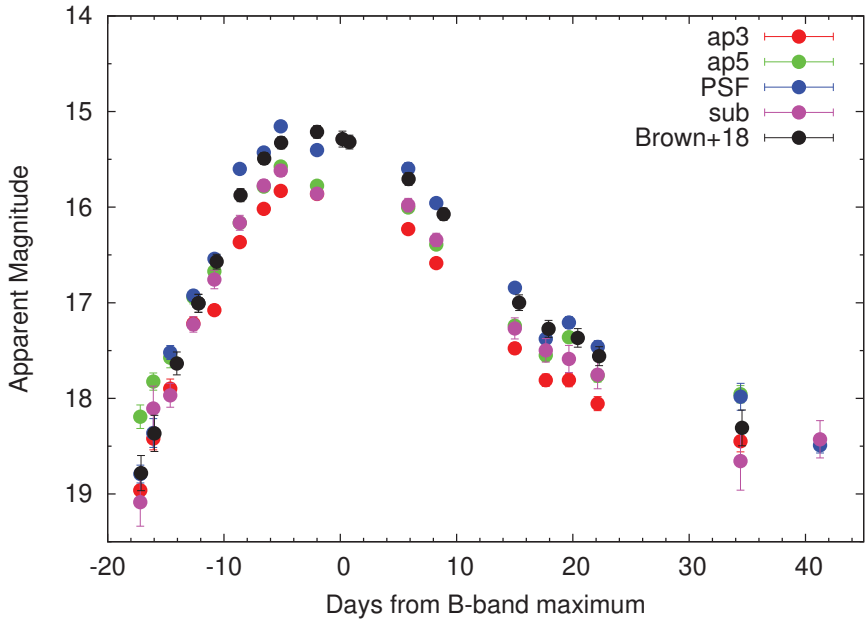

Figure 39: The $UVW1$-band light curves of SN 2017erp. We plot in the same manner as in Figure 38.